FEDERAL UNIVERSITY OF SANTA CATARINA
SCHOOL OF TECHNOLOGY
GRADUATE PROGRAM IN CHEMICAL ENGINEERING

CONTRIBUTIONS TO THE PHOTOCATALYTIC NOx DEGRADATION PROCESS USING COMPUTATIONAL FLUID DYNAMICS

Jéssica Oliveira de Brito Lira

Florianópolis
2019

Jéssica Oliveira de Brito Lira

CONTRIBUTION TO THE PHOTOCATALYTIC NOx DEGRADATION PROCESS USING COMPUTATIONAL FLUID DYNAMICS

Dissertation submitted to the Graduate Program in Chemical Engineering at Federal University of Santa Catarina to obtain a Master's degree in Chemical Engineering.

Advisor: Prof. Dr. Cíntia Soares
Co-advisor: Prof. Dr. Natan Padoin
Prof. Dr. Vítor J. P. Vilar

Florianópolis
2019

Ficha de identificação da obra elaborada pelo autor através do Programa de Geração Automática da Biblioteca Universitária da UFSC.

Lira, Jéssica Oliveira de Brito
CONTRIBUTION TO THE PHOTOCATALYTIC NOx DEGRADATION PROCESS USING COMPUTATIONAL FLUID DYNAMICS / orientadora, Cíntia Soares ; coorientador, Natan Padoin ; coorientador, Vitor J. P. Vilar, Florianópolis, SC, 2019.

131 p.

Dissertação (mestrado) - Universidade Federal de Santa Catarina, Centro Tecnológico. Programa de Pós-Graduação em Engenharia Química.

Inclui referências.

1. Engenharia Química. 2. Fluidodinâmica computacional (CFD). 3. Fotocatálise heterogênea. 4. Poluição atmosférica. 5. Óxido de nitrogênio. I. Soares, Cintia. II. Padoin, Natan. III. Vilar, Vitor J. P. IV. Universidade Federal de Santa Catarina. Programa de Pós-Graduação em Engenharia Química. V. Título.

Jéssica Oliveira de Brito Lira

CONTRIBUTION TO THE PHOTOCATALYTIC NOx DEGRADATION PROCESS USING COMPUTATIONAL FLUID DYNAMICS

This dissertation was considered adequate for the degree of Master in Chemical Engineering and was approved in its final form by the Graduate Program in Chemical Engineering at Federal University of Santa Catarina.

Florianópolis, February 28th 2019.

_____
Prof. Dr. Cíntia Soares
Coordinator of the Graduate Program in Chemical Engineering

Examination Board:

_____
Prof. Dr. Cíntia Soares
Advisor
Federal University of Santa Catarina

_____
Prof. Dr. João Lameu da Silva Jr.
Federal Institute of Education, Science and Technology of South of Minas Gerais

_____
Prof. Dr. Alexandre Kupka da Silva
Federal University of Santa Catarina

This work is dedicated to my family, especially to my parents, Fernando and Nadja, and my sister, Fernanda.

ACKNOWLEDGEMENTS

First of all, I have to thank God for all blessings in my life, in particular for these years of hard work during this journey to the conclusion of my Master's degree.

I am grateful to my family for their continuous support during my study. I thank my parents, Fernando and Nadja and my sister Fernanda who are proud of my achievements. Thanks for all teachings, love, unconditional support and understanding in the moments when I had to abdicate family moments.

I would like to convey my deepest gratitude to my advisors, Prof. Dr. Cíntia Soares and Prof. Dr. Natan Padoin, for their constant encouragement, invaluable guidance, patience, and understanding throughout the whole length of my Master's degree. Thank you for believing in my potential and for all the opportunities you have given me for this work to be done, highlighting your precise and efficient guidelines.

I would like to thank the members of the examination board for their willingness to evaluate and contribute to this dissertation.

Also, I would like to sincerely thank all my friends from UFSC, especially Ricardo Cunha, Fernanda Fraga, Mayara Schäfer, Daniela Gier, Vinícius Macedo and Anderson Moreno, who somehow contributed with all the support throughout my journey, sharing moments of sadness, relaxing in moments of tension and adding moments of happiness and laughter.

Many thanks to Ana Paula Fagundes, Gabriela Oliveira, Ana Paula Capelezzo, Laura Mohr, Anderson Viana and Lusitâneo Macuvele of the LABMAC group for the companionship and the assistance during my moments in the laboratory.

I would like to thank my dear friend Lígia Rabay for always being present in my life, supporting me and vibrating with my achievements. And also to friends Raquel Alves, Camila Cunha, Mayara Maia, Diego Duarte and Gabrielle Lessa for sharing with me happy moments of games and dinners.

I am also thankful for the financial support from CAPES (Coordination for the Improvement of Higher Level Personnel) and CNPq (National Council for Scientific and Technological Development).

Finally, I would like to thank all others who directly and indirectly contributed to the accomplishment of this work.

“If one day you have to choose between the world and love, remember this: If you choose the world you’ll be left without love, but if you choose love, with it you will conquer the world.”
(Albert Einstein)

ABSTRACT

In recent years, air pollution has become a worldwide concern because it is one of the most harmful types of environmental pollution to humans. Among the air pollutants, nitrogen oxides (NOx) stand out because they negatively affect the quality of the environment, and they are also one of the major causes of many health problems related to human beings. In this way, numerous researches have been developed with the objective of degrading these gaseous pollutants; in this scenario, heterogeneous photocatalysis becomes a promising technology for this purpose. The Computational Fluid Dynamics (CFD) has been highlighted when it is associated with the heterogeneous photocatalysis phenomenon since it presents advantages over traditional experimental techniques. Besides the cost- and time-economy, this tool allows a more rigorous and detailed analysis of the processes. In this context, the present work aims to develop a 2D and 3D CFD model for the investigation of photocatalytic NOx abatement, taking a flat plate photocatalytic reactor as benchmark. The proposed model was validated with experimental data provide by Ballari *et al.* (2010). The numerical experiments were carried out in the commercial software ANSYS® CFD (Fluent®), version 14.0, and considered the coupling of fluid flow, chemical species transport and Langmuir-Hinshelwood-Hougen-Watson (LHHW) kinetics model to represent the NOx photocatalytic degradation reaction within the photoreactor. The paper was divided into two parts. Initially, a 2D model was implemented and a comprehensive analysis of the effect of varying several operating parameters (relative humidity, irradiation intensity and NO inlet concentration) as well as geometric characteristics of the reactor was performed. Moreover, a comparison with the 1D ideal plug flow model was carried out. Furthermore, a 3D model was implemented and compared with the 2D approach, identifying the differences between the models. The results of the CFD simulation showed that the 2D model presented good agreement with the experimental data from the literature. It was observed that the process parameters investigated had a strong influence on NOx removal efficiency, especially low values of relative humidity (10%), high values of light intensity (13 $W \cdot m^{-2}$) and low values of initial concentration of NO (4.5×10^{-9} $kmol \cdot m^{-3}$) which provided a NO conversion of approximately 43%, 37%, and 51%, respectively. When varying the reactor's height, it was found a non-linear behavior of this parameter regarding the reaction rates. Moreover, the 2D CFD model resulted in advantages when compared to the ideal 1D plug flow

approach, since the NO and NO_2 mass fraction profiles presented non-idealities in the reactive flow inside the photocatalytic device. The 3D model was also validated and small variations (< 1%) were observed when compared to the 2D approach, evidencing that the two-dimensional model can be used as a good approximation of the photocatalytic reactor applied to NOx degradation.

Keywords: Computational Fluid Dynamics (CFD). Heterogeneous photocatalysis. Atmospheric pollution. Nitrogen oxide.

RESUMO

Nos últimos anos, a poluição atmosférica tem se tornado uma preocupação em escala mundial, pois figura como um dos tipos de poluição ambiental mais danosos aos seres humanos. Dentre os poluentes atmosféricos, os óxidos de nitrogênio (NOx) se destacam, pois, afetam negativamente a qualidade do ambiente e também são uma das maiores causas de vários problemas relacionados a saúde dos seres humanos. Dessa forma, pesquisas vêm sendo desenvolvidas com o objetivo de degradar desses poluentes gasosos, nesse cenário destaca-se a fotocatálise heterogênea como uma tecnologia promissora para esse fim. A tecnologia da fluidodinâmica computacional (CFD) vêm ganhando destaque quando associado ao fenômeno da fotocatálise heterogênea, pois apresenta vantagens sobre as técnicas experimentais tradicionais. Além da economia de custo e tempo, essa ferramenta permite uma análise mais rigorosa e detalhada dos processos. Nesse contexto, o presente trabalho tem por objetivo desenvolver um modelo 2D e 3D CFD para a investigação do abatimento fotocatalítico de NOx, tomando como referência um reator fotocatalítico de placa plana. O modelo proposto foi validado com os dados experimentais fornecidos por Ballari *et al.* (2010). Os experimentos numéricos foram realizados no software comercial ANSYS® CFD (*Fluent*®), versão 14.0, e considerou o acoplamento do fluxo de fluidos, transporte de espécies químicas e modelo cinético de Langmuir-Hinshelwood-Hougen-Watson (LHHW) para representar a reação de degradação fotocatalítica de NOx dentro do fotoreactor. O trabalho foi dividido em duas partes. Inicialmente, um modelo 2D foi implementado e uma análise abrangente do efeito da variação de vários parâmetros operacionais (umidade relativa, intensidade de irradiação e concentração de entrada de NO), bem como características geométricas do reator foi realizada. Adicionalmente, uma comparação com o modelo 1D *plug flow* ideal foi realizada. A segunda parte do presente trabalho aborda a elaboração de um modelo 3D e comparação com o modelo 2D proposto anteriormente, identificando as diferenças entre os modelos. Os resultados das simulações em CFD mostraram que o modelo 2D apresentou boa concordância com os dados experimentais reportados por Ballari *et al.* (2010). Observou-se que os efeitos de diversos parâmetros de processo apresentaram forte influência na eficiência de remoção de NOx, com destaque para à baixos valores de umidade relativa (10%), altos valores de intensidade luminosa (13 $W \cdot m^{-2}$) e baixos valores de concentração inicial de NO (4.5×10^{-9} $kmol \cdot m^{-3}$) que proporcionou uma

conversão de NO de aproximadamente 43%, 37%, e 51%, respectivamente. Ao variar a altura do reator, foi encontrado um comportamento não-linear deste parâmetro em relação às taxas de reação. Além disso, o modelo 2D CFD resultou em vantagens quando comparado à abordagem ideal 1D *plug flow*, pois os perfis da fração mássica de NO e NO_2 apresentaram não idealidades decorrentes ao fluxo reativo dentro do dispositivo fotocatalítico. O modelo 3D também foi validado, porém foram observadas pequenas variações (erros inferiores à 1%) quando comparado ao modelo 2D, evidenciando que o modelo bidimensional pode ser utilizado como boa aproximação do reator fotocatalítico para a degradação de NOx.

Palavras-chave: Fluidodinâmica computacional (CFD). Fotocatálise heterogênea. Poluição atmosférica. Óxido de nitrogênio.

RESUMO EXPANDIDO

Introdução

Nos últimos anos, a poluição atmosférica tem se tornado uma preocupação em escala mundial, pois figura como um dos tipos de poluição ambiental mais danosos aos seres humanos. Dentre os poluentes atmosféricos, os óxidos de nitrogênio (NOx) se destacam, ao afetarem negativamente a qualidade do ambiente e também por serem uma das maiores causas de problemas relacionados a saúde dos seres humanos. Dentre os impactos causados pelos gases NOx ao meio ambiente podem ser citados a chuva ácida, fumaça fotoquímica (*smog*) e a contribuição para o efeito estufa. Além dos problemas ambientais, esses gases trazem inúmeros prejuízos à saúde humana, pois podem causar edemas pulmonares, gerando desde um desconforto até morte por asfixia (BRAGA *et al.*, 2005). Dessa forma, pesquisas vêm sendo desenvolvidas com o objetivo de degradar esses poluentes gasosos. Nesse cenário destaca-se a fotocatálise heterogênea como uma tecnologia promissora para esse fim, uma vez que essa técnica favorece a degradação dos poluentes formando compostos menos nocivos ao meio ambiente. A tecnologia da fluidodinâmica computacional (CFD) vem ganhando destaque quando associada ao fenômeno da fotocatálise heterogênea, pois apresenta vantagens sobre as técnicas experimentais tradicionais, visto que, CFD complementa abordagens experimentais e analíticas demostrando um meio alternativo e econômico de simular o fluxo real (economia de custo e tempo), CFD tem a capacidade de simular condições de fluxo que não são reprodutíveis em testes experimentais e o CFD pode fornecer informações mais detalhadas e mais abrangentes quando comparada à abordagem experimental.

Objetivos

Nesse contexto, o presente trabalho tem por objetivo desenvolver um modelo 2D e 3D CFD para a investigação do abatimento fotocatalítico de NOx, tomando como referência um reator fotocatalítico de placa plana para validação. Além disso, pretende-se avaliar o comportamento do reator fotocatalítico sob diferentes condições operacionais, analisar o comportamento do reator sob variação da altura do canal e comparar o modelo 2D proposto com uma abordagem 1D *plug flow* ideal e com o modelo 3D do reator de placa plana.

Metodologia

O modelo proposto foi validado com os dados experimentais fornecidos

por Ballari *et al.* (2010) em uma placa de concreto impregnado com TiO_2. Os experimentos numéricos foram realizados no software comercial ANSYS® CFD (*Fluent*®), versão 14.0, e considerou o acoplamento do fluxo de fluidos, transporte de espécies químicas e modelo cinético de Langmuir-Hinshelwood-Hougen-Watson (LHHW) para representar a reação de degradação fotocatalítica de NOx dentro do fotoreator de placa plana. O trabalho foi dividido em duas partes. Inicialmente, um modelo 2D foi implementado e uma análise abrangente foi realizada acerca do efeito da variação de vários parâmetros operacionais (umidade relativa, intensidade de irradiação e concentração de entrada de NO), bem como das características geométricas do reator (a partir da variação da altura (*H*) do canal). Adicionalmente, uma comparação com o modelo 1D *plug flow* ideal foi produzida. Na segunda parte do presente trabalho foi abordada a elaboração de um modelo 3D, validação com os dados experimentais fornecidos por Ballari *et al.* (2010) e comparação com o modelo 2D proposto anteriormente, identificando as diferenças entre os modelos. Todas as simulações numéricas para os modelos 2D e 3D foram realizadas sob mesmas condições operacionais (isto é, o mesmo computador usado em todas as simulações: Intel® Xeon® @ 2.67 GHz; 72 GB CPU de RAM e sistema operacional Windows 64-bit).

Resultados

Os resultados foram obtidos com base na conversão de NO (X_{NO}) e seletividade (S). O modelo 2D do reator de placa plana foi avaliado em função de alguns parâmetros como umidade relativa (RH = 10 – 60%), intensidade luminosa (E = 0,3–13 $W \cdot m^{-2}$) e concentração inicial de NO (C_{NO}^{in} = $4{,}5\times10^{-9}$ – $4{,}47\times10^{-8}$ $kmol \cdot m^{-3}$). Foi observada uma tendência do reator mediante a variação desses parâmetros, à medida que a umidade relativa aumentou, houve uma redução de X_{NO} na saída do reator. Já X_{NO} e S aumentaram com o aumento da intensidade luminosa. Por outro lado, para C_{NO}^{in}, a conversão de NO e a seletividade diminuíram com o aumento dessa variável. Todas as análises obtiveram boa concordância com os dados experimentais fornecidos por Ballari *et al.* (2010). Adicionalmente, o modelo 2D proposto apresentou vantagens significativas quando comparado com a abordagem 1D *plug flow* ideal, pois foram observadas não-idealidades na superfície catalítica (y = 0) decorrentes ao fluxo reativo dentro do dispositivo fotocatalítico e um comportamento mais complexo foi associado ao fluxo de NO_2. Além disso, o modelo 2D CFD permitiu uma análise abrangente de diferentes características geométricas quando a dimensão H foi variada (H, 2H e

4*H*), mantendo constante o tempo de residência. Ficou evidente que à medida que *H* aumentou, houve maior contribuição do meio, a X_{NO} diminuiu e *S* passou por um ponto de mínimo, evidenciando a necessidade de otimização do desempenho do reator. Adicionalmente, o modelo 2D proposto foi comparado com o modelo 3D para predizer as diferenças observadas entre esses modelos. Uma excelente concordância foi observada variando *RH* (10 – 60%), resultando em desvios de menos de 1% entre os modelos. Além disso, os perfis de fração mássica de NO e NO_2 também foram comparados. Foi observado que o comportamento dos perfis dentro do reator foi bastante similar, porém desvios entre eles foram notados devido ao efeito de borda associado ao fluxo das espécies próximos às paredes laterais do reator ($z = 0$ e $z = W$). Esse efeito foi encontrado apenas nas simulações em 3D, sendo negligenciada no modelo 2D devido à ausência da terceira dimensão, porém esse efeito não teve grande relevância nos resultados quantitativos. Logo, o modelo 2D conseguiu representar o reator fotocatalítico de placa plana, obviamente permitindo cálculos mais rápidos.

Considerações finais

Os resultados das simulações em CFD mostraram que o modelo 2D apresentou boa concordância com os dados experimentais reportados por Ballari *et al.* (2010). Observou-se que os efeitos de diversos parâmetros de processo apresentaram forte influência na eficiência de remoção de NOx, com destaque para à baixos valores de umidade relativa (10%), altos valores de intensidade luminosa (13 $W \cdot m^{-2}$) e baixos valores de concentração inicial de NO ($4{,}5 \times 10^{-9}$ $kmol \cdot m^{-3}$) que proporcionara uma conversão de NO de aproximadamente 43%, 37%, e 51%, respectivamente. Ao variar a altura do reator, foi encontrado um comportamento não-linear deste parâmetro em relação às taxas de reação. Além disso, o modelo 2D CFD resultou em vantagens quando comparado à abordagem ideal 1D *plug flow*, pois os perfis da fração mássica de NO e NO_2 apresentaram não idealidades decorrentes ao fluxo reativo dentro do dispositivo fotocatalítico. O modelo 3D também foi validado, porém foram observadas pequenas variações (desvios inferiores à 1%) quando comparado ao modelo 2D, evidenciando que o modelo bidimensional pode ser utilizado como boa aproximação do reator fotocatalítico para a degradação de NOx.

Palavras-chave: Fluidodinâmica computacional (CFD). Fotocatálise heterogênea. Poluição atmosférica. Óxido de nitrogênio.

LIST OF FIGURES

LIST OF TABLES

LIST OF ABBREVIATIONS

AOP	advanced oxidation processes
CAPES	Coordination for the Improvement of Higher Level Personnel
CB	conduction band
CFD	computational fluid dynamics
CNPq	National Council for Scientific and Technological Development
CONAMA	National Council for the Environmental
e^-	electrons
E_{BG}	bandgap energy
EEA	European Environmental Agency
EPA	Environmental Protection Agency
GCI	grid convergence index
h^+	hole
hν	photon
MEP	Ministry of Environmental Potection
LABMAC	Laboratory of Materials and Corrosion
LHHW	Langmuir-Hinselwood-Hougen-Watson
NO	nitric oxide
NO_2	nitrogen dioxide
NOx	nitrogen oxides
$O_2^{\cdot-}$	superoxide anion
$OH^{\cdot}$	hydroxyl radicals
PM	particulate matter
TiO_2	titanium dioxide
UV	ultra violet
UDF	user-defined function
VB	valence band
VOC	volatile organic compounds
WHO	world health organization

LIST OF SYMBOLS

A	area (m^2)
$\|A_i\|$	area of an element (m^2)
AU	absolute humidity ($kg \cdot kg^{-1}$)
C_i	molar concentration of species *i* ($kmol \cdot m^{-3}$)
C_T	total molar concentration ($kmol \cdot m^{-3}$)
$D_{i,m}$	molecular diffusion coefficient for species *i* in the mixture ($m^2 \cdot s^{-1}$)
D_{ij}	molecular diffusion coefficient for the pair *i-j* ($m^2 \cdot s^{-1}$)
E	irradiance ($W \cdot m^{-2}$)
f_{NO}, f_{NO2}	correction factor
H	reactor height (m)
J_i	molecular diffusion flux of species *i* ($kmol \cdot m^{-2} \cdot s^{-1}$)
K_i	equilibrium parameter for species *i* ($m^3 \cdot kmol^{-1}$)
k_i''	kinetic parameter for specieis *i* ($kmol \cdot m^{-2} \cdot s^{-1}$)
L	reactor length (m)
M_w	mixture molecular weight ($kg \cdot kmol^{-1}$)
$M_{w,i}$	molecular weight of species *i* ($kg \cdot kmol^{-1}$)
P	pressure ($kg \cdot m^{-1} \cdot s^{-2}$)
P_{abs}	absolute pressure ($kg \cdot m^{-1} \cdot s^{-2}$)
R	universal gas constant ($m^2 \cdot s^{-2} \cdot K^{-1}$)
RH	relative humidity (%)
r_i''	reaction rate for species *i* per unit of area ($kmol \cdot m^{-2} \cdot s^{-1}$)
S	selectivity (%)
T	absolute temperature (K)
T^*	dimensionless temperature
$\hat{V}$	specific volume of dry air ($m^3 \cdot kg^{-1}$)
$\hat{V}^*$	specific volume of water ($m^3 \cdot kg^{-1}$)
$\vec{v}$	velocity vector ($m \cdot s^{-1}$)
v_x, v_y, v_z	velocity components ($m \cdot s^{-1}$)
W	reactor width (m)
w_i	mass fraction of species *i*
x,y,z	cartesian coordinates (m)
X_i	conversion of species *i* (%)
y_i	molar fraction of species *i*
α	kinetic parameter related to irradiance ($m^2 \cdot W^{-1}$)
$(\epsilon/k_B)_i$	Lennard-Jones energy parameter for species *i* (K)
$(\epsilon/k_B)_{ij}$	Lennard-Jones energy parameter for the pair *i-j* (K)

μ	mixture viscosity ($kg \cdot m^{-1} \cdot s^{-1}$)
μ_i	viscosity of species *i* ($kg \cdot m^{-1} \cdot s^{-1}$)
ρ	mixture density ($kg \cdot m^{-3}$)
ρ_i	density of species *i* ($kg \cdot m^{-3}$)
σ_i	Lennard-Jones characteristic length of species *i* ($\dot{A}$)
σ_{ij}	Lennard-Jones characteristic length of the pair *i-j* ($\dot{A}$)
$\vec{\tau}$	stress tensor ($kg \cdot m^{-1} \cdot s^{-2}$)
τ_{ij}	stress tensor components ($kg \cdot m^{-1} \cdot s^{-2}$)
Ω_D	collision integral

Mathematical Operators

$\nabla \cdot \vec{B}$	Divergence of a vector.

$$\nabla = \frac{\partial}{\partial x}\boldsymbol{e}_x + \frac{\partial}{\partial y}\boldsymbol{e}_y + \frac{\partial}{\partial z}\boldsymbol{e}_z$$

CONTENTS

1 INTRODUCTION

Since the Industrial Revolution and combined with the rapid growth of cities, urban environments have dealt with serious problems related to air pollution, becoming a worldwide concern. This issue receives a lot of attention because the data on air quality in the world become more available and accessible. In this sense, it becomes more evident that the magnitude of this problem negatively affects the environment, the economy, and the quality of life.

Air pollution is characterized by the presence of undesirable substances in the air that cause damage to human health and the environment. Typical air pollutants are particulate matters (PM), nitrogen oxides (NOx), carbon monoxide (CO) and volatile organic compounds (VOC). Among the air pollutants mentioned above, nitrogen oxides (NOx = NO + NO_2) deserve special attention, since they cause numerous problems to the environment such as acid rain, photochemical smog, and contribute to global warming. These gases also can directly affect human health, causing serious respiratory problems (BRAGA *et al.*, 2005).

Traditionally, the air pollutants are removed by a number of conventional methods, such as the use of air purifiers employing filters for removal of particulate matters, thermal oxidation, condensation and also the use of sorption materials to adsorb toxic gases and odors (LIM *et al.*, 2009). However, such techniques only transfer contaminants from one phase to another, rather than eliminating them, which requires subsequent waste handling steps.

The limitations observed in conventional technologies have encouraged research on more practical and effective pollutant degradation strategies. Thus, heterogeneous photocatalysis emerges as an alternative and promising technology to conventional methods due to its ability to operate under ambient conditions (i.e., at room temperature and atmospheric pressure). This process occurs by the activation of the photocatalyst under the light (solar or artificial) (ÂNGELO *et al.*, 2013; BOYJOO *et al.*, 2017). Thus, to improve air quality, photocatalytic processes have been suggested as a new remediation technology. In this case, the photocatalyst is often used in combination with building materials, and it has proved effective in removing air pollutants. Some innovative photocatalytic materials were developed from concrete pavements (HÜSKEN; HUNGER; BROUWERS, 2009), mortars (KRISHNAN *et al.*, 2013), asphalts (CAO *et al.*, 2017) and paints (ÂNGELO; ANDRADE; MENDES, 2014), with the aim of degrading NOx and, consequently, enhance the air quality.

Despite the many advantages of heterogeneous photocatalysis and the extensive laboratory research done in this field, there are still some factors that do not allow this technology to reach its full potential. The experimental methods provide an overview of the process and do not allow a local analysis of the reactor's interior, i.e., it is not possible to observe the behavior of some parameter of interest, such as the formation of the dead zones or the distribution of UV radiation along the reactor. For a more rigorous and detailed analysis, microscopic models based on transport phenomena must be employed, and an important tool is Computational Fluid Dynamics (CFD), which has emerged as a robust simulation strategy for chemical engineering.

There are several studies of CFD applied to photocatalytic reactor systems for air purification, such as flat plate reactor (SALVADÓ-ESTIVILL; BRUCATO; LI PUMA, 2007), corrugated plate (PASSALÍA *et al.*, 2011), annular (KUMAR; BANSAL, 2015), multi-annular (IMOBERDORF *et al.*, 2006), multi-tube (ROEGIERS; VAN WALSEM; DENYS, 2018), among others. The modeling and simulation of these reactors require the simultaneous solution of moment equation, chemical species transport, heterogeneous reaction kinetics and even the radiation transport equation. Additionally, the use of CFD allows a more comprehensive analysis of the fluid dynamics and the performance of the photocatalytic reactor, providing the local values of the interest parameters. However, the CFD simulations results need to be validated to increase the reliability of the proposed model. Thus, several studies were devoted to the photocatalytic systems modeling for the gaseous pollutants abatement.

In this sense, this study aims to implement a 2D/3D CFD model for a flat plate reactor applied to photocatalytic NOx abatement. The proposed model was compared and validated with experimental data provided by Ballari *et al.* (2010). A model-based comprehensive phenomenological evaluation of the reactor's performance under different operational conditions was also carried out.

1.1 GENERAL OBJECTIVE

The general objective of this work is to investigate the process of photocatalytic degradation of nitrogen oxides in a flat plate photocatalytic reactor using the Computational Fluid Dynamics Tools (CFD).

1.2 SPECIFIC OBJECTIVES

The overall goal was performed by focusing on specific objectives as outlined below:

- validate a 2D CFD model with the experimental data available in the literature for a flat plate photocatalytic reactor applied to NOx abatement.
- evaluate the performance of the photocatalytic reactor under different conditions of relative humidity, light intensity and inlet NO concentration.
- analyze the behavior of the reactor under different geometric characteristics, varying the channel height (*H*).
- compare the 2D CFD proposed model with the ideal 1D plug flow approach.
- predict the differences between the 3D and 2D CFD models for a flat plate photocatalytic reactor.

1.3 OUTLINE OF THE DISSERTATION

For a better understanding, this dissertation was organized as follows:

Chapter 2 deals with the literature review. Firstly, environmental pollution is presented, focusing on air pollution, air pollutants and nitrogen oxide as the model compound in this work. Then, it discusses conventional air treatment techniques and the use of heterogeneous photocatalysis for NOx abatement. Finally, this chapter covers the work developed in the use of Computational Fluid Dynamics (CFD) for the simulation of gas phase photocatalytic systems.

In Chapter 3, the mathematical modeling and the investigation of photocatalytic degradation of NOx in a flat plate reactor in 2D planar coordinates are presented. This chapter was based on the article entitled "Photocatalytic NOx abatement: Mathematical modeling, CFD validation and reactor analysis", by Jessica Oliveira de Brito Lira, Natan Padoin, Vítor J. P. Vilar and Cíntia Soares, published in Journal of Hazardous Materials (doi.org/10.1016/j.jhazmat.2018.07.009, special issue – Photocatalysis: Future Trends). The computational simulations were performed at Federal University of Santa Catarina (UFSC), within the Laboratory of Materials and Corrosion (LABMAC). The research reported herein consists in the validation of the 2D model developed with the software ANSYS® CFD (Fluent®), considering a comprehensive phenomenological investigation of the effect of different operating conditions, such as relative humidity of the air, initial NO concentration,

and light intensity, on the reactor's performance. Moreover, an analysis of the impact of geometric variations in the photocatalytic reactor and a comparison of the 2D model and the ideal 1D plug flow approach were conducted.

In Chapter 4, an investigation of a flat plate photocatalytic reactor applied to NOx abatement using a three-dimensional (3D) CFD model (also based on ANSYS® Fluent®), and relating it to a 2D approach, is presented. This research was a continuation of the article presented in chapter 3. Essentially, this chapter aims to answer the following question: does the 2D model adequately represents the reactor's performance or a more robust, and computationally intensive, three-dimensional model is required for a proper description of this system?

Finally, Chapter 5 closes the present work with the concluding remarks and perspectives for future work. In the sequence, all references used in this document are listed.

2 LITERATURE REVIEW

2.1 ENVIRONMENT POLLUTION

The environmental pollution is an unfavorable change in the environment around us, totally or largely as a by-product of man's actions (RAI, 2016). This problem is global because it covers both developed and developing countries and has attracted human attention for its serious long-term consequences.

The pollution is commonly accepted as a result of increased industrial activity, the unbridled exploitation of natural resources, the population growth and the ever-increasing industrial waste, reaching critical levels that compromise the balance of the global ecosystem.

In recent decades, a number of sources of pollution have been identified that greatly harm the quality of life. The main types of pollution can be categorized as air, water, soil, noise, visual and thermal pollution. Among these types, air pollution is classified as a real problem to living beings because it is directly related to health problems.

Problems arising from air pollution vary in different parts of the world, but as air quality decreases, human health risks increase, especially in urban areas where air pollution exceeds acceptable limits. In 2016, the World Health Organization (WHO) published a map which indicates the number of deaths attributed to air pollution and reports that only air pollution causes the deaths of 3 million people a year, mainly due to non-communicable diseases (also known as chronic diseases), such as cardiovascular diseases like heart attacks and stroke, cancer, chronic respiratory diseases, and diabetes (WORLD HEALTH ORGANIZATION, 2016a).

Air pollution has been intensified with the increasing growth of industries and automobiles use, which released various pollutants into the atmosphere. According to WHO (2016b), major sources of pollution include fuel combustion from motor vehicles, household fuels and waste burning, oil and coal power plants and industrial activities. However, it is worth noting that there are also natural sources of air pollution, such as sandstorm, volcanic eruptions, and non-criminal forest fires.

Moreover, according to the Health Effects Institute (2018), 95% of the world's population lives in areas that exceed WHO limits to healthy air, and almost 60% live in areas that do not meet even the least stringent quality target stipulated by WHO. The WHO (2016a) reported that no matter geographic or socioeconomic differences, all countries in the world and people of different classes are exposed to air pollution.

Therefore, air pollution must be a public health problem and not just an environmental problem.

Thus, it is clear that air pollution is a serious problem and requires urgent action both at the government level with the regulation and supervision of pollutant gases emissions, as well as in the academic field through the development of new technologies and environmental solutions for the air decontamination.

2.2 AIR POLLUTANTS

Any substance in the air that can harm animals, humans, vegetation and/or materials is called an air pollutant. These can be classified into two groups according to their emission: primary and secondary pollutant (BRAGA *et al.*, 2005).

Primary pollutants are those that are emitted directly into the air from natural sources or sources of human activity. Some of the common pollutants of this group are carbon monoxide (CO), sulfur dioxide (SO_2), nitrogen oxides (NOx), volatile organic compounds (VOC) and some particulate matter (PM).

Secondary pollutants are those that are produced in the atmosphere as a result of the interaction between the primary pollutants in favorable atmospheric conditions. Some of the common pollutants that belong to this group are ozone (O_3), hydrogen peroxide (H_2O_2) and aldehydes (such as formaldehyde).

Among the air pollutants mentioned, the present work uses nitrogen oxides as the model compound.

2.2.1 Nitrogen oxides

The gaseous nitrogen compounds are found mainly in the form of nitrogen oxides (NOx). These are gases formed in the atmosphere due to the chemical interactions between nitrogen and oxygen. This family of oxides mainly includes nitric oxide (NO) and nitrogen dioxide (NO_2).

The NOx can be emitted from natural processes and also human activities. Volcanic activities, transport from high to low atmosphere, and some decomposition processes can emit NOx, for instance. In urban areas, emissions are generally high due to human activities, such as combustion processes generated by industrial installations and automotive vehicles (BOYJOO *et al.*, 2017).

The NOx emissions have a major negative impact on the environment, the human and animal health, and also the vegetation. These

pollutants create several environmental problems that are characterized by the changing acidity of rainwater (acid rain), the formation of a dark cloud made up of atmospheric pollutants (photochemical smog), and the increase in the planet's temperature (greenhouse effect). In addition to the environmental problems, these gases bring innumerable damages to human health, because they can cause from a simple lung discomfort, to pulmonary edemas and even death by asphyxia. High NOx levels can have a negative effect on vegetation which includes leaf damage, reduced growth, and inefficient photosynthesis (LASEK; YU; WU, 2013). Figure 2.1 illustrates the causes and problems related to the emission of nitrogen oxides into the atmosphere. These problems intensify in large metropolises where there is a great concentration of air pollutants. Therefore, it is important to control the NOx emission and to use efficient technologies capable of purifying the air.

Figure 2.1 – Source and problems associated with NOx pollution.

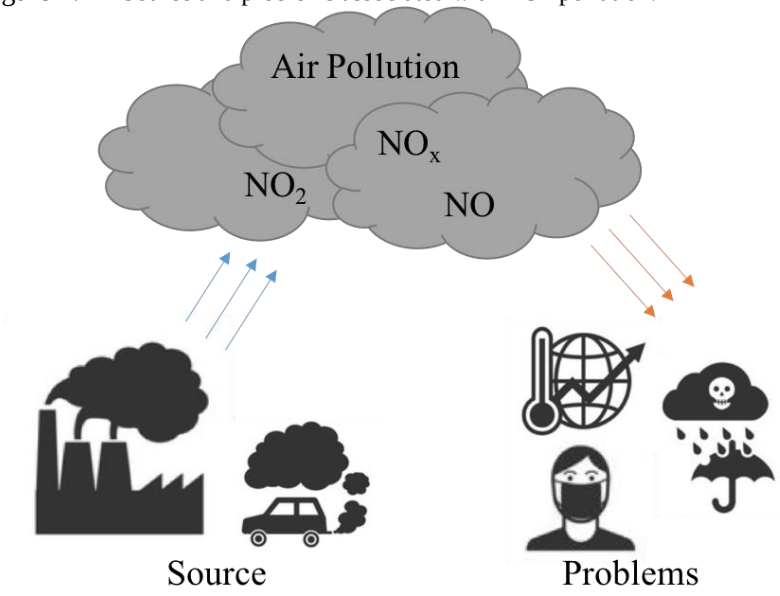

Source: adapted from Ângelo *et al.* (2013).

2.3 CONVENTIONAL TECHNOLOGIES FOR AIR TREATMENT

Atmospheric pollution has been pointed out as one of the greatest problems of modern society. Thus, it is important to develop technologies for air treatment. There is still no generic technology to reduce air pollution because for each situation there is an appropriate solution. The choice of the best pollutant removal strategy is defined based on the cost-benefit ratio and on reaching the objective of interest.

Several techniques have emerged for the air treatment and can be classified into two types: non-destructive and destructive (PENCE, 2012; WANG; PEREIRA; HUNG, 2004).

Non-destructive techniques are those that only make the separation or containment of the pollutant of interest. These techniques aim to transfer the polluting compounds of the gas phase to another phase, which may be liquid or solid. Examples of the non-destructive technique for the air treatment are condensation, which consists in collecting the compounds at a temperature below of their boiling point and passing them to the liquid phase; absorption, in which some liquid (water, oil, or other) is used to absorb the air pollutants; and adsorption which use some sorption material (activated carbon, silica gel and clays, for example) to adsorb the air pollutants from the gaseous phase (LIM *et al.*, 2009; ROCHETTO, 2012). It is noted that conventional non-destructive methods of air pollution still require post-processing to discard the waste material or to regenerate the adsorbent material, which is the biggest disadvantage of these techniques. This is explained by the fact that they are based only on the phase transfer of the pollutant.

On the other hand, the destructive techniques lead to the degradation of the pollutants forming compounds less harmful to the environment. Examples of destructive techniques can be cited as the biological treatment with biofilms that use microorganisms for degradation of organic compounds, the thermal incineration, which use high temperatures for the destruction of pollutants and the advanced oxidative processes (AOP), which use highly reactive intermediate chemical species as chemical oxidants in the degradation of pollutants (LIM *et al.*, 2009; ROCHETTO, 2012).

Among the advanced oxidative processes, heterogeneous photocatalysis has been widely studied for the degradation of air pollutants, mainly NOx (ÂNGELO *et al.*, 2013; BOYJOO *et al.*, 2017; LASEK; YU; WU, 2013; ROY; MADRAS, 2015).

2.4 HETEROGENEOUS PHOTOCATALYSIS

Heterogeneous photocatalysis was discovered by Fujishima and Honda in 1972, when they performed an experiment using TiO_2 in a photo-electrochemical cell in the presence of ultraviolet (UV) radiation and a platinum electrode. The authors suggested that water was decomposed into oxygen and hydrogen. From this time, many researchers were devoted to the understanding and application of photocatalytic processes in both liquid phase and gas phase.

Heterogeneous photocatalysis occurs in the presence of a semiconductor catalyst. It is usually in a solid phase that forms a system of more than one phase. Among the semiconductors, titanium dioxide (TiO_2) has been extensively applied as a catalyst due to its high physicochemical stability, non-toxicity, good photo-generation of highly oxidizing radicals and low cost (FUJISHIMA; RAO; TRYK, 2000; FUJISHIMA; ZHANG, 2006).

The principle of heterogeneous photocatalysis involves the exposure of the catalyst (TiO_2) to light (solar or artificial). TiO_2 is a semiconductor, which consists of a valence band (VB) and a conduction band (CB), separated by a region called bandgap (the minimum amount of energy required to excite an electron, E_{BG}, which for the TiO_2 anatase phase is 3.20 V) (CARP; HUISMAN; RELLER, 2004). When the semiconductor is irradiated with photons (*hv*) with energy equal or greater than its bandgap energy, it absorbs these photons and results in the excitation of the electrons of the VB to the CB, generating a positive hole (h^+) in the VB, as shown in Figure 2.2.

The excited electrons react with the oxygen molecules and form the superoxide anion ($O_2^{\cdot -}$). The holes have a sufficiently positive potential for generating hydroxyl radicals ($OH^{\cdot -}$) by interacting with water molecules on the surface of the catalyst. These free radicals formed are powerful oxidants and can attack some organic and inorganic compounds, causing their decomposition (ÂNGELO *et al.*, 2013; LASEK; YU; WU, 2013; OCHIAI; FUJISHIMA, 2012; ZHONG; HAGHIGHAT, 2015).

Figure 2.2 – Mechanism of heterogeneous photocatalysis.

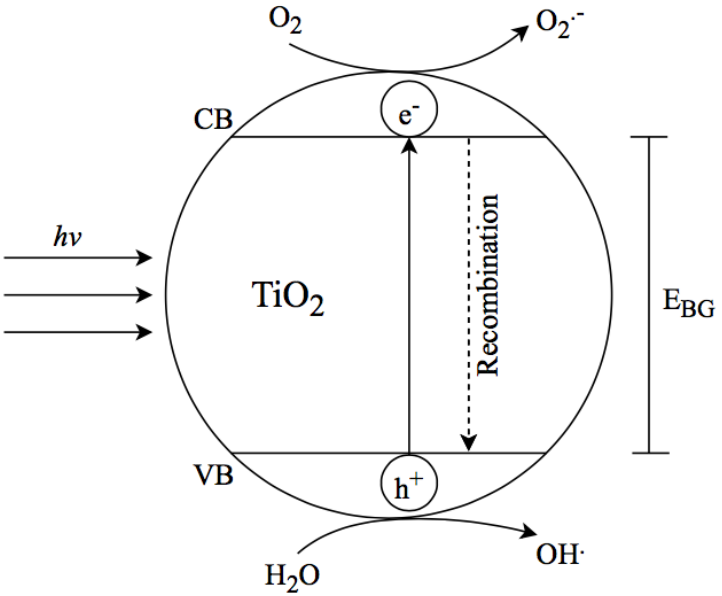

Source: adapted from Ângelo *et al.* (2013).

A wide variety of toxic compounds are susceptible to degradation by heterogeneous photocatalysis, making it a promising technology. Numerous studies report the use of heterogeneous photocatalysis mainly for the treatment of aqueous effluents. For example, industrial and agro-industrial waste, rivers, and lakes contaminated with organic, inorganic and microbial pollutants (BYRNE; SUBRAMANIAN; PILLAI, 2018; RODRIGUEZ-NARVAEZ *et al.*, 2017) can be treated by this technology.

Besides the aqueous phase decontamination, heterogeneous photocatalysis has been also used for the destruction of several classes of compounds in the gas phase with great efficiency. This technology is extremely important in several environmental sectors focused on gases such as the decontamination of confined environments, bad odor elimination due to the presence of volatile organic compounds and treatment of atmospheres contaminated with gases originating from chimneys and automobiles.

Several studies have been done using heterogeneous photocatalysis for the abatement of gas phase pollutants. Many of them have focused on the degradation of different pollutant types, such as nitrogen oxides (pollutant model of this dissertation) as well as volatile

organic compounds (SHAYEGAN; LEE; HAGHIGHAT, 2018), carbon monoxide (KOWSARI; ABDPOUR, 2017), sulfur dioxide (KOWSARI; ABDPOUR, 2016), and others. Other studies investigate the kinetic model and the optimal conditions for the process, evidencing the main factors that influence the degradation of a pollutant. Moreover, studies on new and/or improved photocatalysts are the subject of scientific discussions in order to obtain better photocatalytic activity compared to the pristine titanium dioxide catalyst.

2.4.1 Strategies for NOx degradation using heterogeneous photocatalysis

Heterogeneous photocatalysis has become an active research area in air purification. Due to the large NOx emissions in the environment and its negative impact especially on humans, several studies were conducted towards the application of heterogeneous photocatalysis for NOx abatement. The use of this technology for environmental remediation has been done by the impregnation of TiO_2 in building materials such as concrete, asphalt, and paints, making them known as photocatalytic materials.

The addition of the photocatalyst in building materials, such as concrete, generates environmentally sustainable materials applied to the degradation of air pollutants. According to Jimenez-Relinque *et al.* (2015) and Trichês *et al.* (2010), the concrete structures have excellent characteristics to be used as photocatalytic support since they exhibit a flat surface, making them suitable for applying the photocatalytic material, and for facilitating the exposure of sunlight. Moreover, the concrete has a porous structure and alkaline pH, compatible with TiO_2. Additional studies also evaluate the photocatalytic activity in ceramic materials for NOx degradation (ÂNGELO; ANDRADE; MENDES, 2014; HERNÁNDEZ RODRÍGUEZ *et al.*, 2016; HÜSKEN; HUNGER; BROUWERS, 2009; SEO; YUN, 2017; TRICHÊS *et al.*, 2010).

Recently, photocatalytic cementitious materials were patented by Murata *et al.* (1999) (Mitsubishi Materials Corporation), as well as Cassar e Pepe (2006) (Italcementi S.p.A). The first one comprises the application of TiO_2 to concrete blocks with improved NOx cleaning ability. The second patent, owned by Italcementi S.p.A, covers the application of photocatalyst particles in tiles to degrade pollutants present in the environment. Furthermore, new commercial blocks of cement are being developed for air pollutant degradation, especially for NOx. Among the different products available on the market, NOxer® technology by

Mitsubishi and TX Active®, TX Aria®, and TX Arca® technologies by Italcementi (FOLLI *et al.*, 2012; PAZ, 2010) can be highlighted.

Despite the existence of photocatalytic concretes, when it comes to roads in large cities, it is common to apply asphalt paving as the main form of the coating. Therefore, another material widely used in NOx degradation processes is photocatalytic asphalt pavements. This material was developed to solve pollution problems caused by the exhaustion of automobiles in big cities (CAO *et al.*, 2017; CHEN; LI; YUAN, 2007; CHEN; LIU, 2010; HASSAN *et al.*, 2013; LIU *et al.*, 2015; SEGUNDO *et al.*, 2018).

Another building material also largely used for the photocatalytic NOx degradation process are the paints. The great advantage of photocatalytic paints is that almost all surfaces of urban areas can be painted. So, this material becomes quite attractive for photocatalysis (ÁGUIA *et al.*, 2010, 2011; ALLEN *et al.*, 2005; ÂNGELO; ANDRADE; MENDES, 2014; GANDOLFO *et al.*, 2015; LAUFS *et al.*, 2010; MAGGOS *et al.*, 2007a, 2007b).

In general, numerous studies using photocatalytic construction materials are being reported in the literature for NOx degradation. In these works, besides to approach the main issue of air pollution, some of them also deal with several factors that positively or negatively affect the efficiency of NOx degradation.

2.4.2 Operating conditions effects

The photocatalytic NOx degradation efficiency is strongly dependent on various operating conditions as initial pollutant concentration, relative humidity of the air and light intensity. Details of some of these factors are described below.

2.4.2.1 Initial pollutant concentration

The inlet NO concentration has a very important effect on photocatalytic activity. Several authors have observed that low values of initial NOx concentration favor the increase of NOx degradation (ÂNGELO *et al.*, 2013; DEVAHASDIN *et al.*, 2003; MARTINEZ *et al.*, 2011; YU; BROUWERS, 2009).

Ballari, Yu and Brouwers (2011) evaluated the effect of varying the inlet NO concentration (0.1, 0.5 and 1 ppm), while maintaining constant other parameters such as relative humidity (50%) and light intensity (10 $W \cdot m^{-2}$) in concrete paving samples. These authors found a

NO conversion of approximately 83%, 62% and 43%, respectively. Thus, they concluded that, as expected, by lowering the initial concentration of the pollutant, the reaction conversion increases.

Other studies by Yu and Brouwers (2009) used carbon-doped TiO_2 as a photocatalyst. The authors obtained degradation of 60.76% for the initial NO concentration of 0.1 ppm, while a conversion of 15.88% was reached for the initial concentration of 1 ppm. The experiments were conducted using a flow rate equals to 3 $L \cdot min^{-1}$, relative humidity of 50% and light intensity equivalent to 10 $W \cdot m^{-2}$. Hüsken, Hunger and Brouwers (2009) confirmed the findings by Yu and Brouwers (2009). They concluded that high values of inlet pollutant concentrations result in lower oxidation rates; therefore, low initial concentrations result in enhanced degradation performance.

Wang *et al*. (2007) evaluated the behavior of a photocatalytic process applied to NOx abatement under high initial concentrations (15 – 147 ppm). It was observed that the NO conversion reached 85% at the initial concentration of 15 ppm. However, when the concentration increased to 147 ppm, the conversion dramatically decreased to 27%.

Similar results were obtained by Devahasdin *et al.* (2003). The authors found 70% of NO conversion when its concentration at the reactor's inlet was set to 5 ppm. Conversely, a NO conversion as low as 10% was observed when its feed concentration was increased to 60 ppm.

In fact, the effect of the initial pollutant concentration has been studied by many authors. It can be explained by assuming that the heterogeneous photocatalytic reaction is controlled by the adsorption step of the pollutant at the photocatalyst's surface. Therefore, for high initial concentrations, there will be saturation of the catalyst's active sites and, consequently, a decrease in the degradation rates is expected.

2.4.2.2 Relative humidity

Relative humidity has a very important role in the heterogeneous photocatalytic degradation of NOx. The water (moisture) is responsible for the generation of the hydroxyl radicals on the surface of the catalyst, crucial for the pollutant abatement. Therefore, several authors have studied and reported how relative humidity influences NOx degradation (BALLARI; YU; BROUWERS, 2011; CHEN; LIU, 2010; HASSAN *et al.*, 2013; HERNÁNDEZ RODRÍGUEZ *et al.*, 2016; LAUFS *et al.*, 2010; SEO; YUN, 2017).

Different arguments were found on the influence of this parameter on NOx photocatalysis using TiO_2 as photocatalyst. According to Devahasdin *et al.* (2003), the NO conversion increased from 0 to 35% when the relative humidity increased from 0 to 50%, and this conversion remained constant, equal to 35%, when the relative humidity was further increased to RH=75%. In all cases, the NO concentration at the reactor's inlet was maintained at 40 ppm. The same behavior was observed by Wang *et al.* (2007) when they evaluated the effect of increasing the relative humidity (10-100%) on the photocatalytic abatement of NOx. The authors observed that the conversion increased from 40% to approximately 60% for RH in the range of (10-60)%, and it remained constant (60%) when the relative humidity was further increased to RH=100%. These experiments were also performed with the inlet NO concentration fixed at 40 ppm. A comprehensive explanation about this behavior was not provided by the authors.

Martinez *et al.* (2011) showed that when combining variations of the relative humidity in the range of (0-74)% and NO concentration at the reactor's inlet in the range of (400-1000) ppb, no significant influence was observed in the NO conversion. Moreover, the authors have shown that the degradation rate increases with increasing NO concentration (1500 and 2000 ppb) at relative humidity levels below 20%. At moisture levels above 20%, the degradation rates for NO concentrations of 1500 and 2000 ppb were constant. This behavior was justified by two hypotheses: (i) the photocatalytic reaction is not limited by the competition with water in the photoactive sites at high humidity rates, and (ii) the lack of oxygen reactive species due to insufficient humidity in the air hinders the photocatalytic degradation of NO at high pollutant concentrations. The influence of initial NO concentration and the relative humidity in the NO degradation rate was similar on glass and mortar substrate.

Seo and Yun (2017) evaluated the NOx removal rate under wet conditions with varying relative humidity values (5, 15, 25, 35 and 50%). They observed that increasing the relative humidity results in a linear decrease in the NOx degradation rate. The same behavior was also obtained by Ballari, Yu and Brouwers (2011), which varied the relative humidity from 10% to 70%. They observed that the photocatalytic NO degradation is low for high relative humidity values. Additionally, Hüsken, Hunger and Brouwers (2009) evaluated the influence of the relative humidity on cement samples, and they stated that this influence also depends largely on the material type. According to these authors, for high values of relative humidity, the hydrophilic effect on the surface

prevails over the photocatalytic effect. Melo e Trichês (2012) also reported decreasing photocatalytic activity when increasing the relative humidity.

The effect of relative humidity on the rate of NOx photocatalytic abatement was explained by Ballari *et al.* (2010). The authors explained that increasing the relative humidity leads to saturation and competition between the molecules of water and pollutant by the active sites on the photocatalyst's surface. Indeed, it would prevent the molecules of pollutant from being adsorbed on the surface and, thus, the degradation reaction is impaired or does not occur.

2.4.2.3 Light intensity

Heterogeneous photocatalytic processes are based on the activation of a photocatalyst by light. Once photons with sufficient energy are absorbed by the photocatalyst, electron-hole pairs are formed in the material and, as a consequence, the degradation reaction of the pollutant occurs. So, another factor that affects the photocatalytic activity is the irradiation intensity (solar or UV), which is essential to the formation of the oxidative radicals and, consequently, to the degradation of NOx (MELO; TRICHÊS, 2012; TSENG; HUANG, 2012; WANG *et al.*, 2017; YU; BROUWERS, 2009).

According to Yu and Brouwers (2009), light intensity influences the photocatalytic process because the number of photons produced increases as the light intensity becomes higher. This fact was also evidenced by Obee and Brown (1995), who reported the direct proportionality between the rate of pollutant oxidation and the UV light intensity. Therefore, a high light intensity is capable of producing a high number of electron-hole pairs that will participate in the oxidation and reduction reactions during the photocatalytic phenomenon, resulting in increased pollutant degradation.

Murata, Kamitani and Takeuchi (2000) observed that NOx conversion increased from 5% to 40% when increasing the UV light intensity from 1 $W \cdot m^{-2}$ to 12 $W \cdot m^{-2}$, considering a NO concentration of 1 ppm at the reactor's inlet. The same range was used by Yu and Brouwers (2009) for visible light with carbon-doped catalyst, and the NOx conversion reached up to 25%. Both studies found a non-linear behavior between NOx conversion and light intensity. On the other hand, Ballari *et al.* (2010), Hüsken, Hunger and Brouwers (2009) and Sikkema, Ong and Alleman (2015) observed a purely linear behavior between these parameters.

Chen and Liu (2010) found that under a UV intensity of 0–1 $mW \cdot cm^{-2}$, the photocatalytic reaction rate increased linearly with light intensity. However, from 2–4 $mW \cdot cm^{-2}$, the reaction rate increased with the square root of light intensity. The authors proposed an explanation on how the photocatalytic pollutant abatement is related to the irradiation, dividing the phenomenon into two categories: (i) a first-order regime, where the electron-hole pairs are consumed more rapidly by the chemical reactions than by the recombination reaction; and (ii) a half-order regime, where the rate of recombination of the electron-hole pairs is the dominant process. A similar behavior was found by Lim *et al.* (2000). Although there is consensus that this division into two categories exists, there is no agreement about the critical value of the light intensity that divides these categories. Overall, the published works have noted that a linear relationship is more applied under low irradiation conditions, while a nonlinear relationship is valid for high irradiation conditions (HÜSKEN; HUNGER; BROUWERS, 2009; IMOBERDORF *et al.*, 2005; JACOBY *et al.*, 1995; SIKKEMA; ONG; ALLEMAN, 2015).

2.5 CFD APPLIED TO GAS PHASE PHOTOCATALYTIC PROCESSES

Computational Fluid Dynamics (CFD) can be defined as the science of predicting flow behavior, heat transfer, mass transfer, chemical reaction and other associated phenomena (DURAN, 2010). It makes use of different algorithms and numerical methods to analyze and solve problems of several areas, including the fields of chemical engineering and chemical reaction engineering. This technology provides insights into flow properties that would be difficult, expensive or impossible to study using traditional techniques (analytical solutions and physical experiments, for instance).

Thus, in the context of heterogeneous photocatalysis applied to the abatement of gaseous pollutants, CFD has been shown to be useful for the analysis of the flow characteristics and the reactor performance. This technique enables a detailed analysis of the fluid dynamics and local effects of parameters of interest. Typical problems in the field of heterogeneous photocatalysis may involve the solution of mass conservation (continuity equation), momentum conservation (Navier-Stokes equations), chemical species conservation, reaction rates, as well as radiative transport.

Therefore, different types of photocatalytic reactors were investigated using CFD codes, such as flat plate reactor (VERBRUGGEN; LENAERTS; DENYS, 2015), corrugated plate reactor (PASSALÍA *et al.*, 2011; ZHANG, 2013), annular reactor (TAGHIPOUR; MOHSENI, 2005), multi-tube reactor (ROEGIERS; VAN WALSEM; DENYS, 2018; VAN WALSEM *et al.*, 2016), among others.

Several studies have been devoted to the modeling of photocatalytic systems for different applications. Taghipour and Mohseni (2005) simulated two photocatalytic reactors (flat plate and annular) with surface reaction for the trichloroethylene oxidation. The authors analyzed variations in different parameters, such as initial pollutant concentrations, flow rates, and reactor length, aiming to better understand of the flow characteristics and to evaluate reactor performance. The simulations were carried out using ANSYS® CFD (Fluent®), version 6.0, considering a three-dimensional model, steady state, laminar flow and photocatalytic surface reaction based on first-order kinetics. The results showed that, for both reactors, the CFD model provided detailed information on the contaminant concentration gradients along the reactor. Moreover, the model provided crucial information for the improvement of the reactor's performance. Mohseni and Taghipour (2004) used two approaches (CFD and experiments) for the study of the removal of vinyl chloride in the gas phase in an annular photoreactor. The authors investigated the flow field and the photocatalytic reaction of the compound in air using ANSYS® CFD (Fluent®). They reported that the model presented good agreement with the experimental data.

Tomasic, Jovic and Gomzi (2008) compared the performance of one-dimensional (1D) and two-dimensional (2D) models for toluene degradation in a continuous annular photocatalytic reactor. The catalyst (TiO_2) was coated on the inner wall of the reactor, and the device was illuminated internally by a fluorescent lamp. The authors concluded that the 2D model led to a better representation of the reactor than the 1D model. Both models were compared with the experimental data.

Gauvin *et al.* (2018) used CFD to simulate airflow in a reactor applied to NOx removal by photocatalytic oxidation aiming to understand the differences in the flow behavior when two different substrates were used (open pore structure given by wood-wool cement board and closed pore structure given by autoclaved aerated concrete). The simulations were conducted in two dimensions (2D) using the software Flowsquare 4.0, reconstructing the substrate pore structures. It was observed that the CFD simulations confirmed the importance of the pore structure in the

photocatalytic oxidation efficiency. A similar study was developed by Zhang, Stefanakos and Goswami (2013), who investigated the improvement of photocatalytic efficiency by introducing artificial roughness to the reactor's surface. The effects of five different forms of roughness elements (square, triangle, semi-round, round, and chamfered) were studied. The simulations were developed in two dimensions (2D) using the software ANSYS® CFD (Fluent®), version 13.0. The authors observed that there was an improvement in the reaction rate with the addition of the roughness elements on the surface of the reactor. The best form was the isosceles triangle.

Additionally, many studies have used CFD to determine kinetic parameters. Verbruggen, Lenaerts and Denys (2015) used two methods (analytical and CFD) to determine the Langmuir-Hinshelwood-Hougen-Watson (LHHW) kinetic parameters for acetaldehyde oxidation in a flat plate photocatalytic reactor. The authors showed that the analytical model based on mass transfer and the CFD approach accurately provided the kinetic parameters. Verbruggen *et al.* (2016) continued the acetaldehyde oxidation studies, but with a different objective – to determine the adsorption parameters of the pollutant in a photocatalytic fiber reactor. The simulations were carried out with the commercial software COMSOL® Multiphysics, version 4.4, in steady state and also time dependent. It is worth mentioning that the authors used the Darcy-Forcheimer equation to model the velocity and air pressure fields in the glass fiber, considering single-phase flow in the porous medium. The authors proved that CFD is an accurate tool for extracting all relevant adsorption parameters.

Van Walsen *et al.* (2016) used CFD to model a new multi-tube reactor applied to the degradation of acetaldehyde (reaching conversions >90%). The CFD model was developed to determine the concentrations of the pollutant and to estimate the adsorption and desorption constants in the transient regime. The simulations were conducted in COMSOL® Multiphysics, version 5.1, considering laminar flow, incompressible fluid and modeling of the acetaldehyde transport through the time-dependent advection-diffusion equation. The input data of the CFD model was obtained from experiments. The authors concluded that the CFD simulations showed excellent agreement with the experimental data with high capacity to calculate the adsorption and desorption constants independently. Following the studies on the performance of multi-tube photocatalytic reactors, Roefiers, Van Walsem and Denys (2018) modeled the radiation field coupled with reaction kinetics and fluid dynamics in order to simulate the transient transport of acetaldehyde

along the reactor. As a result, the authors were able to optimize some parameters of the reactor, i.e., the refractive index and the thickness of the photocatalyst layer.

It should be highlighted that the modeling of the radiation field within photocatalytic reactors has a significant contribution to the design of the devices considering different configurations. Salvadó-Estivill, Hargreaves and Li Puma (2007) used CFD to simulate the oxidation of trichloroethylene in a flat plate photocatalytic reactor considering the modeling of the radiation field in their analyses. In this study, the linear source spherical emission model (LSSE) was used to explore the effect of the incident radiation intensity at any position on the surface of the photocatalytic plate. Furthermore, Boyjoo, Ang and Pareek (2014) used CFD to investigate the fluid flow behavior and the radiation transport in a pilot scale photocatalytic slurry reactor. The multiphase flow was solved using the granular Eulerian model, while the solution of the radiative transport equation (RTE) was performed using the discrete ordinates model (DOM). Pareek *et al.* (2003) also used CFD and the DOM radiation model to simulate immobilized photocatalytic reactors. Similarly, Chong *et al.* (2011) used CFD to simulate a monolith reactor applied to the oxidation of toluene and formaldehyde in which the radiation field was modeled with DOM and the oxidation rate was described by the Langmuir-Hinshelwood-Hougen-Watson (LHHW) kinetic model.

Wang *et al.* (2012) used CFD to model odor abatement (taking dimethyl sulfide as model compound) in a photocatalytic flat plate reactor irradiated with UV-LEDs. The LED emission model was coupled to the reaction kinetics of LHHW type (with parameters determined experimentally) and to the gas flow dynamics model within the reactor. The authors found good agreement between the CFD predictions and the experimental data. Khodadadian *et al.* (2018) also investigated the use of LED in photocatalytic processes. Again, the authors used CFD to simulate the coupled fluid flow, radiation field and reaction kinetics of LHHW type in an annular LED-based photocatalytic reactor for toluene degradation. The model was successfully validated based on the experimental data for a wide range of operating conditions (different initial pollutant concentrations, irradiance, relative humidity and residence time).

In this context, it is important to highlight that many studies were carried out regarding the use of CFD to simulate gas phase heterogeneous photocatalysis. Several paths can be traced in this topic, either to obtain process improvements from variations in operating conditions or to investigate the behavior of the reactor under conditions that are not easily obtained through experimentation. Moreover, researches working on

CFD modeling of gas phase heterogeneous photocatalysis have explored a variety of scenarios, as seen above. Examples include the use of different types of reactors, the photocatalytic degradation of several gaseous contaminants, as well as different applications of this technology.

In this sense, it is evident that many studies were studied when associating CFD to the heterogeneous photocatalysis process in the gas phase. However, when we linked CFD to the photo-abatement of NOx, few studies were investigated, which motivated the development of this work.

2.5.1 Computational Fluid Dynamics

Many industrial and academic organizations invest large amounts of resources to develop new technologies in the area of computational fluid dynamics. Thus, they acquire a software package capable of simulating different conditions. As there is a growing commercial market for these programs, there are several available. Examples may be cited: ANSYS-CFX®, COMSOL Multiphysics®, ANSYS-Fluent®, CHAM-Phoenics®, Star-CD® and Flow3D®, among others (TU; YEOH; LIU, 2008).

Each software package aimed at the CFD market must assist the user in performing the tasks that form the analysis process. Then, it is necessary to follow a series of basic steps to set up and solve the problem to get a CFD solution. Therefore, this is done by providing three main parts of the software, such as a pre-processor, a solver, and a post-processor (RANADE, 2002; TU; YEOH; LIU, 2008; VERSTEEG; MALALASEKERA, 2007). Figure 2.3 shows the structure that illustrates the interconnectivity between these three elements within the CFD analysis.

Figure 2.3 – Structure of the three main elements in CFD analysis.

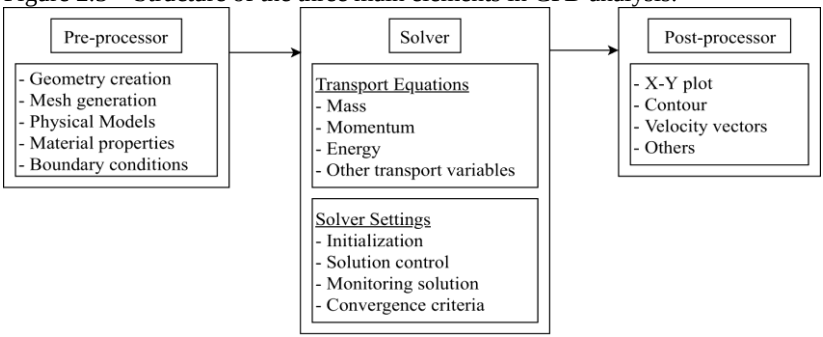

Source: adapted from Tu, Yeoh and Liu (2008).

The increasing interest in using CFD as a practical tool currently found in almost every field, from medical research to modern engineering. Thus, there are many advantages associated with the use of computational fluid dynamics, such as (TU; YEOH; LIU, 2008):

- CFD complements the experimental and analytical approaches, showing an alternative and economical way of simulating the actual fluid flow;
- CFD has the ability to simulate different conditions, such as beyond their limits, or processes that can not be easily tested.
- CFD provides pretty detailed and comprehensive information about the flow behavior compared to experimental fluid dynamics.

Despite the advantages, CFD techniques present limitations such as the need for model validation, high memory demand and speed in calculations, especially when the Reynolds number is high and a very refined numerical mesh is required. Although the use of CFD encounters such limitations, this technology is still widely used in the application of chemical engineering processes, mainly in the simulation of chemical reactors. In this sense, few papers report the application of CFD to the NOx photocatalytic abatement, which motivated the present work.

3 PHOTOCATALYTIC NOx ABATEMENT: MATHEMATICAL MODELING, CFD VALIDATION AND REACTOR ANALYSIS

This chapter is based on the paper entitled “Photocatalytic NOx abatement: Mathematical modeling, CFD validation and reactor analysis” (Journal or Hazardous Materials, doi.org/10.1016/j.jhazmat.2018.07.009, special issue – Photocatalysis: Future Trends), by Jéssica Oliveira de Brito Lira, Natan Padoin, Vítor J. P. Vilar and Cíntia Soares.

3.1 INTRODUCTION

According to the World Health Organization, approximately 3 million people die every year worldwide due to atmospheric pollution (see Figure A.1 in Appendix A) (WORLD HEALTH ORGANIZATION, 2016a). In fact, this is a problem that affects people from different geographical regions and classes, so, far from an environmental concern, it has turned into a public health issue (WORLD HEALTH ORGANIZATION, 2016a).

Nitrogen oxides, commonly denoted as NOx, are among the species with increased concern. NOx can be emitted by natural processes as well as human activity. Some common sources include volcanic activity, atmospheric transport, combustion processes and emissions from industries and vehicles (BOYJOO *et al*., 2017).

Among the adverse consequences derived from NOx at the atmosphere one can highlight acid rains, smog and contribution to greenhouse effect. Moreover, it can cause health problems like pulmonary edema in human beings and be prejudicial to photosynthesis in vegetables (LASEK; YU; WU, 2013).

Based on this scenario, strict regulations have been adopted worldwide to control the concentration of NOx within acceptable limits (see Table A.1 in Appendix A). In Brazil, for instance, the National Council for the Environment (CONAMA), through the resolution n. 03 from 06/28/90, established a maximum NO_2 concentration of 320 $\mu g \cdot m^{-3}$ at the atmosphere during a sampling interval of 1 h (CONAMA, 1990).

Therefore, technologies to prevent and mitigate NOx emissions to the atmosphere are highly necessary. In terms of mitigation, heterogeneous photocatalysis has been considered a suitable alternative which can degrade NO through the following generic mechanism (PÉREZ-NICOLÁS *et al*., 2017):

$$TiO_2 + h\nu \rightarrow TiO_2\ (e^- + h^+) \quad (3.1)$$

$$O_2 + e^- \rightarrow O_2^{\cdot -} \quad (3.2)$$

$$H_2O + h^+ \rightarrow H^+ + HO^{\cdot} \quad (3.3)$$

$$NO + O_2^{\cdot -} \rightarrow NO_3^- \quad (3.4)$$

$$NO + HO^{\cdot} \rightarrow HNO_2 \quad (3.5)$$

$$HNO_2 + HO^{\cdot} \rightarrow NO_2 + H_2O \quad (3.6)$$

$$NO_2 + HO^{\cdot} \rightarrow NO_3^- + H^+ \quad (3.7)$$

where TiO_2 (titanium dioxide) is the semiconductor (photocatalyst), hν represents an incident photon with energy higher than the bandgap of the photocatalyst, e^- and h^+ are the photogenerated electron and hole, respectively; $O_2^{\cdot -}$ represents superoxide anion and $HO^{\cdot}$ is the highly oxidative hydroxyl radical.

When impregnated in a support material, a photocatalyst can be suitably used to carry out a green process for NO degradation using light as activator. Concrete, for instance, can be used as a porous structure for the deposition of titanium dioxide (ÂNGELO; ANDRADE; MENDES, 2014; HERNÁNDEZ RODRÍGUEZ *et al*., 2016; HÜSKEN; HUNGER; BROUWERS, 2009; JIMENEZ-RELINQUE *et al*., 2015; SEO; YUN, 2017).

It is well known that operational factors such as initial concentration of pollutant, flow rate, irradiation intensity and relative humidity have significant impact on the efficiency of photocatalytic systems applied to NO abatement (DEVAHASDIN *et al*., 2003; HÜSKEN; HUNGER; BROUWERS, 2009; MARTINEZ *et al*., 2011; YU; BALLARI; BROUWERS, 2010).

Low initial concentrations of NO were found to enhance the efficiency of the photocatalytic process (DEVAHASDIN *et al.*, 2003; MARTINEZ *et al.*, 2011). Yu and Brouwers (2009) showed that ~61% of NO degradation was reached when an initial concentration of 0.1 ppm was used (NO consumption rate of ~1.3×10^{-10} mol·s^{-1}), while a yield of ~16% was obtained when the concentration was increased to 1.0 ppm (rate of ~3.3×10^{-10} mol·s^{-1}). Similar results were found by Devahasdin *et*

al. (2003). The authors reached a NO conversion of 70% when operating with an initial concentration of 5 ppm, while a yield of 10% was obtained for a concentration of 60 ppm.

Keeping the residence time constant, more molecules adsorb at the catalyst surface as the pollutant concentration is increased at the reactor inlet (due to the higher driving force resulting from higher difference of concentration between the bulk and the catalyst surface), but a maximum reaction rate is reached since the rate of radicals generated at the surface becomes the limiting step and the higher concentration of NOx may result in lower adsorption of water molecules and blockage of the catalyst surface (ÂNGELO *et al*., 2013).

The relative humidity has reportedly significance on the conversion reached in photocatalytic reactors for NOx treatment (BALLARI *et al.*, 2010; HERNÁNDEZ RODRÍGUEZ *et al.*, 2016; SEO; YUN, 2017). Seo and Yun (2017) varied the relative humidity (5, 15, 25, 35 and 50%) and found the NO conversion decreased as the RH increased. Ballari *et al.* (2010) also varied the relative humidity in the range 10–70% and found low conversions at high values of RH. On the other hand, Martinez *et al.* (2011) did not found significant effect on the NO conversion when working with a combining variation of the relative humidity in the range 0–74% and initial concentration in the range 400–1000 ppb.

The high oxidative hydroxyl radical ($HO^{\cdot}$) is generated by the reaction between the adsorbed water molecules at the catalyst surface and the holes (h^{+}) resulting from the semiconductor activation by light, according to Eqs. 3.1 and 3.3. Therefore, a higher number of hydroxyl radicals are expected to be generated at the catalyst surface (resulting in enhanced reaction rates) as the relative humidity is increased, but this process is limited by the competitive adsorption of water and pollutant molecules on the active sites (depending on the pollutant/water molar ratio) (ÂNGELO *et al*., 2013). Consequently, the NO conversion can effectively reduce as the water content increases within the photoreactor.

Irradiation intensity (with adequate wavelength to activate the NO photocatalyst) also has significant effect on NO degradation (TSENG; HUANG, 2012; WANG *et al.*, 2017). Essentially, the rate of NO degradation increases non-linearly as the irradiation intensity is increased.

Although several studies have been reported at the laboratorial scale, few contributions have dealt with the application of photocatalytic concrete in large scale. Gallus *et al*. (2015) evaluated NOx degradation at Leopold II tunnel (Brussels, Belgium) and found a maximum conversion of 2%, which can be related to experimental uncertainties. The influence

of factors such as high concentration of pollutant, high values of relative humidity and the wind speed inside the tunnel were considered as drawbacks for the effectiveness of this system. Moreover, insufficient illumination (low irradiance) may be attributed as a significant factor for the inefficiency of this system.

Independently from the scale considered, though, the theoretical characterization of the problem is highly relevant in terms of reactor design, analysis and optimization. Once a model is validated, phenomenological investigations and evaluation of scale-up (or scale-out) strategies can be readily carried out. However, for a complete description of the coupled fluid flow and mass transport (ideally considering irradiation distribution as well) in photocatalytic reactors a set of nonlinear partial differential equations must be solved, which can be reached through numerical methods (IMOBERDORF *et al*., 2007; LI PUMA *et al*., 2009; LOPES *et al*., 2012). Photocatalytic reactor modeling also can be performed by Monte Carlo (MC) method and computational fluid dynamics (CFD) techniques. The MC method (LOPES *et al*., 2012; SINGH; SALVADÓ-ESTIVILL; LI PUMA, 2007) is a statistical technique that allows predicting the light distribution inside a photoreactor and eventually the estimated absorption coefficients can be an input parameter for the CFD modeling of a photocatalytic reactor (WANG; TAN; YU, 2014a).

CFD software can reproduce the photocatalytic reactor geometry with its exact dimensions and allows to solve the hydrodynamics and radiation transport and is particularly useful when ideal flow conditions cannot be assumed. In this sense, CFD codes are effective tools for the simulation of the reactive flow within photocatalytic devices considering all the coupled phenomena taking place. CFD has been used to model different photoreactors types: annular (MOHSENI; TAGHIPOUR, 2004; TAGHIPOUR; MOHSENI, 2005), flat plate (SALVADÓ-ESTIVILL; BRUCATO; LI PUMA, 2007), corrugated plate (PASSALÍA *et al*., 2011), impeller (TOKODE *et al*., 2017), multi-tube (ROEGIERS; VAN WALSEM; DENYS, 2018) and many others as reported by Boyjoo and co-workers.

In this work, a computational model, based on CFD code, for photocatalytic abatement of NOx was validated with experimental data available in the literature. Moreover, a comprehensive analysis of the photocatalytic reactor was carried out, highlighting the advantages of the model implemented herein when compared to the ideal plug flow approach.

3.2 METHOD

3.2.1 Mathematical model

The mathematical model consisted of a system of nonlinear partial differential equations describing single-phase fluid flow and multicomponent species transport in steady state. The overall mass conservation was calculated according to Eq. 3.8 (BIRD; STEWART; LIGHTFOOT, 2007):

$$\frac{\partial}{\partial x}(\rho v_x) + \frac{\partial}{\partial y}(\rho v_y) = 0 \tag{3.8}$$

where x and y are Cartesian coordinates, ρ is the mixture density, and v_x and v_y are the *x*- and *y*-velocity components, obtained from the respective Navier-Stokes equations (BIRD; STEWART; LIGHTFOOT, 2007):

$$\frac{\partial}{\partial x}(\rho v_x v_x) + \frac{\partial}{\partial y}(\rho v_y v_x) = -\frac{\partial P}{\partial x} - \left(\frac{\partial}{\partial x}\tau_{xx} + \frac{\partial}{\partial y}\tau_{yx}\right) \tag{3.9}$$

$$\frac{\partial}{\partial x}(\rho v_x v_y) + \frac{\partial}{\partial y}(\rho v_y v_y) = -\frac{\partial P}{\partial y} - \left(\frac{\partial}{\partial x}\tau_{xy} + \frac{\partial}{\partial y}\tau_{yy}\right) \tag{3.10}$$

where P is the pressure and τ_{ij} are the components of the stress tensor. Since Newtonian fluid was considered, the corresponding stress tensor components were calculated according to Eqs. 3.11-3.13 (BIRD; STEWART; LIGHTFOOT, 2007):

$$\tau_{xx} = -\mu\left(2\frac{\partial v_x}{\partial x}\right) + \frac{2}{3}\mu\left(\frac{\partial v_x}{\partial x} + \frac{\partial v_y}{\partial y}\right) \tag{3.11}$$

$$\tau_{yy} = -\mu\left(2\frac{\partial v_y}{\partial y}\right) + \frac{2}{3}\mu\left(\frac{\partial v_x}{\partial x} + \frac{\partial v_y}{\partial y}\right) \tag{3.12}$$

$$\tau_{xy} = \tau_{yx} = -\mu\left(\frac{\partial v_y}{\partial x} + \frac{\partial v_x}{\partial y}\right) \tag{3.13}$$

where is the mixture dynamic viscosity. Eqs. 3.9 and 3.10 consist in a parabolic boundary value problem and thus 8 boundary conditions must

be specified to solve the momentum conservation. At the inlet of the channel that defines the geometry used (see Figure 3.1), a given value was imposed for the *x*-component of the velocity (Eq. 3.14), while at the outlet null gauge pressure was prescribed (Eq. 3.15).

Figure 3.1 – Schematic representation of the computational domain. All characteristic dimensions and boundary conditions are indicated.

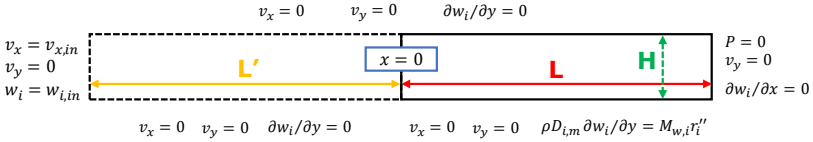

Source: Lira *et al.* (2018)

$$v_x(x = -L', \forall y) = v_{x,in} \tag{3.14}$$

$$P(x = L, \forall y) = 0 \tag{3.15}$$

Moreover, the *x*-component of the velocity was equal to zero at the walls:

$$v_x(\forall x, y = 0) = v_x(\forall x, y = H) = 0 \tag{3.16}$$

In addition, the *y*-component of the velocity was prescribed as zero at all boundaries of the domain:

$$v_y(x = -L', \forall y) = v_y(x = L, \forall y) = v_y(\forall x, y = 0) = \\ = v_y(\forall x, y = H) = 0 \tag{3.17}$$

The conservation of NO, NO_2 and H_2O was calculated by Eq. 3.18 (BIRD; STEWART; LIGHTFOOT, 2007):

$$\frac{\partial}{\partial x}(\rho v_x \omega_i) + \frac{\partial}{\partial y}(\rho v_y \omega_i) + \frac{\partial}{\partial x}(J_{i,x}) + \frac{\partial}{\partial y}(J_{i,y}) = 0 \tag{3.18}$$

where ω_i is the species mass fraction and $J_{i,(x,y)}$ represent the diffusive flux of the species *i* in the *x* and *y* coordinates, given by Fick's law (assuming dilute concentration, *i.e.*, large excess of air) (Eqs. 3.19 and 3.20) (BIRD; STEWART; LIGHTFOOT, 2007):

$$J_{i,x} = -\rho D_{i,m} \frac{\partial \omega_i}{\partial x} \tag{3.19}$$

$$J_{i,y} = -\rho D_{i,m} \frac{\partial \omega_i}{\partial y} \tag{3.20}$$

where $D_{i,m}$ is the species diffusivity in the mixture, expressed by Eq. 3.21 (YANG; SIMON; CUI, 2017):

$$D_{i,m} = \frac{1 - y_i}{\sum_{j,j \neq i} \left(y_j / D_{ij} \right)} \tag{3.21}$$

The binary molecular diffusion coefficients D_{ij} were calculated through a modified Chapman-Enskog correlation given by Eq. 3.22 (MCGEE, 1991):

$$D_{ij} = 0.0018583 \times \frac{\left[T^3 \left(\frac{1}{M_{w,i}} + \frac{1}{M_{w,j}} \right) \right]^{\frac{1}{2}}}{P_{abs} \sigma_{ij}^2 \Omega_D} \tag{3.22}$$

where $M_{w,(i,j)}$ is the molecular weight of the species, T is the absolute temperature and P_{abs} is the absolute pressure. In Eq. 3.22, the collision integral (Ω_D) is a function of the dimensionless temperature (BIRD; STEWART; LIGHTFOOT, 2007):

$$T^* = \frac{T}{(\epsilon / k_B)_{ij}} \tag{3.23}$$

$$\Omega_D = \frac{1.06036}{T^{*0.15610}} + \frac{0.19300}{\exp(0.47635 \times T^*)} + \frac{1.03587}{\exp(1.52996 \times T^*)} + \frac{1.76474}{\exp(3.89411 \times T^*)} \tag{3.24}$$

The Lennard-Jones energy parameter $(\epsilon / k_B)_{ij}$ for the mixture was calculated according to the geometric average expressed by Eq. 3.25 (BIRD; STEWART; LIGHTFOOT, 2007):

$$(\epsilon/k_B)_{ij} = \sqrt{(\epsilon/k_B)_i \times (\epsilon/k_B)_j} \tag{3.25}$$

In addition, the Lennard-Jones characteristic length for the mixture σ_{ij} was calculated by the arithmetic average given in Eq. 3.26 (BIRD; STEWART; LIGHTFOOT, 2007):

$$\sigma_{ij} = \frac{1}{2}(\sigma_i + \sigma_j) \tag{3.26}$$

Table 3.1 presents the physical properties considered herein. The dynamic viscosity of the mixture (μ) was calculated according to Eqs. 3.27 and 3.28 (FLUENT, 2011):

Table 3.1 – Physical properties adopted in the CFD simulations.

Species	μ_i^* (kg·m^{-1}·s^{-1})	$M_{w,i}^*$ (kg·kmol^{-1})	σ_i^* (Å)	$(\epsilon/k_B)_i^*$ (K)	D_{ij} (m^2·s^{-1})**		
					NO	NO_2	H_2O^{vap}
Air	1.7894×10^{-5}	28.966	3.711	78.6	1.76×10^{-5}	1.60×10^{-5}	2.25×10^{-5}
NO	1.72×10^{-5}	30.0061	4	100	-	1.42×10^{-5}	1.94×10^{-5}
NO_2	1.72×10^{-5}	46.0055	4	100	-	-	1.81×10^{-5}
H_2O^{vap}	1.34×10^{-5}	18.01534	2.605	572.4	-	-	-

Source: *ANSYS® CFD (Fluent®) database; **Eq. 3.22.

$$\mu = \sum_i \frac{y_i \mu_i}{\sum_j y_i \phi_{ij}} \tag{3.27}$$

$$\phi_{ij} = \frac{\left[1 + \left(\frac{\mu_i}{\mu_j}\right)^{1/2} \left(\frac{M_{w,j}}{M_{w,i}}\right)^{1/4}\right]^2}{\left[8\left(1 + \frac{M_{w,i}}{M_{w,j}}\right)\right]^{1/2}} \tag{3.28}$$

where $\mu_{(i,j)}$ is the dynamic viscosity of each species in the mixture. Moreover, the density of the mixture (ρ) was calculated considering the ideal gas law:

$$\rho = \frac{P_{abs} M_w}{RT} \tag{3.29}$$

where M_w is the mixture molar weight and R is the universal gas constant. Known compositions of NO and H_2O were imposed at the channel inlet:

$$w_i(x = -L', \forall y) = w_{i,in} \tag{3.30}$$

while zero derivative of the species fraction was prescribed at the outlet:

$$\frac{\partial w_i}{\partial x}(x = L, \forall y) = 0 \tag{3.31}$$

Impermeability for all species was considered at the upper wall as well as at the non-reactive portion of the bottom wall:

$$\frac{\partial w_i}{\partial y}(\forall x, y = H) = 0 \tag{3.32}$$

$$\frac{\partial w_i}{\partial y}(-L' < x < 0, y = 0) = 0 \tag{3.33}$$

while at the bottom wall a Neumann condition was imposed, considering continuity of fluxes due to mass transport and chemical reaction:

$$\rho D_{i,m} \frac{\partial w_i}{\partial y}(0 < x < L, y = 0) = M_{w,i} r_i'' \tag{3.34}$$

The chemical reaction was assumed to occur only at the external surface, *i.e.*, pore reaction-diffusion was assumed negligible. The rate of NO and NO_2 reaction was given, respectively, by Eqs. 3.35 and 3.36 (BALLARI *et al.*, 2010):

$$-r_{NO}'' = \frac{\tilde{k}_{NO}'' C_{NO}^s}{1 + \tilde{K}_{NO} C_{NO}^s + \tilde{K}_{NO_2} C_{NO_2}^s + K_{H_2O} C_{H_2O}^g} \times \left(-1 + \sqrt{1 + \alpha E}\right) \tag{3.35}$$

$$-r_{NO_2}'' = \frac{\tilde{k}_{NO_2}'' C_{NO_2}^s - \tilde{k}_{NO}'' C_{NO}^s}{1 + \tilde{K}_{NO} C_{NO}^s + \tilde{K}_{NO_2} C_{NO_2}^s + K_{H_2O} C_{H_2O}^g} \times \left(-1 + \sqrt{1 + \alpha E}\right) \tag{3.36}$$

where $\tilde{k}_i''$ and $\tilde{K}_i$ are intrinsic (i.e., without contributions of mass transfer limitations) kinetics and equilibrium parameters, respectively. A comprehensive discussion about the corrections of the parameters of Eqs. 3.35 and 3.36, based on the values reported by Ballari *et al.* (2010),

presented in Table 3.2 and taken as reference in this study, was included in the Appendix A. It should be highlighted that the light intensity (E) was explicitly considered in these rate laws.

Table 3.2 – Parameters of the rate laws.

Parameter	Value	Unit
k''_{NO}	4.18	$m \cdot s^{-1}$
k''_{NO_2}	6.73×10^{1}	$m \cdot s^{-1}$
K_{NO}	$8.48 \times 10^{+8}$	$m^3 \cdot kmol^{-1}$
K_{NO_2}	$3.02 \times 10^{+8}$	$m^3 \cdot kmol^{-1}$
K_{H_2O}	$5.07 \times 10^{+4}$	$m^3 \cdot kmol^{-1}$
α	2.37×10^{-3}	$m^2 \cdot W^{-1}$

Source: Ballari *et al.* (2010)

3.2.2 Computational procedure

The mathematical model presented in section 3.2.1 was solved with ANSYS® CFD (Fluent®), version 14.0, using the finite volume method. A 2D domain with length of 0.4 m and height (H) of 3 mm was used, according to the experimental setup taken as reference (see Figure 3.1). It should be highlighted that the domain with length L ($0 < x < 0.2$ m) representing the real dimension of the photoreactor was extended by L' (-0.2 m $< x < 0$) to ensure fully developed laminar velocity profile at the entrance of the device (i.e., $x = 0$ at the beginning of the photoreactor domain).

All boundary conditions described in section 3.2.1 are also indicated at the corresponding locations in Figure 3.1. Room temperature (293 K) was imposed at all boundaries. A homogeneous velocity ($v_{x,in}$=0.1667 $m \cdot s^{-1}$) was specified at the inlet. NO and H_2O composition at the inlet were imposed as molar fraction considering a reference concentration of 4.47×10^{-8} $kmol \cdot m^{-3}$ for NO and different values of relative humidity varying in the range (10-60)%. These values of RH were translated to molar fraction of H_2O at the inlet through psychometric conversions. Based on the given RH (50%) and temperature of reference (293 K), the absolute humidity (AU) and specific volume ($\hat{V}$) were found. The density and molar concentration of dry air were calculated according to Eqs. 3.37 and 3.38, respectively.

$$\rho_{air} = 1/\hat{V} \tag{3.37}$$

$$C_{air} = \rho_{air}/M_{w,air} \tag{3.38}$$

The specific volume, density and molar concentration of water were then respectively calculated by Eqs. 3.39-3.41.

$$\hat{V}^* = \hat{V}/AU \tag{3.39}$$

$$\rho_{H_2O} = 1/\hat{V}^* \tag{3.40}$$

$$C_{H_2O} = \rho_{H_2O}/M_{w,H_2O} \tag{3.41}$$

Furthermore, the total molar concentration was given by Eq. 3.42:

$$C_T = \sum_{i=1}^{n} C_i \tag{3.42}$$

where n is the number of species in the mixture. Finally, the molar fraction of NO and H_2O at the inlet was calculated as the ratio of the species molar concentration and the total concentration:

$$y_i = C_i/C_T \tag{3.43}$$

The molar fraction of NO_2 was equal to zero at the inlet in all simulations. Also, the molar fraction of air was calculated by the restriction $\Sigma y_i = 1$.

A homogeneous irradiance (E) of 10 $W \cdot m^{-2}$ was imposed at the reactive wall ($0 < x < L$) as a reference condition. However, this value was further varied in the range of (0.3-13) $W \cdot m^{-2}$. Furthermore, the NO concentration at the inlet was varied, assuming the following values: 4.5×10^{-9} $kmol \cdot m^{-3}$, 1.45×10^{-8} $kmol \cdot m^{-3}$, 2.25×10^{-8} $kmol \cdot m^{-3}$ and 4.47×10^{-8} $kmol \cdot m^{-3}$ (BALLARI *et al.*, 2010).

Since the kinetics of NO and NO_2 chemical reaction follows LHHW rate laws (Eqs. 3.35 and 3.36) a user defined function (UDF) was written (C code) for the calculation of the boundary condition expressed in Eq. 3.34 (see Figure A.2 in Appendix A).

The macro DEFINE_SR_RATE was used in this code. Thus, the rate laws must be written to yield units of $kmol \cdot m^{-2} \cdot s^{-1}$. The C code was then compiled into ANSYS® CFD (Fluent®).

The 2D steady double precision solver (2ddp) was used in all cases. SIMPLE scheme was applied for the pressure-velocity coupling. Spatial discretization was performed through least squares cell-based scheme for

the gradients, standard for the pressure and second order upwind for the remaining variables.

All cases were initialized prescribing the values of the variables at the inlet in the entire domain. The solution was considered converged when the scaled residuals for the overall mass, (*x*,*y*)-velocity components, energy and species equations were lower than 10^{-4}, 10^{-4}, 10^{-6} and 10^{-12}, respectively. It should be highlighted that although this problem is essentially isothermal, the energy equation should be enabled for the calculation of the mixture density as an ideal gas. The entire computational domain was discretized with quadrilateral elements and a mesh independence study was carried out prior to collecting the final data. For the reference case, considering the photoreactor with length *L* and height *H*, the final mesh was composed by $\sim 3.2\times10^4$ quadrilateral elements. Complementary studies were carried out considering channels with height *2H* and *4H* (keeping *L* and *L'* constant), resulting in meshes with $\sim 6.2\times10^4$ and $\sim 1.2\times10^5$ elements, respectively.

Finally, the molar concentrations of NO and NO_2 were calculated as mass-weighted averages:

$$C_{(NO,\,NO_2)}^{avg,out} = \frac{\int C_{(NO,\,NO_2)}\rho|\vec{v}\cdot d\vec{A}|}{\int \rho|\vec{v}\cdot d\vec{A}|} = \frac{\sum_{i=1}^{n} C_{(NO,\,NO_2)_i}\rho_i|\vec{v}_i\cdot\vec{A}_i|}{\sum_{i=1}^{n}\rho_i|\vec{v}_i\cdot\vec{A}_i|} \tag{3.44}$$

where $C_{(NO,NO_2)_i}$, ρ_i, $\vec{v}_i$ and $|\vec{A}_i|$ are the molar concentration of NO and NO_2, density, velocity and area in each element, at the outlet of the computational domain ($x = L$), for comparison with the experimental data taken as reference for the validation of the model.

3.3 RESULTS AND DISCUSSION

The numerical solution of the mathematical model described in section 3.2.1, considering the procedure presented in section 3.2.2, allowed the validation of the CFD model with experimental data taken from the literature (BALLARI *et al.*, 2010).

Figure 3.2 presents a comparison of the results obtained numerically and the experimental data regarding the NO conversion (X_{NO}) and selectivity (*S*), calculated by Eqs. 3.45 and 3.46 (ÂNGELO *et al.*, 2013), at the reactor outlet as a function of relative humidity.

$$X_{NO}(\%) = \left(\frac{C_{NO}^{in} - C_{NO}^{avg,out}}{C_{NO}^{in}}\right) \times 100 \quad (3.45)$$

$$S(\%) = \left(1 - \frac{C_{NO_2}^{avg,out}}{C_{NO}^{in} - C_{NO}^{avg,out}}\right) \times 100 \quad (3.46)$$

Figure 3.2 – NO conversion (X_{NO}) and selectivity (S) as a function of the relative humidity ($v_{x,in}$ = 0.1667 m·s^{-1}; E = 10 W·m^{-2}). Comparison between the experimental profiles (BALLARI *et al.*, 2010) and those obtained by the CFD simulations.

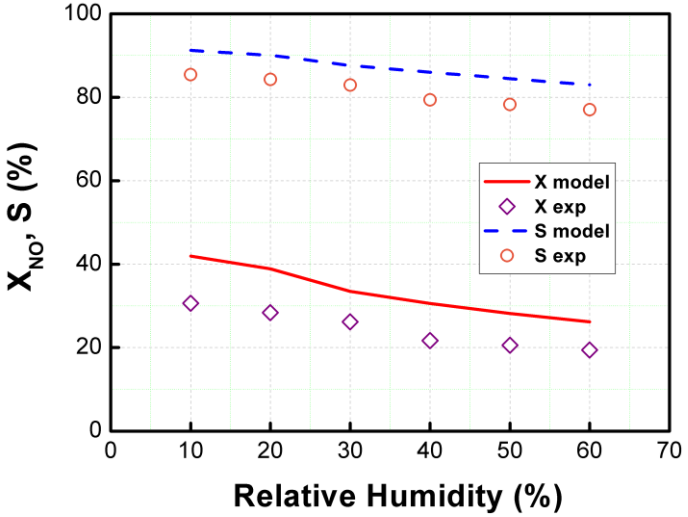

Source: Lira *et al.* (2018)

Clearly, as the relative humidity was increased there was a tendency of decreasing the NO conversion at the reactor outlet. Similarly, the selectivity decreased as the relative humidity increased. Maggos *et al.* (2007b) concluded that the relative humidity effect on the conversion of pollutants is also influenced by their concentration. If pollutants concentration is at ppb level, the competition for adsorption sites is much higher than if they are at ppm concentrations. This happens because for feed concentrations at ppb level it is needed only a small amount of water to produce enough hydroxyl/superoxide radicals. The difference of the molar ratio of NO_x/H_2O between the reactor inlet and outlet decreases

nonlinearly as the relative humidity is increased (see Figure A.3 in Appendix A) in the reactor studied herein.

Evidently, a gap was obtained when comparing the data from the CFD simulations and the experimental results for NO conversion and selectivity. However, the same trend obtained in the experiments was observed when solving the mathematical model.

Moreover, the NO conversion and selectivity increased for the highest values of irradiance. Figure 3.3 presents a comparison of the NO conversion and selectivity as a function of the light intensity, keeping the inlet velocity and the relative humidity constant (0.1667 $m \cdot s^{-1}$ and 50%, respectively), and an excellent agreement between the experimental and numerical data was obtained.

Figure 3.3 – NO conversion (X_{NO}) and selectivity (S) as a function of the irradiation intensity ($v_{x,in}$ = 0.1667 $m \cdot s^{-1}$; RH = 50%). Comparison between the experimental profiles (BALLARI *et al.*, 2010) and those obtained by the CFD simulations.

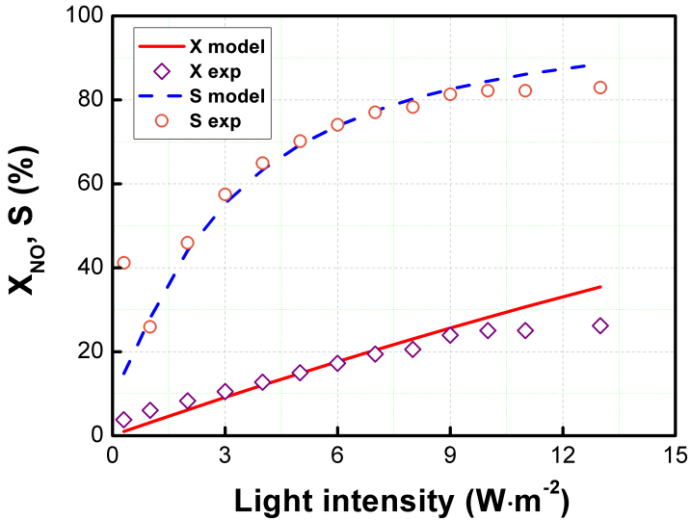

Source: Lira *et al.* (2018)

A Taylor series expansion of the term $\sqrt{1 + \alpha E}$ in Eqs. 3.35 and 3.36 around $E = 0$ results in $(1 + 0.5 \times \alpha \times E)$, while for large E it results in $\sqrt{\alpha \times E}$. Thus, the linearity of $X = X(E)$ observed in Figure 3.3 is consistent considering the range of E considered herein and the value

of the parameter (=2.37×10^{-3} m^2·W^{-1}). A scenario considering a higher value for the parameter α is presented in the Appendix A (see Figure A.4).

Keeping the inlet velocity, the relative humidity and the irradiance constant (0.1667 m·s^{-1}, 50% and 10 W·m^{-2}, respectively), an excellent agreement was observed when comparing the NO conversion and selectivity with the values obtained from the CFD simulations for different NO concentrations at the inlet (Figure 3.4). Highest X_{NO} and S were obtained for low concentrations of NO at the inlet.

Figure 3.4 – NO conversion (X_{NO}) and selectivity (S) as a function of the normalized NO concentration at the inlet ($v_{x,in}$ = 0.1667 m·s^{-1}; E = 10 W·m^{-2}; RH = 50%). Comparison between the experimental profiles (BALLARI *et al.*, 2010) and those obtained by the CFD simulations.

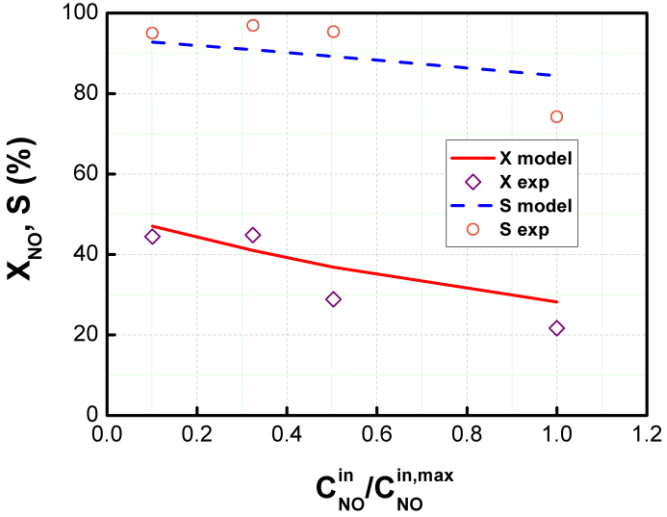

Source: Lira *et al.* (2018)

It should be highlighted that the CFD model presented herein has significant advantages when compared with the 1D plug flow model. Although Ballari *et al.* (2010) obtained good agreement when comparing the 1D plug flow model with their experimental data (used as reference herein), the 2D model implemented in this work allows the treatment of the catalytic reaction as a real surface phenomenon, unlike the plug flow approach. As described in section 3.2.1, the chemical reactions represented by Eqs. 3.35 and 3.36 were prescribed as a boundary condition at the bottom wall of the reactor (Eq. 3.34). Therefore, non-

idealities arising from the reactive flow within the photocatalytic device were properly simulated.

Figure 3.5 – Profiles of (a) NO and (b) NO_2 mass fraction along $0 < y < H$ at x = 0.001, 0.05, 0.10, 0.15 and 0.20 m.

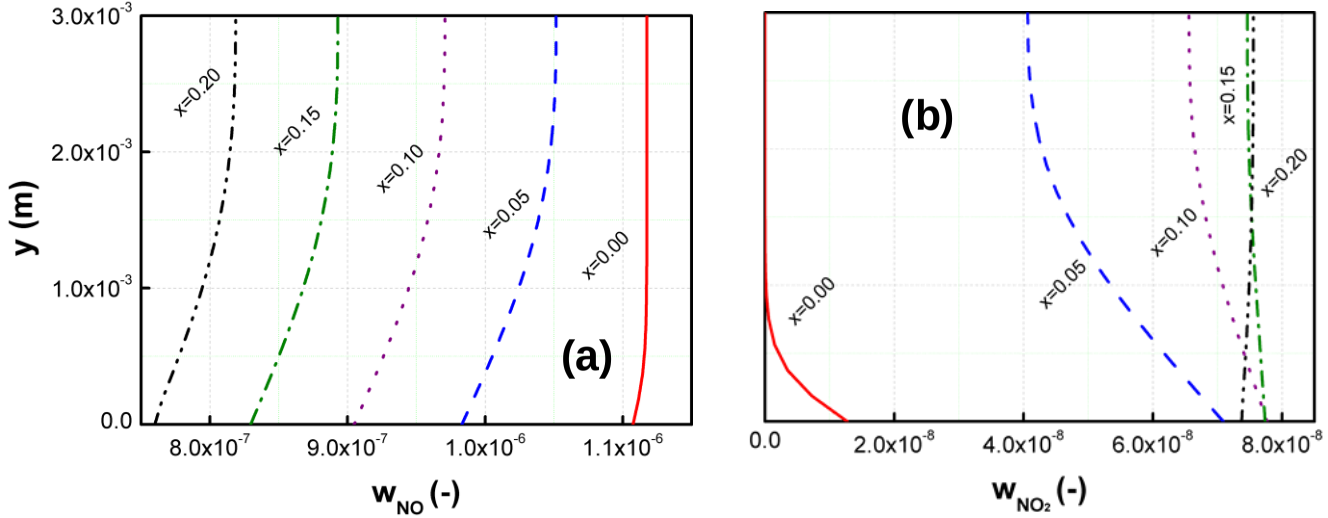

Source: Lira *et al.* (2018)

Clearly, the profiles significantly differ from the plug flow model. Moreover, the complex behavior associated to the NO_2 reactive flow within the device was properly captured in Figure 3.5 (b). Interestingly, the NO_2 mass fraction increases at the region close to the catalytic surface until $x \approx 0.15$ m and then an inversion occurs, due to consumption of this species. On the other hand, Figure 3.6 presents the NO and NO_2 mass fraction profiles obtained for $0 < x < L$ at $y = 0.00$, 0.0015 and 0.003 m.

Figure 3.6 – Profiles of (a) NO and (b) NO_2 mass fractions obtained for $0 < x < L$ at $y = 0.00$, 0.0015 and 0.003 m.

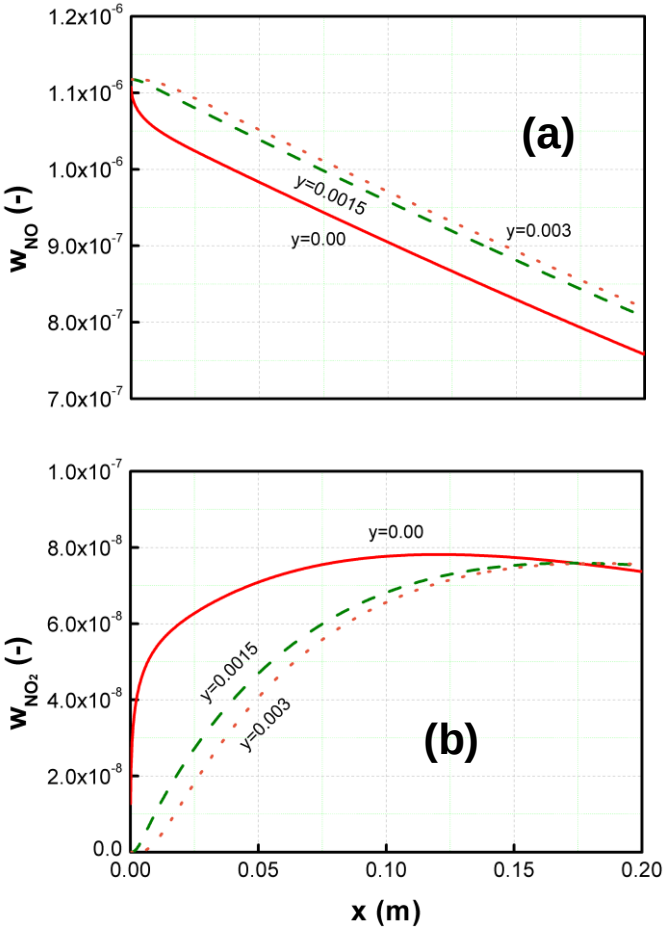

Source: Lira *et al.* (2018)

The NO mass fraction decreased almost linearly for $x > \sim 0.025$ m at y = 0.00, 0.0015 and 0.003 m. However, a significantly different behavior was observed when analyzing the NO_2 mass fraction along the axial coordinates within the photocatalytic reactor. At y = 0.00 the NO_2 mass fraction reaches a point of maximum as expected from the results presented in Figure 3.6(b). Nevertheless, the profiles tend to a saturation at y = 0.0015 and 0.003 m.

This analysis is unfeasible when considering the 1D plug flow model. Thus, the advantage of using a higher dimensional CFD model is evident for the analysis of the reactor performance aiming further optimization regarding different irradiation arranges, for instance. In this study, a homogeneous irradiation at the catalytic surface was assumed, which is acceptable given the conditions adopted in the experiments. However, this is not always the case, especially when macro-scale reactors are considered. In all scenarios, however, CFD codes can be readily used for the design and optimization of photocatalytic reactors given the workflow considered herein coupled with an irradiation distribution model.

Moreover, the 2D CFD model considered in this work allows the comprehensive evaluation of different geometrical features. Figure 3.7 presents the NO and NO_2 molar concentration profiles when the dimension H was varied (H, 2H and 4H), keeping the residence time constant.

It is evident that as H was increased a higher contribution of bulk is noticed. Therefore, an even higher deviation from the plug flow behavior occurs, which implies in enhanced significance of applying the CFD code for the analysis of the reactor.

Additionally, an analysis of the reaction rates ($-r''_{NO}$ and $-r''_{NO_2}$), taken at y = 0.00, for different values of H is presented in Figure 3.8.

Figure 3.7 – NO and NO_2 molar concentration ($mol \cdot m^{-3}$) profiles varying H; (a) C_{NO} for H; (b) C_{NO} for $2H$; (c) C_{NO} for $4H$; (d) C_{NO2} for H; (e) C_{NO2} for $2H$; (f) C_{NO2} for $4H$.

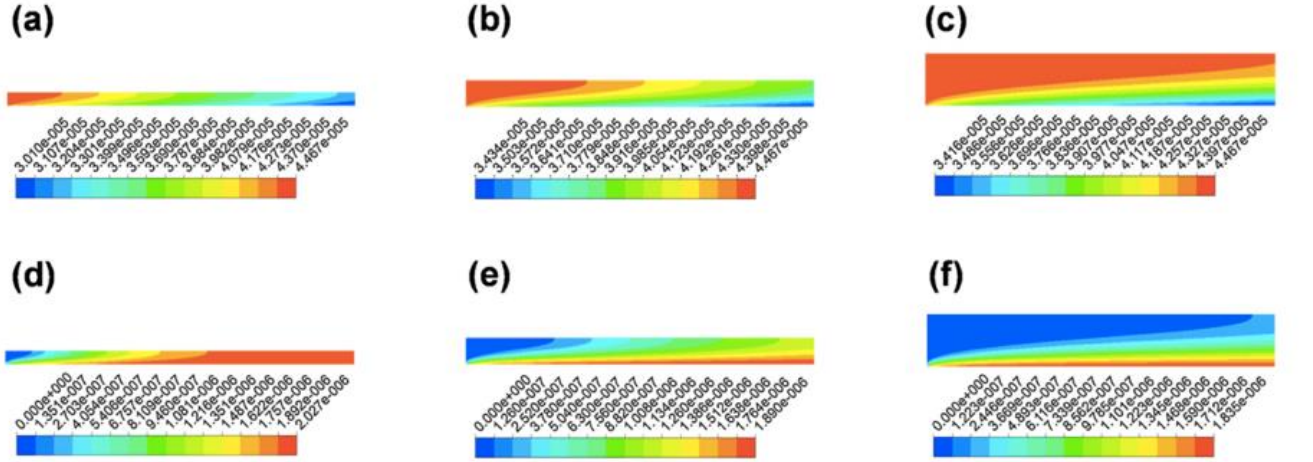

Source: Lira *et al.* (2018)

Figure 3.8 – Reaction rates for (a) NO and (b) NO_2 along x at the catalytic surface.

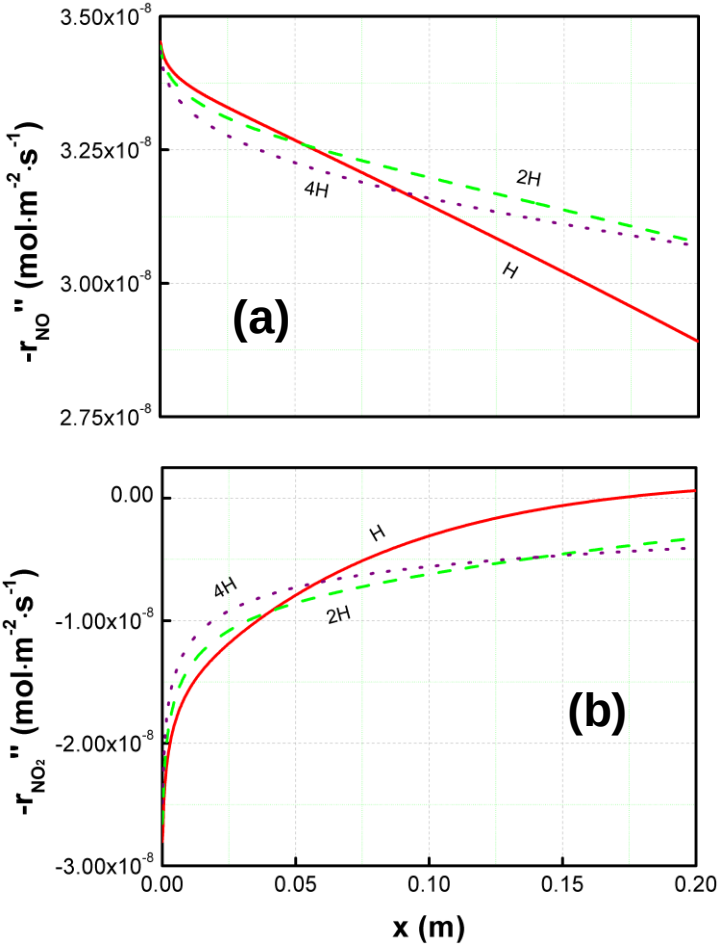

Source: Lira *et al.* (2018)

Figure 3.8(a) shows that a higher NO consumption was observed at the first ~25% and ~50% of the reactor length when considering the height H compared to the configurations with height $2H$ and $4H$, respectively. However, $-r''_{NO}$ continues to decrease almost linearly along x for the height H. When the height $2H$ was considered, the reaction rate was higher than that of the reference after $x > \sim 0.25L$. However, for the system with height $4H$, $-r''_{NO}$ was higher than the reference for $x > \sim 0.5L$, but lower than the reaction rate observed for the height $2H$ along the entire

reactor length. A more complex, but inverse, behavior was noticed for $-r''_{NO_2}$, as depicted in Figure 3.8(b). Furthermore, taking the integral of $-r''_{NO}$ along the catalytic surface reveals the existence of a point of maximum regarding the NO consumption rate for the reactor with height $2H$ (see Figure 3.9). Moreover, Figure 3.9 shows that, while X_{NO} continually decreased, S passed through a point of minimum when the channel height was varied in the range H–$4H$. Thus, it is evident the need for optimization of the reactor performance for the intensification of this photocatalytic process.

Figure 3.9 – Integral rate of NO consumption at the catalytic surface, X_{NO} and S as a function of the height H of the photocatalytic reactor ($v_{x,in}$ = 0.1667 m·s^{-1}; E = 10 W·m^{-2}; RH = 50%). The insert represents the integral rate of NO_2 consumption (nmol$_{NO2}$·s^{-1}) as a function of H.

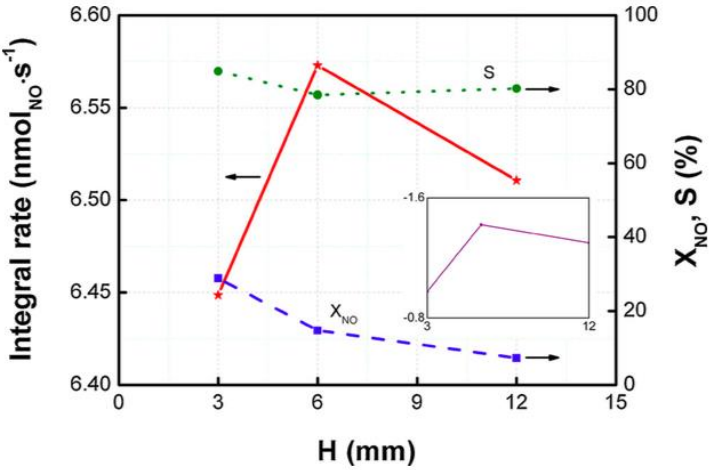

Source: Lira *et al.* (2018)

Finally, a comparison of X_{NO} and S profiles, as a function of the concentration of NO at the inlet and the channel height, considering the CFD and 1D plug flow models, can be observed in Figure A.5 (Appendix A). The plug flow calculation was performed with the explicit fourth-order Runge-Kutta method (algorithm also provided in the Appendix A). Although no significative differences were noted between the calculated values of X_{NO} by CFD and the plug flow approaches, the profiles of S diverged significantly when considering the different models for the channel heights H, $2H$ and $4H$.

In addition, it should be highlighted that the behavior observed in Figure 3.9 is not predicted by the plug flow model. While the integral rate of NO consumption passes through a point of maximum as the channel height is varied in the range H-4H when considering the CFD model, it continuously decreases when the plug flow approach is considered.

It should be noted, however, that the capability of the CFD approach becomes even more evident in cases in which ideal flow conditions cannot be assumed. Once validated, the CFD model can, therefore, be used to test different arranges of the photoreactor, at different scales and considering possible complex geometric features.

3.4 CONCLUSION

A 2D CFD model was implemented and validated with experimental data available in the literature for NOx abatement in a photocatalytic reactor, considering rate laws assigned as boundary condition at the catalytic surface and evaluating the effect of varying relative humidity, irradiation intensity and NO concentration at the inlet on the performance of the system. The CFD model allowed the simulation of the reactive flow inside the photocatalytic device as a real heterogeneous process and, therefore, a significant advantage regarding the ideal 1D plug flow model was obtained. Composition profiles along the reactor axial and transversal dimensions revealed a significant deviation from the plug flow model, evidencing the relevance of the model implemented herein for design, analysis, optimization and scale-up (or scale-out) of photocatalytic reactors applied to NOx abatement. An investigation of the effect of varying the reactor height (H), keeping all other conditions constant, was carried out and revealed a nonlinear behavior regarding the reaction rates calculated along the catalytic surface. A point of maximum for the integral rate of NO consumption as a function of H was also found. It should be highlighted that the CFD model implemented herein can be readily used for the investigation of the performance of photocatalytic reactors with in homogeneous irradiation, different light source arranges, etc. Moreover, as previously mentioned, different geometrical configurations can be investigated, with any level of complexity, allowing fast and effective preliminary evaluation of several scenarios aiming mainly the intensification of the photocatalytic process under technical and economic feasibility limits.

4 CFD SIMULATION OF A FLAT PLATE PHOTOCATALYTIC REACTOR APPLIED TO NOx REMOVAL: COMPARING 2D AND 3D APPROACHES

4.1 INTRODUCTION

Air pollution has become a concern in recent years with high air pollution rates in many cities around the world. The World Health Organization (2016a) highlights that environmental pollution has been considered a global health priority that affects all continents, all socioeconomic groups and most people with varied ages, causing numerous premature deaths each year. In addition to affecting human health, increasing levels of pollutants in the air causes damage to the ecosystem and causes climate changes (HEALTH EFFECTS INSTITUTE, 2018). The major challenge facing this impasse is to find solutions to urban environmental problems: reducing emissions and applying treatment for gaseous pollutants removal using environmentally sustainable technologies.

Several technologies have emerged for the air treatment. Among them, heterogeneous photocatalytic processes have been attracting numerous scientific investments because they deal with the destruction of gaseous pollutants, forming less harmful compounds to the environment (NAKAHARA *et al.*, 2017). This processes, using a semiconductor such as TiO_2 in combination with light exposure (solar or artificial), proved to be highly effective for the abatement of gaseous pollutants (PAZ, 2010; TSANG *et al*., 2019; VERBRUGGEN, 2015). In general, it is well known that light irradiation on the semiconductor induces the formation of electron-hole pairs, which react with chemical species such as H_2O and O_2 and produce hydroxyl radicals (•OH) as well as superoxide radical anions ($O_2^{\bullet-}$) which contribute to the decomposition of organic and inorganic compounds on the surface of the catalyst (BOYJOO *et al.*, 2017; NAKATA; FUJISHIMA, 2012; OCHIAI; FUJISHIMA, 2012). This technology represents the newest generation of air purification technology (ZHONG; HAGHIGHAT, 2015).

Heterogeneous photocatalysis has been reported in scientific works as a purely experimental approach. Traditional experimental techniques provide an overview of the process and do not allow for local analysis inside the photoreactor. Thus, mathematical models based on computational fluid dynamics (CFD) are being developed for application in the photo-abatement of atmospheric pollutants, allowing a more rigorous and detailed analysis of the photocatalytic process. Several

studies have been conducted on the CFD application for the photocatalytic abatement of different gaseous pollutants types, such as volatile organic compounds (VOCs) (NAKAHARA *et al.*, 2017; VAN WALSEM *et al.*, 2016; VERBRUGGEN; LENAERTS; DENYS, 2015), and also inorganic compounds such as NOx and SOx (BALLARI *et al.*, 2010; EGEDY *et al.*, 2018; GANDOLFO *et al.*, 2015; GAUVIN *et al.*, 2018). Thus, CFD has been shown to be a powerful tool to model hydrodynamics, radiation transport and chemical reaction in photocatalytic reactors (BOYJOO; ANG; PAREEK, 2013; WANG *et al.*, 2012), allowing to predict the behavior of the reactor, to improve its performance, to save time and even process costs.

Additionally, other efforts have been developed in the modeling of different photocatalytic reactors for air purification purposes according to a recent review by Boyjoo *et al.* (2017). Among the many types of reactors reported by these authors, the flat plate reactor has the simplest configuration. The catalyst is coated on a certain flat substrate, and light with appropriate intensity and wavelength is applied on it. The air contaminants contact with the catalyst when the air passes through the reactor's channel performing the photocatalysis reaction (ZHONG; HAGHIGHAT, 2015). Therefore, CFD simulations of flat plate reactors have been developed for the investigation of gaseous pollutants abatement.

Verbruggen, Lenaerts and Denys (2015) modeled a slit-shaped flat bed photocatalytic reactor for the acetaldehyde oxidation considering two methods: a mass-transfer analytical model adapted from the literature and a 3D CFD approach. The authors observed that the CFD method could accurately calculate the spatial variation of the fluid flow, reaction rate and surface concentrations, which is not explained by the analytical approach. Moreover, the CFD approach proved to be adequate for the design of alternative reactor geometries. Similarly, Wang, Tan and Yu (2014) developed a 3D CFD model that coupled fluid flow and surface photocatalytic reaction for ozone photocatalytic decomposition. This work showed the occurrence of lower ozone concentrations at the edges of the plate near the side walls of the reactor as a result of the longer residence time of the fluid traveling near the walls. Muñoz *et al.* (2019) modeled the photocatalytic oxidation of nitrogen oxides through 3D CFD simulations. The CFD model of the reactor considered the coupling the fluid flow, radiation field, photoreaction and mass transfer, and it was able to predict satisfactorily the experimental results in the reactor with an error below 17%.

Jarandehei and Visscher (2009) developed a 3D CFD model of a flat plate photocatalytic reactor with serpentine geometry for the oxidation of trichloroethylene. The authors obtained detailed information about the reactor that could not be reached from experiments such as an accurate insight of the behavior of the fluid flow and the existence of concentration gradients in the vertical direction of the device even at high gas flows. Moreover, Salvadó-Estivill, Hargreaves and Li Puma (2007) also studied the oxidation of trichloroethylene modeling a flat plate photocatalytic reactor with three-dimensional geometry. The model considered the fluid flow, non-uniform radiation incidence on the catalytic plate and the effect of the reactant concentration. The same research group later developed the 2D model for that process, and they concluded that this simplified model could very well the predictions from the 3D model, which greatly simplified the implementation and computation cost (SALVADÓ-ESTIVILL; BRUCATO; LI PUMA, 2007). Additionally, Zhang, Stefanakos and Goswami (2013) performed a 2D analysis of the airflow through the rectangular duct with different transverse roughness. A significant improvement in the reactor's performance was observed introducing on the surface of the catalyst compared to an equivalent equipment with a smooth surface.

3D CFD simulations provide a more accurate prediction of the fluid flow behavior, and edge effects can be observed near the walls of the reactor; however, this approach requires a greater computational effort. On the other hand, 2D CFD simulations are considered simpler compared to 3D models, but they may be less accurate or even lose some important information about the phenomena that occur inside the reactor. Thus, this leads us to some doubts: faced with greater computational effort, is it worth developing a 3D model for the flat plate photocatalytic reactor under study or does the 2D model already predict the behavior of the same reactor? What differences can be observed between the 2D and 3D models for the flat plate photocatalytic reactor?

In this sense, this work, continuing previous studies of our research group (LIRA *et al.*, 2018), aims to investigate a 3D CFD model for a flat plate photocatalytic reactor applied to the abatement of gaseous pollutant. The proposed model was compared with the 2D model developed by Lira *et al.* (2018) and also with experimental data provided by Ballari *et al.* (2010). An evaluation of reactor's behavior was performed mainly to observe edge effects associated with the fluid travelling near the side walls of the device. Nitrogen oxides (NOx), composed of NO and NO_2, were used as a model pollutant because they cause serious environmental

concern due to acid rain, global warming and human diseases, mainly in the respiratory system.

4.2 METHOD

4.2.1 Mathematical model

The mathematical model consisted of a set of partial differential equations. The system was described as isothermal single-phase flow with multicomponent species transport in steady state. The overall mass and momentum conservation were described by Eqs. 4.1 and 4.2, respectively (*i.e.*, continuity and Navier-Stokes equations; see Table B.1 in Appendix B for more details) (BIRD; STEWART; LIGHTFOOT, 2007).

$$\nabla \cdot (\rho \vec{v}) = 0 \tag{4.1}$$

$$\nabla \cdot (\rho \vec{v}\vec{v}) = -\nabla P - \nabla \cdot \vec{\tau} \tag{4.2}$$

where ρ is the mixture density, $\vec{v}$ is the velocity vector, P is pressure and $\vec{\tau}$ is the stress tensor. Since Newtonian fluid was considered, the stress tensor was calculated by Eq. 4.3 (BIRD; STEWART; LIGHTFOOT, 2007).

$$\vec{\tau} = -\mu(\nabla v + (\nabla v)^{\dagger}) + \frac{2}{3}\mu(\nabla \cdot \vec{v})\delta \tag{4.3}$$

where δ is the unit tensor (with components δ_{ij}), ∇v is the velocity gradient with components $\left(\partial v_j / \partial x_i\right)$, $(\nabla v)^{\dagger}$ is the transpose of the velocity gradient with components $\left(\partial v_i / \partial x_j\right)$ and $(\nabla \cdot \vec{v})$ is the divergence of the velocity vector.

To solve the momentum conservation equations, 18 boundary conditions must be specified (see Figure 4.1). The *x*-component of the velocity at the reactor's inlet was specified (Eq. 4.4), while null gauge pressure was defined at the outlet (Eq. 4.5).

$$v_x(x = -L', \forall y, \forall z) = v_{x,in} \tag{4.4}$$

$$P(x = L, \forall y, \forall z) = 0 \tag{4.5}$$

Figure 4.1 – Representative 3D diagram of the reactor.

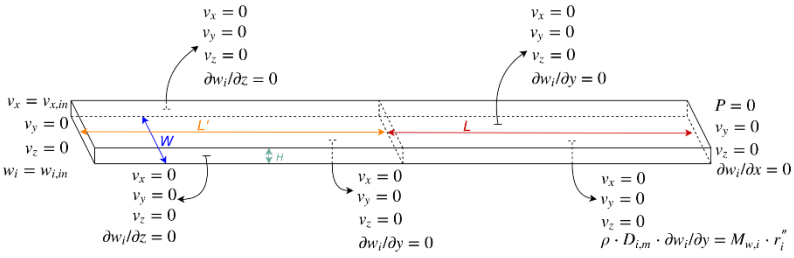

Moreover, the *x*-component of velocity was equal to zero at the walls (Eq. 4.6):

$$\begin{aligned} v_x(\forall x, y = 0, \forall z) &= v_x(\forall x, y = H, \forall z) \\ &= v_x(\forall x, \forall y, z = 0) \\ &= v_x(\forall x, \forall y, z = W) = 0 \end{aligned} \tag{4.6}$$

The (*y*,*z*)-components of the velocity were established as zero at all boundaries of the domain (Eqs. 4.7 and 4.8), respectively:

$$\begin{aligned} v_y(x = -L', \forall y, \forall z) &= v_y(x = L', \forall y, \forall z) \\ &= v_y(\forall x, y = 0, \forall z) \\ &= v_y(\forall x, y = H, \forall z) \\ &= v_y(\forall x, \forall y, z = 0) \\ &= v_y(\forall x, \forall y, z = W) = 0 \end{aligned} \tag{4.7}$$

$$\begin{aligned} v_z(x = -L', \forall y, \forall z) &= v_z(x = L', \forall y, \forall z) \\ &= v_z(\forall x, y = 0, \forall z) \\ &= v_z(\forall x, y = H, \forall z) \\ &= v_z(\forall x, \forall y, z = 0) \\ &= v_z(\forall x, \forall y, z = W) = 0 \end{aligned} \tag{4.8}$$

The conservation of NO, NO_2 and H_2O was calculated by Eq. 4.9 (BIRD; STEWART; LIGHTFOOT, 2007).

$$\nabla \cdot (\rho \vec{v} \omega_i) = -\nabla \cdot \vec{J_i} \tag{4.9}$$

where ω_i is the species mass fraction and $\vec{J_i}$ is the mass flux vector form of Fick's law defined by Eq. 4.10 (assuming dilute concentration, *i.e.*, large excess of air) (BIRD; STEWART; LIGHTFOOT, 2007).

$$\vec{J_i} = -\rho D_{i,m} \nabla \omega_i \tag{4.10}$$

where $D_{i,m}$ is the species diffusivity in the mixture, calculated by Eq. 4.11 (MCGEE, 1991).

$$D_{i,m} = \frac{1}{\sum_{j,j\neq i}\left(\frac{y_j}{D_{ij}}\right)} \tag{4.11}$$

The gas phase binary diffusion coefficient was calculated from a modified Chapman-Enskog correlation given by Eq. 4.12 (MCGEE, 1991).

$$D_{ij} = 0.00188 \times \frac{\left[\mathrm{T}^3\left(\frac{1}{\mathrm{M_{w,i}}} + \frac{1}{\mathrm{M_{w,j}}}\right)\right]^{\frac{1}{2}}}{P_{abs}\sigma_{ij}^2 \Omega_D} \tag{4.12}$$

where $M_{w(i,j)}$ is the molecular weight of the species, T is the absolute temperature, P_{abs} is the absolute pressure, σ_{ij} is the characteristic length, and Ω_D is the collisional integral for diffusion (a function of the dimensionless temperature T^*).

$$T^* = \frac{T}{(\varepsilon/k_B)_{ij}} \tag{4.13}$$

$$\Omega_D = \frac{1.06036}{T^{*0.15610}} + \frac{0.19300}{\exp(0.47635 \times T^*)} + \frac{1.03587}{\exp(1.52996 \times T^*)} + \frac{1.76474}{\exp(3.89411 \times T^*)} \tag{4.14}$$

The Lennard-Jones parameters σ_{ij} and ε_{ij} were estimated according to Eqs. 4.15 and 4.16, respectively (BIRD; STEWART; LIGHTFOOT, 2007).

$$\sigma_{ij} = \frac{1}{2}(\sigma_i + \sigma_j) \tag{4.15}$$

$$(\varepsilon/k_B)_{ij} = \sqrt{(\varepsilon/k_B)_i \times (\varepsilon/k_B)_j} \tag{4.16}$$

Table 4.1 presents the physical properties considered herein. The dynamic viscosity of the mixture was calculated by Eqs. 4.17 and 4.18 (FLUENT, 2011).

Table 4.1 – Physical properties adopted in the CFD simulations.

Species	μ_i^* (kg·m^{-1}·s^{-1})	$M_{w,i}^*$ (kg·kmol^{-1})	σ_i^* (Å)	$(\varepsilon/k_B)_i^*$ (K)	D_{ij} (m^2·s^{-1})**		
					NO	NO_2	H_2O^{vap}
Air	1.7894×10^{-5}	28.966	3.711	78.6	1.76×10^{-6}	1.60×10^{-6}	2.25×10^{-6}
NO	1.72×10^{-5}	30.0061	4	100	-	1.42×10^{-6}	1.94×10^{-6}
NO_2	1.72×10^{-5}	46.0055	4	100	-	-	1.81×10^{-6}
H_2O^{vap}	1.34×10^{-5}	18.01534	2.605	572.4	-	-	-

Source: *ANSYS® CFD (Fluent®) database; **Eq. 4.12.

$$\mu = \sum_i \frac{y_i \mu_i}{\sum_j y_i \phi_{ij}} \tag{4.17}$$

$$\phi_{ij} = \frac{\left[1 + \left(\frac{\mu_i}{\mu_j}\right)^{\frac{1}{2}} \left(\frac{M_{w,j}}{M_{w,i}}\right)^{\frac{1}{4}}\right]^2}{\left[8\left(1 + \frac{M_{w,i}}{M_{w,j}}\right)\right]^{\frac{1}{2}}} \tag{4.18}$$

where $\mu_{(i,j)}$ is the dynamic viscosity of each species in the mixture. In addition, the density of the mixture was calculated considering the ideal gas law, given by Eq. 4.19.

$$\rho = \frac{P_{abs} M_w}{RT} \tag{4.19}$$

where M_w is the mixture molecular weight and R is the universal gas constant. The known composition of NO and H_2O was imposed at the inlet of the reactor (Eq. 4.20).

$$w_i(x = -L', \forall y, \forall z) = w_{i,in} \tag{4.20}$$

Additionally, zero derivative of the species mass fraction was specified at the outlet of the reactor (Eq. 4.21).

$$\frac{\partial w_i}{\partial x}(x = L, \forall y, \forall z) = 0 \tag{4.21}$$

Impermeability of all species was considered at the upper wall, at the non-reactive part of the bottom wall ($-L' < x < 0$) and at the lateral walls (Eqs. 4.22-4.25).

$$\frac{\partial w_i}{\partial y}(\forall x, y = H, \forall z) = 0 \tag{4.22}$$

$$\frac{\partial w_i}{\partial y}(-L' < x < 0, y = 0, \forall z) = 0 \tag{4.23}$$

$$\frac{\partial w_i}{\partial z}(\forall x, \forall y, z = 0) = 0 \tag{4.24}$$

$$\frac{\partial w_i}{\partial z}(\forall x, \forall y, z = W) = 0 \tag{4.25}$$

At the reactive portion at the bottom wall, the Neumann boundary condition was imposed, considering continuity of fluxes due to mass transport and chemical reaction (Eq. 4.26).

$$\rho D_{i,m} \frac{\partial w_i}{\partial y}(0 < x < L, y = 0, \forall z) = M_w r_i'' \tag{4.26}$$

The intrinsic kinetics was assumed to occur only at the external surface of the catalytic material, *i.e.*, reaction and diffusion in the pore was neglected. The rate laws of NO and NO_2 degradation were given by Eqs. 4.27 and 4.28, respectively.

$$(-r_{NO}'')_S = \frac{\widetilde{k_{NO}''} C_{NO}^S}{1 + \widetilde{K}_{NO} C_{NO}^S + \widetilde{K}_{NO_2} C_{NO_2}^S + K_{H_2O} C_{H_2O}} \times \left(-1 + \sqrt{1 + \alpha E}\right) \tag{4.27}$$

$$\left(-r''_{NO_2}\right)_S = \frac{\widetilde{k''_{NO_2}} C^S_{NO_2} - \widetilde{k''_{NO}} C^S_{NO}}{1 + \widetilde{K}_{NO} C^S_{NO} + \widetilde{K}_{NO_2} C^S_{NO_2} + K_{H_2O} C^g_{H_2O}} \times \left(-1 + \sqrt{1 + \alpha E}\right) \tag{4.28}$$

where $\widetilde{k''_i}$ e $\widetilde{K}_i$ are the intrinsic (*i.e.*, without contributions of mass transfer limitations) kinetic and equilibrium parameters, respectively. It should be pointed out that this set of rate laws were based on the work of Ballari *et al.* (2010) and modified by Lira *et al.* (2018) in order to obtain the intrinsic parameters necessary for CFD simulations.

4.2.2 Computational procedure

Species transport and chemical reactions for NOx abatement were modeled with the software ANSYS® CFD (Fluent®), version 14.0, using the finite volume method. The simulations were developed in 3D domain, steady state, laminar flow and including a photocatalytic surface reaction. The geometry was created with length of 0.4 m, height of 3 mm and width of 0.1 m (see Figure 4.1). It should be highlighted that domain with length L ($0 < x < 0.2$ m) represents the real dimensions of the photocatalytic surface. However, the domain with extension L' (-0.2 m $< x < 0$) was created to ensure fully developed laminar velocity profile at the entrance of the reactor ($x = 0$).

All the boundary conditions were shown in section 4.2.1 as well as in Figure 4.1. The inlet velocity was defined as equal to 0.1667 $m \cdot s^{-1}$ at room temperature (293 K). The NO and NO_2 molar fraction were specified assuming a reference concentration of 4.47×10^{-8} $kmol \cdot m^{-3}$ for NO and relative humidity (*RH*) of 50%. This value of *RH* was translated to molar fraction of H_2O at inlet through psychometric conversions. Based on the reference T (293 K) and RH = 50%, the absolute humidity (AU) and specific volume ($\hat{V}$) of dry air were found. The density and molar concentration of dry air were calculated according to Eqs. 4.29 and 4.30, respectively.

$$\rho_{air} = 1/\hat{V} \tag{4.29}$$

$$C_{air} = \rho_{air}/M_{w,air} \tag{4.30}$$

The specific volume, density and molar concentration of water were calculated by Eqs. 4.31 to 4.33.

$$\hat{V}^* = \hat{V}/AU \tag{4.31}$$

$$\rho_{H_2O} = 1/\hat{V}^* \tag{4.32}$$

$$C_{H_2O} = \rho_{H_2O}/M_{w,H_2O} \tag{4.33}$$

Given the concentration of all components, the total concentration was calculated by Eq. 4.34.

$$C_T = \sum_{i=1}^{n} C_i \tag{4.34}$$

where *n* is the number of species in the mixture. Then, the molar fraction of each species was calculated as the ratio of the species molar concentration and the total concentration (Eq. 4.35).

$$y_i = C_i/C_T \tag{4.35}$$

The molar fraction of NO_2 was equal to zero at the entrance in all simulations. Also, the molar fraction of the air was calculated by the restriction $\Sigma y_i = 1$.

A homogeneous irradiation (E) of 10 $W \cdot m^{-2}$ was imposed at the reactive wall ($0 < x < L$) as a reference condition.

The kinetics of the NO and NO_2 decomposition follows a LHHW mechanism (Eqs. 4.27 and 4.28). Thus, a user defined function (UDF) was written (C code) for the calculation of the boundary condition given by Eq. 4.26, as done in a previous work (LIRA *et al.*, 2018).

The macro DEFINE_SR_RATE was used in this code. Therefore, the rate laws must be written to yield units of $kmol \cdot m^{-2} \cdot s^{-1}$. The C code was compiled into ANSYS® CFD (Fluent®).

The 3D steady double precision solver (3ddp) was used in all cases. The SIMPLE scheme was applied for the pressure-velocity coupling. Spatial discretization was performed through least squares cell-based scheme for the gradients, standard for the pressure and second order upwind for the remaining variables.

All cases were initialized with the inlet values. The solution was considered converged when the scaled residuals for the overall mass equation, (*x*,*y*,*z*)-velocity components, energy and species were lower than 10^{-4}, 10^{-4}, 10^{-6} e 10^{-12}, respectively. The entire domain was

discretized with hexahedral elements and the mesh independence study was done before collecting the final data. For the reference case ($C_{NO,in}$ = 4.47×10^{-8} kmol·m^{-3}, RH = 50% and E = 10 W·m^{-2}), the final mesh consisted of ~8×10^{5} hexahedral elements.

Finally, NO and NO_2 molar concentration were calculated as mass-weighted averages, according Eq. 4.36.

$$C_{(NO,NO_2)}^{avg,out} = \frac{\int C_{(NO,NO_2)}\rho\left|\vec{v}\cdot\overrightarrow{dA}\right|}{\int \rho\left|\vec{v}\cdot\overrightarrow{dA}\right|} = \frac{\sum_{i=1}^{n} C_{(NO,NO_2)_i}\rho_i\left|\overrightarrow{v_i}\cdot\overrightarrow{A_i}\right|}{\sum_{i=1}^{n}\rho_i\left|\overrightarrow{v_i}\cdot\overrightarrow{A_i}\right|} \tag{4.36}$$

where $C_{(NO,NO_2)_i}$, ρ_i, $\overrightarrow{v_i}$ e $\left|\overrightarrow{A_i}\right|$ are the molar concentrations of NO and NO_2, density velocity and area in each element, at the outlet of the reactor ($x = L$).

4.3 RESULTS AND DISCUSSION

The results obtained numerically in the 3D domain were evaluated in terms of the conversion of NO (X_{NO}) and selectivity (S), calculated by Eqs. 4.37 and 4.38, at the outlet of the reactor (ÂNGELO *et al.*, 2013).

$$X_{NO}(\%) = \left(\frac{C_{NO}^{in} - C_{NO}^{avg,out}}{C_{NO}^{in}}\right)\times 100 \tag{4.37}$$

$$S(\%) = \left(1 - \frac{C_{NO_2}^{avg,out}}{C_{NO}^{in} - C_{NO}^{avg,out}}\right)\times 100 \tag{4.38}$$

Figure 4.2 shows a comparison of NO conversion and selectivity for the 2D and 3D models by varying the relative humidity, maintaining constant inlet velocity and irradiance intensity (0.1667 m·s^{-1} and 10 W·m^{-2}, respectively). The 2D model was developed in a previous study of our group (LIRA *et al.*, 2018). An excellent agreement was observed when comparing the NO conversion to the values obtained from the 3D CFD simulation with the 2D approach. It is also worth to note that the 2D and 3D models present good agreement with the experimental values, which implies that the data were validated. In addition, 3D simulations were also run for other parameters. In all cases studied, the NO and NO_2

outlet concentration deviation obtained was less than 1% when comparing the 3D and 2D models (see Table B.2 in Appendix B).

Figure 4.2 – NO conversion (X_{NO}) and selectivity (S) as function of relative humidity. Comparison between the 3D model and 2D model (LIRA *et al.*, 2018) with the experimental profiles (BALLARI *et al.*, 2010).

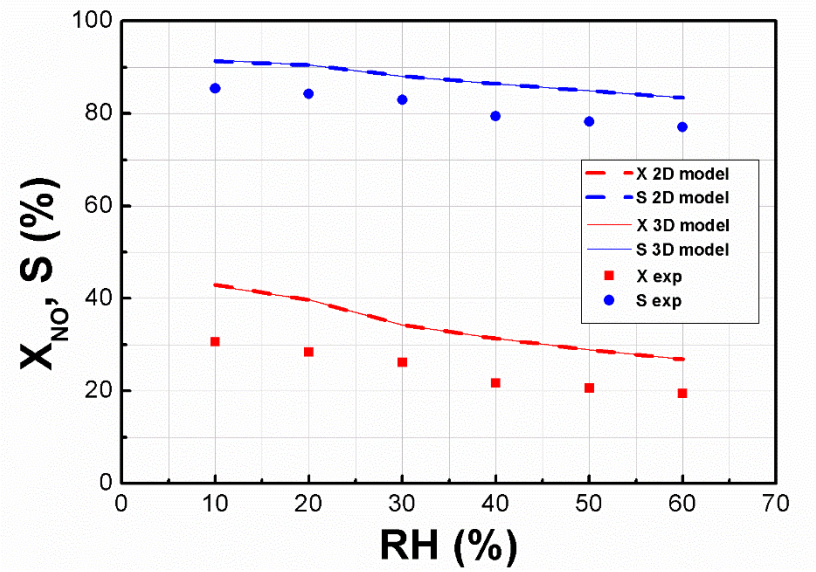

The rate laws represented by Eqs. 4.27 and 4.28 were used as boundary condition (Eq. 4.26) at the bottom wall of the reactor ($0 < x < L$). Figure 4.3 presents the mass fraction profiles for 3D ($W = 0$) and 2D approaches along $0 < y < H$ for x = 0, 0.05, 0.10, 0.15 and 0.20 m. The dashed line represents the 2D solution while the 3D solution is plotted with the solid line. Clearly, the profiles show quite similar behavior for both NO and NO_2. Some differences in the profile were observed due to the associated edge effect near the reactor wall. For both cases, there is a significant deviation from the plug flow model. Especially, the NO_2 profile presented a complex behavior. The mass fraction of NO_2 increases near the surface of the catalyst to x = 0.10, and then the inverse occurs due to the consumption of the species.

Figure 4.3 – Profiles of the mass fraction of (a) NO and (b) NO_2 for 2D and 3D simulations as function of reactor height.

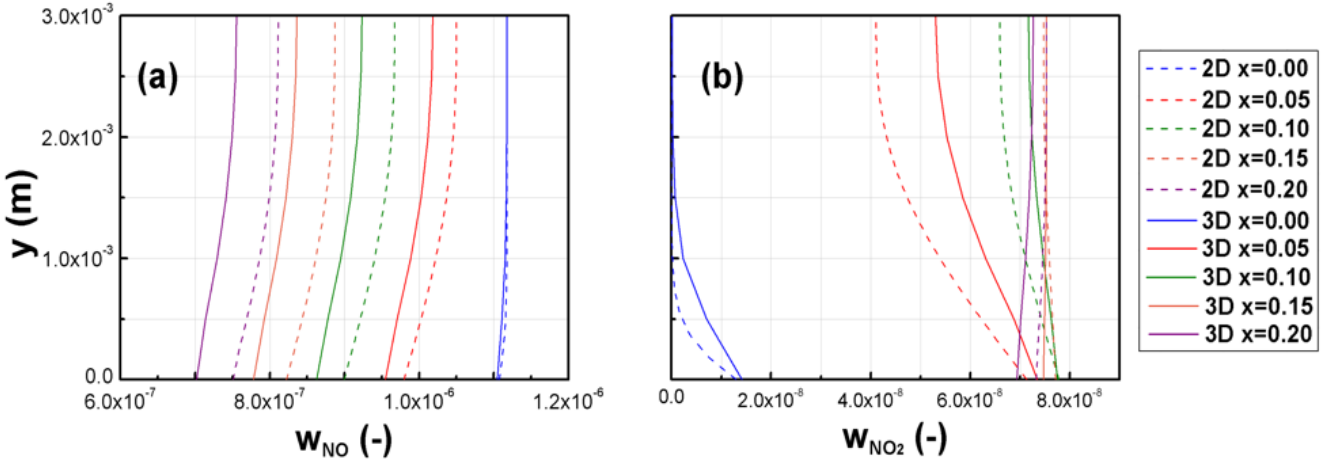

Figure 4.4 shows the mass fraction profiles of NO and NO_2 along the catalytic region ($0 < x < L$) for different reactor heights (y = 0, 0.0015 and 0.003) considering both 2D and 3D models. Again, the profiles along the reactor length were very similar when comparing the models studied and small variations were observed due to the edge effect near the side wall. The NO mass fraction decreases almost linearly. However, different behaviors were observed for the profile along the length of the reactor for NO_2. For y = 0, both the 2D and 3D models presented a point of maximum, as expected in Figure 4.4(b).

Figure 4.4 – Profiles of the mass fraction of (a) NO and (b) NO_2 for 2D and 3D simulations as function of reactor length.

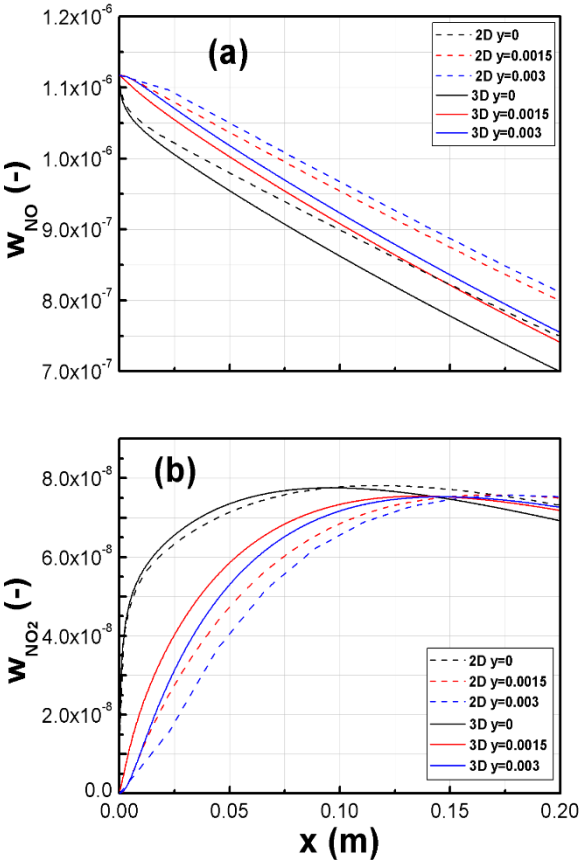

Figure 4.5 presents the mass fraction profile of NO and NO_2 along the width for x = 0, 0.05, 0.10, 0.15 and 0.20 m and y = 0, 0.0015 and 0.003 m. Interestingly, both NO and NO_2 profiles have an edge effect associated with the species flow at the edges of the plate near the side wall (z = 0 and z = W). High variations in the NO and NO_2 concentrations in the x-axis direction can be observed as a result of the reaction and convection of the fluid in the reactor. Lower concentrations at the edge of the reactor width are formed as a result of the higher residence time of the fluid traveling near to the wall.

Figure 4.5 – Profiles of the mass fraction of NO and NO_2 for 3D models as function of reactor width.

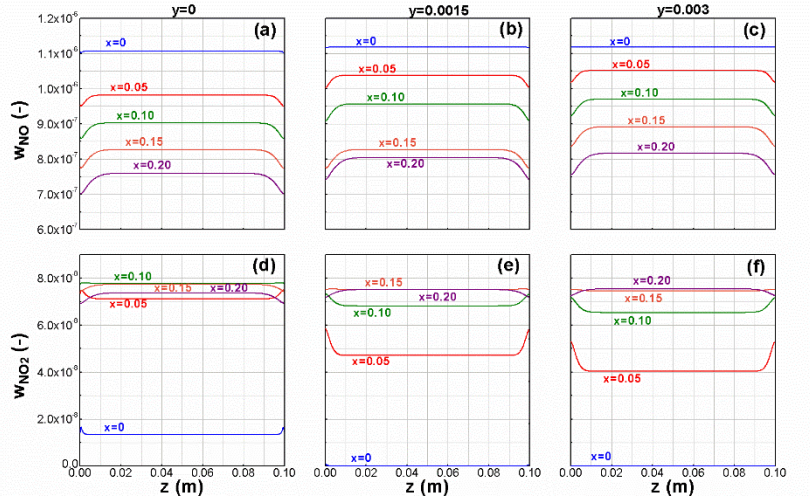

This evidence also can be seen from the NO and NO_2 concentration profiles on the photocatalytic surface (y = 0 m) obtained by the 3D CFD species contours for a standard operation condition (see Figure 4.6). Similar behavior near the side wall was found by other authors for the decomposition of ozone and photocatalytic oxidation of trichloroethylene (SALVADÓ-ESTIVILL; HARGREAVES; LI PUMA, 2007; WANG; TAN; YU, 2014b). This behavior is observed only in 3D CFD simulation, neglected in the 2D model due to the third dimension used. However, this effect did not have great relevance in the quantitative results when compared both simulations.

Figure 4.6 – Contour plot of (a) NO and (b) NO_2 at the photocatalytic surface in the reactor ($C_{NO,in}$ = 4.47×10^{-8} kmol·m^{-3}; E = 10 W·m^{-2} and RH = 50%).

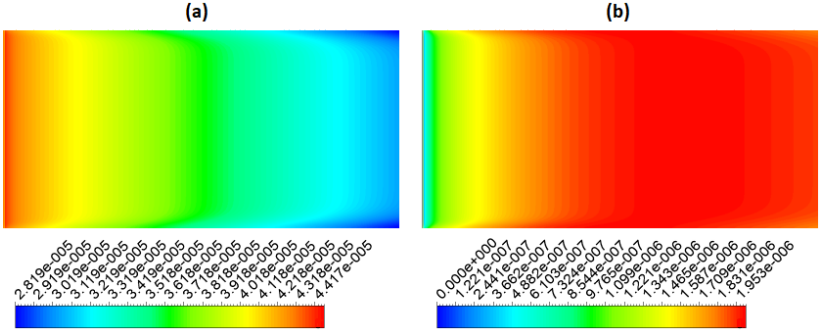

Figure 4.7 shows a comparison of the NO and NO_2 concentration profiles for the 2D and 3D models at W = 0.05 m. It was observed that the contours were very similar with slight changes, but it did not modify the performance of the profiles.

Figure 4.7 – Contour plot of (a) 3D-NO and (b) 3D-NO_2 at W = 0.05 m, (c) 2D-NO and (d) 2D-NO_2 ($C_{NO,in}$ = 4.47×10^{-8} kmol·m^{-3}; E = 10 W·m^{-2} and RH = 50%).

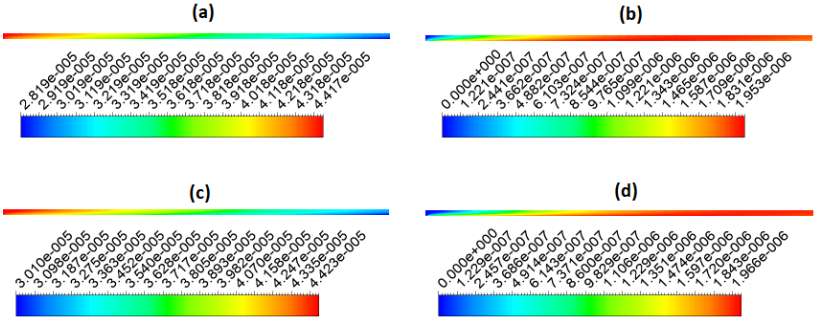

The simplification made in the 2D model assumes that the width is much larger than the height, thus considering an infinite flat plate. Reduction of one dimension of the problem may be enough to answer some questions about the transport of species (NO and NO_2) by the reactor, obviously allowing for faster calculations. Although the 3D model shows interesting effects on the reactor (see Figure 4.5), it requires a higher computational cost. This difference between the time of simulation is very high, using the same machine. For example, in this

case, the 2D CFD simulation time was approximately 20 min to be solved the problem. However, the simulation time for the 3D model took almost 8 h to be solved. As a result, the 2D model obtained results very close to the 3D model with less computational time.

It can be highlighted that all simulations for both 2D and 3D models were performed under the same operating conditions (i.e., the same computer used in all simulations: Intel® Xeon® @ 2.67 GHz, 72 GB CPU of RAM and 64-bit Windows operating system).

4.4 CONCLUSION

A three-dimensional model of a flat plate photocatalytic reactor showed good approximation with experimental results for NOx degradation. It was also shown that the 3D and 2D simulations presented good agreement, showing small variations in the NO and NO_2 concentrations. The 3D model exhibited more detailed information on the flow of the species studied, showing the edge effect near the walls of the reactor. However, this effect did not bring considerable changes in the results presented by both simulations. Due to the complexity, the simulations involving three dimensions require a much longer computational time than those that presuppose some simplifications. In this sense, the 2D model can be used as a good approximation of the flat plate photocatalytic reactor for the degradation of gaseous pollutants.

5 CONCLUDING REMARKS AND RECOMMENDATIONS FOR FUTURE WORK

This work presented a Computational Fluid Dynamics (CFD) approach for the simulation of a flat plate photocatalytic reactor applied to NOx abatement. 2D and 3D models were implemented in the CFD code ANSYS® CFD (Fluent®), version 14.0, considering the coupling of fluid flow, transport of chemical species and surface reaction kinetics. The numerical results were validated with the experimental data provided by Ballari *et al.* (2010).

Among the contributions of this work, it was possible to highlight the implementation and validation of the 2D model. The proposed model was able to adequately describe the behavior of the photocatalytic reactor for NOx degradation. Additionally, the effect of different operational scenarios, namely the relative humidity, light intensity and feed NO concentration, was evaluated. Therefore, it was possible to conclude that these parameters have a strong influence on the NOx removal efficiency. With the increase of the relative humidity from 10% to 60% (maintaining $C_{NO,in}$ = 4.47×10^{-8} kmol·m^{-3} and E = 10 W·m^{-2}), a decrease of approximately 16% in the NOx removal was found. The higher light intensity studied (13 W·m^{-2}) reached a NO conversion of 37% (keeping $C_{NO,in}$ = 4.47×10^{-8} kmol·m^{-3} RH = 50%). Moreover, X_{NO} increased by almost 50% when the initial NO concentration decreased by 10% of the standard condition (4.47×10^{-8} kmol·m^{-3}), maintaining E = 10 W·m^{-2} and RH = 50%.

In addition, the effect of different geometric characteristics, namely the reactor's height, was studied. A nonlinear behavior was revealed in relation to the reaction rates and, also, a point of maximum was reached for the integral rate of NO consumption.

Another contribution consisted in a comparative analysis between the bi-dimensional model and the ideal 1D plug flow approach. Significant advantages of the 2D model were observed in relation to the ideal 1D plug flow model. This model allowed the treatment of the catalytic reaction as a real surface phenomenon. Significant deviations were revealed in relation to the 1D plug flow approach when the NO and NO_2 mass fraction profiles were analyzed.

The three-dimensional model also showed good approximation with the experimental data for the NOx degradation. The 3D model presented more detailed flow information, showing the edge effect near the walls of the reactor. In addition, a comparison between the results of

3D and 2D models was proposed and small variations between the models (less than 1%) were observed. However, the 2D model required a much shorter computational time compared to 3D. Thus, the two-dimensional model can be used as a good approximation of the photocatalytic reactor.

Finally, as suggestions for future work, the following studies can be performed:

- investigation of the performance of the CFD model with the inclusion of the irradiation field, considering the non-uniform irradiation along the reactor.
- evaluation of different light source arrangements.
- elaboration of different geometric configurations of the reactor, highlighting the use of microreactors applied to heterogeneous photocatalytic NOx degradation.
- development of experimental work using other reactor geometries for NOx abatement.

REFERENCES

ÁGUIA, C. *et al.* Influence of photocatalytic paint components on the photoactivity of P25 towards NO abatement. **Polymer Degradation and Stability**, v. 151, p. 77–83, 2010.

ÁGUIA, C. *et al*. Photo-oxidation of NO using an exterior paint - Screening of various commercial titania in powder pressed and paint films. **Journal of Environmental Management**, v. 92, p. 1724–1732, 2011.

ALLEN, N. S. *et al*. Photocatalytic Coatings for Environmental Applications. **Photochemistry and Photobiology**, v. 81, p. 279–290, 2005.

ÂNGELO, J. *et al*. An overview of photocatalysis phenomena applied to NOx abatement. **Journal of Environmental Management**, v. 129, p. 522–539, 2013.

ÂNGELO, J.; ANDRADE, L.; MENDES, A. Highly active photocatalytic paint for NOx abatement under real-outdoor conditions. **Applied Catalysis A: General**, v. 484, p. 17–25, 2014.

BALLARI, M. M. *et al.* Modelling and experimental study of the NOx photocatalytic degradation employing concrete pavement with titanium dioxide. **Catalysis Today**, v. 151, p. 71–76, 2010.

BALLARI, M. M.; YU, Q. L.; BROUWERS, H. J. H. Experimental study of the NO and NO2 degradation by photocatalytically active concrete. **Catalysis Today**, v. 161, p. 175–180, 2011.

BIRD, R. B.; STEWART, W. E.; LIGHTFOOT, E. N. **Transport Phenomena**. 2. ed. John Wíley & Sons, Inc., 2007.

BOYJOO, Y. *et al*. A review on photocatalysis for air treatment: From catalyst development to reactor design. **Chemical Engineering Journal**, v. 310, p. 537–559, 2017.

BOYJOO, Y.; ANG, M.; PAREEK, V. Some aspects of photocatalytic reactor modeling using computational fluid dynamics. **Chemical Engineering Science**, v. 101, p. 764–784, 2013.

BOYJOO, Y.; ANG, M.; PAREEK, V. CFD simulation of a pilot scale slurry photocatalytic reactor and design of multiple-lamp reactors. **Chemical Engineering Science**, v. 111, p. 266–277, 2014.

BRAGA, B. *et al.* **Introdução à engenharia ambiental: O desafio do desenvolvimento sustentável.** 2. ed. São Paulo: Pearson Prentice Hall, 2005.

BYRNE, C.; SUBRAMANIAN, G.; PILLAI, S. C. Recent advances in photocatalysis for environmental applications. **Journal of Environmental Chemical Engineering**, v. 6, p. 3531–3555, 2018.

CAO, X. *et al.* Investigation of Ce-TiO2 photocatalyst and its application in asphalt- based specimens for NO degradation. **Construction and Building Materials**, v. 148, p. 824–832, 2017.

CARP, O.; HUISMAN, C. L.; RELLER, A. Photoinduced reactivity of titanium dioxide. **Progress in Solid State Chemistry**, v. 32, p. 33–177, 2004.

CASSAR, L.; PEPE, C. **Paving tile comprising an hydraulic binder and photocatalyst particles.** Int Cl. C04B 14/30 (2006.01). EP 1600430 B1. 24 jul. 1997. 30 nov. 2005.

CELIK, I. B.; GHIA, U.; ROACHE, P. J.; FREITAS, C. J.; COLEMAN, H.; RAAD, P. E. Procedure for Estimation and Reporting of Uncertainty Due to Discretization in CFD Applications. **Journal of Fluids Engineering**, v. 130, 2008.

CHEN, D. H.; LI, K.; YUAN, R. **Photocatalytic Coating on Road Pavements/structures for NOx Abatement.** In: Annual Project Report Submitted to Houston Advanced Research Center and Office of Air Quality Planning and Standards US Environmental Protection Agency. Houston. Texas, 2007.

CHEN, M.; LIU, Y. NOx removal from vehicle emissions by functionality surface of asphalt road. **Journal of Hazardous Materials**, v. 174, p. 375–379, 2010.

CHONG, S. *et al*. Simulations of Photodegradation of Toluene and Formaldehyde in a Monolith Reactor Using Computational Fluid Dynamics. **AlChE Journal**, v. 57, n. 3, p. 724–734, 2011.

CONAMA. **Resolução no 03 de 28/06/1990 - Controle da Poluição do ar - PRONAR**. Brasil, 1990.

DEVAHASDIN, S. *et al*. TiO2 photocatalytic oxidation of nitric oxide: Transient behavior and reaction kinetics. **Journal of Photochemistry and Photobiology A: Chemistry**, v. 156, p. 161–170, 2003.

DURAN, J. E. **Development of a CFD-Based model for the simulation of immobilized photocatalytic reactors for water treatment**. 2010. 235 f. Thesis (Degree of Doctor of philosophy). University of British Columbia (Vancouver), 2010.

EGEDY, A. *et al*. CFD Based Optimization of a NOx Removal Reactor. **Chemical Engineering Transactions**, v. 70, p. 691–696, 2018.

EUROPEAN ENVIRONMENT AGENCY, E. **Air quality in Europe — 2018 report**. Luxembourg, 2018.

FLUENT, A. **Theory Guide**. ANSYS Inc, 2011.

FOLLI, A. *et al*. TiO2 photocatalysis in cementitious systems: Insights into self-cleaning and depollution chemistry. **Cement and Concrete Research**, v. 42, p. 539–548, 2012.

FUJISHIMA, A.; HONDA, K. Electrochemical Photolysis of water at a Semiconductor Electrode. **Nature**, v. 238, p. 37–38, 1972.

FUJISHIMA, A.; RAO, T. N.; TRYK, D. A. Titanium dioxide photocatalysis. **Journal of Photochemistry and Photobiology C: Photochemistry Reviews**, v. 1, p. 1–21, 2000.

FUJISHIMA, A.; ZHANG, X. Titanium dioxide photocatalysis: present situation and future approaches. **Comptes Rendus Chimie**, v. 9, p. 750–760, 2006.

GALLUS, M. *et al.* Photocatalytic de-pollution in the Leopold II tunnel in Brussels: NOx abatement results. **Building and Environment**, v. 84, p. 125–133, 2015.

GANDOLFO, A. *et al.* The effectiveness of indoor photocatalytic paints on NOx and HONO levels. **Applied Catalysis B: Environmental**, v. 166–167, p. 84–90, 2015.

GAUVIN, F. *et al*. Effect of the morphology and pore structure of porous building materials on photocatalytic oxidation of air pollutants. **Applied Catalysis B: Environmental**, v. 227, p. 123–131, 2018.

HASSAN, M. *et al.* Sustainable Photocatalytic Asphalt Pavements for Mitigation of Nitrogen Oxide and Sulfur Dioxide Vehicle Emissions. **Journal of Materials in Civil Engineering**, v. 25, n. 3, p. 365–371, 2013.

HEALTH EFFECTS INSTITUTE. **State of Global Air 2018:** A special **report on global exposure to air pollution and its disease burden**. Boston, MA: Health Effects Institute. 2018. 24 p.

HERNÁNDEZ RODRÍGUEZ, M. J. *et al.* Comparison of supported TiO2 catalysts in the photocatalytic degradation of NOx. **Journal of Molecular Catalysis A: Chemical**, v. 413, p. 56–66, 2016.

HUNGER, M.; HÜSKEN, G.; BROUWERS, H. J. H. Photocatalytic degradation of air pollutants - From modeling to large scale application. **Cement and Concrete Research**, v. 40, p. 313–320, 2010.

HÜSKEN, G.; HUNGER, M.; BROUWERS, H. J. H. Experimental study of photocatalytic concrete products for air purification. **Building and Environment**, v. 44, p. 2463–2474, 2009.

IMOBERDORF, G. E. *et al*. Photocatalytic Degradation of Formaldehyde in Gas Phase on TiO2 Films: A Kinetic Study. **Industrial & Engineering Chemistry Research**, v. 44, p. 6075–6085, 2005.

IMOBERDORF, G. E. *et al.* Modeling of a Multiannular Photocatalytic Reactor for Perchloroethylene Degradation in Air. **Romanian Journal of Morphology and Embryology**, v. 52, n. 5, p. 1814–1823, 2006.

IMOBERDORF, G. E. *et al*. Scaling-up from first principles of a photocatalytic reactor for air pollution remediation. **Chemical Engineering Science**, v. 62, p. 793–804, 2007.

JACOBY, W. A. *et al*. Kinetics of the oxidation of trichloroethylene in air via heterogeneous photocatalysis. **Journal of Catalysis**, v. 157, p. 87–96, 1995.

JARANDEHEI, A.; VISSCHER, A. DE. Three-Dimensional CFD Model for a Flat Plate Photocatalytic Reactor : Degradation of TCE in a Serpentine Flow Field. **AlChE Journal**, v. 55, n. 2, p. 312–320, 2009.

JIMENEZ-RELINQUE, E. *et al.* Characteristics and efficiency of photocatalytic cementitious materials: Type of binder, roughness and microstructure. **Cement and Concrete Research**, v. 71, p. 124–131, 2015.

KHODADADIAN, F. *et al*. Design, characterization and model validation of a LED-based photocatalytic reactor for gas phase applications. **Chemical Engineering Journal**, v. 333, p. 456–466, 2018.

KOWSARI, E.; ABDPOUR, S. Investigation performance of rod-like ZnO/CdO composites, synthesized in ionic liquid medium as photocatalytic for degradation of air pollutants (SO2 and NOX). **Optik**, v. 127, p. 11567–11576, 2016.

KOWSARI, E.; ABDPOUR, S. In-situ functionalization of mesoporous hexagonal ZnO synthesized in task specific ionic liquid as a photocatalyst for elimination of SO2, NOx, and CO. **Journal of Solid State Chemistry**, v. 256, p. 141–150, 2017.

KRISHNAN, P. *et al*. Photocatalytic degradation of particulate pollutants and self-cleaning performance of TiO2-containing silicate coating and mortar. **Construction and Building Materials**, v. 44, p. 309–316, 2013.

KUMAR, J.; BANSAL, A. CFD simulations of immobilized-titanium dioxide based annular photocatalytic reactor: Model development and experimental validation. **Indian Journal of Chemical Technology**, v. 22, p. 95–104, 2015.

LASEK, J.; YU, Y. H.; WU, J. C. S. Removal of NOx by photocatalytic processes. **Journal of Photochemistry and Photobiology C: Photochemistry Reviews**, v. 14, p. 29–52, 2013.

LAUFS, S. *et al.* Conversion of nitrogen oxides on commercial photocatalytic dispersion paints. **Atmospheric Environment**, v. 44, p. 2341–2349, 2010.

LI PUMA, G. *et al.* Kinetics rate model of the photocatalytic oxidation of trichloroethylene in air over TiO2thin films. **Separation and Purification Technology**, v. 67, p. 226–232, 2009.

LIM, M. *et al.* Development and potential of new generation photocatalytic systems for air pollution abatement: an overview. **Asia-Pacific Journal of Chemical Engineering**, v. 4, p. 387–402, 2009.

LIM, T. H. *et al.* Photocatalytic decomposition of NO by TiO2 particles. **Journal of Photochemistry and Photobiology A: Chemistry**, v. 134, p. 209–217, 2000.

LIRA, J. D. O. B. *et al.* Photocatalytic NO x abatement : Mathematical modeling , CFD validation and reactor analysis. **Journal of Hazardous Materials**, v. x, n. x, p. xxx–xxx, 2018.

LIU, W. *et al.* Photocatalytic degradation of vehicle exhausts on asphalt

pavement by TiO2/rubber composite structure. **Construction and Building Materials**, v. 81, p. 224–232, 2015.

LOPES, F. V. S. *et al.* Insights into UV-TiO2 photocatalytic degradation of PCE for air decontamination systems. **Chemical Engineering Journal**, v. 204–206, p. 244–257, 2012.

MAGGOS, T. *et al.* Photocatalytic degradation of NOx gases using TiO2-containing paint: A real scale study. **Journal of Hazardous Materials**, v. 146, n. 3, p. 668–673, 2007a.

MAGGOS, T. *et al.* Application of photocatalytic technology for NOx removal. **Applied Physics A: Materials Science and Processing**, v. 89, p. 81–84, 2007b.

MARTINEZ, T. *et al.* Degradation of NO using photocatalytic coatings applied to different substrates. **Building and Environment**, v. 46, p. 1808–1816, 2011.

MCGEE, H. A. **Molecular Engineering**. 1. ed. Michigan: McGraw Hill, 1991.

MELO, J. V. S. DE; TRICHÊS, G. Evaluation of the influence of environmental conditions on the efficiency of photocatalytic coatings in the degradation of nitrogen oxides (NOx). **Building and Environment**, v. 49, p. 117–123, 2012.

MILLS, A. *et al.* Kinetics of the photocatalysed oxidation of NO in the ISO 22197 reactor. **Journal of Photochemistry and Photobiology A: Chemistry**, v. 321, p. 137–142, 2016.

MOHSENI, M.; TAGHIPOUR, F. Experimental and CFD analysis of photocatalytic gas phase vinyl chloride (VC) oxidation. **Chemical Engineering Science**, v. 59, p. 1601–1609, 2004.

MUÑOZ, V. *et al.* Photocatalytic NOx removal: Rigorous kinetic modelling and ISO standard reactor. **Catalysis Today**, v. xx, p. xx–xx, 2019.

MURATA, Y. *et al.* **NOx-cleaning paving block**. Int Cl. B01 J23/00. US 5861205. 24 jan. 1997, 19 jan. 1999.

MURATA, Y.; KAMITANI, K.; TAKEUCHI, K. **Air purifying blocks based on photocatalysis**. In: Japan Interlocking Block Pavement Engineering Association World Congress 2000. Tokyo, Japan, 2000.

NAKAHARA, K. *et al.* Computational fluid dynamics modeling and parameterization of the visible light photocatalytic oxidation process of toluene for indoor building material. **Sustainable Cities and Society**, v. 35, p. 298–308, 2017.

NAKATA, K.; FUJISHIMA, A. TiO2 photocatalysis: Design and applications. **Journal of Photochemistry and Photobiology C: Photochemistry Reviews**, v. 13, p. 169–189, 2012.

OBEE, T. N.; BROWN, R. T. TiO2 Photocatalysis for Indoor Air Applications: Effects of Humidity and Trace Contaminant Levels on the Oxidation Rates of Formaldehyde, Toluene, and 1,3-Butadiene. **Environmental Science and Technology**, v. 29, n. 5, p. 1223–1231, 1995.

OCHIAI, T.; FUJISHIMA, A. Photoelectrochemical properties of TiO2 photocatalyst and its applications for environmental purification. **Journal of Photochemistry and Photobiology C: Photochemistry Reviews**, v. 13, p. 247–262, 2012.

P.R.C. ENVIRONMENT, M. OF E. P. **Ambient Air Quality Standard: GB 3095-2012 Chinese National Ambient Air Quality Standards (CNAAQS)**. 2012.

PAREEK, V. K. *et al.* Computational fluid dynamic (CFD) simulation of a pilot-scale annular bubble column photocatalytic reactor. **Chemical Engineering Science**, v. 58, p. 859–865, 2003.

PASSALÍA, C. *et al.* Modeling and Experimental Verification of a Corrugated Plate Photocatalytic Reactor Using Computational Fluid Dynamics. **Industrial & Engineering Chemistry Research**, v. 50, p. 9077–9086, 2011.

PAZ, Y. Application of TiO2 photocatalysis for air treatment: Patents' overview. **Applied Catalysis B: Environmental**, v. 99, p. 448–460, 2010.

PENCE, M. **Handbook of Air Pollution Control Systems and Devices**. 1. ed. Darya Ganj, Delhi: University Publications, 2012.

PÉREZ-NICOLÁS, M. *et al.* Atmospheric NOx removal: Study of cement mortars with iron- and vanadium-doped TiO2 as visible light–sensitive photocatalysts. **Construction and Building Materials**, v. 149, p. 257–271, 2017.

RAI, P. K. Particulate Matter and Its Size Fractionation. In: **Biomagnetic**

Monitoring of Particulate Matter. Aizawl, India: Elsevier Science, 2016. p. 216.

ROCHETTO, U. **Destruição de Compostos Orgânicos Voláteis em Fase Gasosa por Fotocatálise Heterogênea**. 2012. 132 f. Dissertação (Mestrado em Engenharia Química). Universidade Estadual de Campinas, 2012.

RODRIGUEZ-NARVAEZ, O. M. *et al.* Treatment technologies for emerging contaminants in water : A review. **Chemical Engineering Journal**, v. 323, p. 361–380, 2017.

ROEGIERS, J.; VAN WALSEM, J.; DENYS, S. CFD- and radiation field modeling of a gas phase photocatalytic multi-tube reactor. **Chemical Engineering Journal**, v. 338, p. 287–299, 2018.

ROY, S.; MADRAS, G. Photocatalytic NOx Abatement: A Short Review. **Current Organic Chemistry**, v. 19, p. 2122–2131, 2015.

SALVADÓ-ESTIVILL, I.; BRUCATO, A.; LI PUMA, G. Two-dimensional modeling of a flat-plate photocatalytic reactor for oxidation of indoor air pollutants. **Industrial and Engineering Chemistry Research**, v. 46, n. 23, p. 7489–7496, 2007.

SALVADÓ-ESTIVILL, I.; HARGREAVES, D. M.; LI PUMA, G. Evaluation of the intrinsic photocatalytic oxidation kinetics of indoor air pollutants. **Environmental Science and Technology**, v. 41, p. 2028–2035, 2007.

SEGUNDO, I. G. DA R. *et al.* Photocatalytic asphalt pavement: the physicochemical and rheological impact of TiO2 nano/microparticles and ZnO microparticles onto the bitumen. **Road Materials and Pavement Design**, p. 1–16, 2018.

SEO, D.; YUN, T. S. NOx removal rate of photocatalytic cementitious materials with TiO2 in wet condition. **Building and Environment**, v. 112, p. 233–240, 2017.

SHAYEGAN, Z.; LEE, C. S.; HAGHIGHAT, F. TiO2 photocatalyst for removal of volatile organic compounds in gas phase – A review. **Chemical Engineering Journal**, v. 334, p. 2408–2439, 2018.

SIKKEMA, J. K.; ONG, S. K.; ALLEMAN, J. E. Photocatalytic concrete pavements: Laboratory investigation of NO oxidation rate under varied environmental conditions. **Construction and Building Materials**, v. 100, p.

305–314, 2015.

SINGH, M.; SALVADÓ-ESTIVILL, I.; LI PUMA, G. Radiation Field Optimization in Photocatalytic Monolith Reactors for Air Treatment. **AIChE Journal**, v. 53, n. 3, p. 678–686, 2007.

TAGHIPOUR, F.; MOHSENI, M. CFD simulation of UV photocatalytic reactors for air treatment. **AIChE Journal**, v. 51, n. 11, p. 3039–3047, 2005.

TOKODE, O. *et al.* A photocatalytic impeller reactor for gas phase heterogeneous photocatalysis. **Journal of Environmental Chemical Engineering**, v. 5, n. 4, p. 3942–3948, 2017.

TOMASIC, V.; JOVIC, F.; GOMZI, Z. Photocatalytic oxidation of toluene in the gas phase : Modelling an annular photocatalytic reactor. **Catalysis Today**, v. 137, p. 350–356, 2008.

TRICHÊS, G. *et al.* **Peças Pré-Moldades de Concreto Fotocatalíticas para Pavimentação e Degradação de óxido de Nitrogênio (NOx) presentes na atmosfera.** In: 40a RAPv - Reunião Anual de Pavimentação, 2010, Rio de Janeiro. Anais da 40a RAPv - Reunião Anual de Pavimentação. Rio de Janeiro.

TSANG, C. H. A. *et al.* Titanium oxide based photocatalytic materials development and their role of in the air pollutants degradation : Overview and forecast. **Environment International**, v. 125, p. 200–228, 2019.

TSENG, Y.-H.; HUANG, B.-K. Photocatalytic Degradation of Using Ni-Containing TiO2. **International Journal of Photoenergy**, p. 1–7, 2012.

UNITED STATES ENVIRONMENT PROTECT AGENCY, E. **National Ambient Air Quality Standards (NAAQS)**. Available at: <https://www.epa.gov/criteria-air-pollutants/naaqs-table>. Accessed on: 09 jan. 2019.

VAN WALSEM, J. *et al.* CFD investigation of a multi-tube photocatalytic reactor in non-steady-state conditions. **Chemical Engineering Journal**, v. 304, p. 808–816, 2016.

VERBRUGGEN, S. W. TiO2 photocatalysis for the degradation of pollutants in gas phase: From morphological design to plasmonic enhancement. **Journal of Photochemistry and Photobiology C: Photochemistry Reviews**, v. 24, p. 64–82, 2015.

VERBRUGGEN, S. W. *et al.* CFD modeling of transient adsorption/desorption behavior in a gas phase photocatalytic fiber reactor. **Chemical Engineering Journal**, v. 292, p. 42–50, 2016.

VERBRUGGEN, S. W.; LENAERTS, S.; DENYS, S. Analytic versus CFD approach for kinetic modeling of gas phase photocatalysis. **Chemical Engineering Journal**, v. 262, p. 1–8, 2015.

WANG, H. *et al.* Photocatalytic oxidation of nitrogen oxides using TiO2 loading on woven glass fabric. **Chemosphere**, v. 66, n. 1, p. 185–190, 2007.

WANG, L. K.; PEREIRA, N. C.; HUNG, Y.-T. **Air Pollution Control Engineering**. 1. ed. New Jersey: Human Press, 2004.

WANG, T. *et al.* Photocatalytic degradation properties of V-doped TiO2 to automobile exhaust. **Science of the Total Environment**, v. 586, p. 347–354, 2017.

WANG, X.; TAN, X.; YU, T. Modeling of formaldehyde photocatalytic degradation in a honeycomb monolith reactor using computational fluid dynamics. **Industrial and Engineering Chemistry Research**, v. 53, n. 48, p. 18402–18410, 2014a.

WANG, X.; TAN, X.; YU, T. Kinetic Study of Ozone Photocatalytic Decomposition Using a Thin Film of TiO2 Coated on a Glass Plate and the CFD Modeling Approach. **Industrial & Engineering Chemistry Research**, v. 53, n. 19, p. 7902–7909, 2014b.

WANG, Z. *et al.* CFD modeling of a UV-LED photocatalytic odor abatement process in a continuous reactor. **Journal of Hazardous Materials**, v. 215–216, p. 25–31, 2012.

WELTY, J. R.; WICKS, C. E.; WILSON, R. E.; RORRER, G. L. Fundaments of Momentum, Heat, and Mass Transfer. 5. ed. John Wiley & Sons, Inc, 2008.

WORLD HEALTH ORGANIZATION. **WHO guidelines for indoor air quality: selected pollutantsThird Sector**. Copenhagen, Denmark, 2010.

WORLD HEALTH ORGANIZATION. **Ambient air pollution: A global assessment of exposure and burden of disease**. Genebra, Switzerland, 2016.

WORLD HEALTH ORGANIZATION. **Burning opportunity: clean household energy for health, sustainable development, and wellbeing of**

women and children. Genebra, Switzerland, 2016.

YANG, C.; SIMON, T.; CUI, T. Numerical simulation and analysis of hybrid physical-chemical vapor deposition to grow uniform perovskite MAPbI 3. **Journal of Applied Physics**, v. 121, p. 144903, 2017.

YU, Q. L.; BALLARI, M. M.; BROUWERS, H. J. H. Indoor air purification using heterogeneous photocatalytic oxidation. Part II: Kinetic study. **Applied Catalysis B: Environmental**, v. 99, n. 1–2, p. 58–65, 2010.

YU, Q. L.; BROUWERS, H. J. H. Indoor air purification using heterogeneous photocatalytic oxidation. Part I: Experimental study. **Applied Catalysis B: Environmental**, v. 92, p. 454–461, 2009.

ZHANG, Y. **Modeling and Design of Photocatalytic reactors for Air Purification**. 2013. 182 f. Thesis (Degree of Doctor of Philosophy) - University of South Florida, 2013.

ZHANG, Y.; STEFANAKOS, E. K.; GOSWAMI, D. Y. Effect of photocatalytic surface roughness on reactors effectiveness for indoor air cleaning. **Building and Environment**, v. 61, p. 188–196, 2013.

ZHONG, L.; HAGHIGHAT, F. Photocatalytic air cleaners and materials technologies - Abilities and limitations. **Building and Environment**, v. 91, p. 191–203, 2015.

APPENDIX A – Supplementary Material for Chapter 3

Table A.1 –Maximum allowed concentration of NO_2 at the atmosphere ($\mu g \cdot m^{-3}$) according to different regulations.

Sampling time interval	WHO*	US (EPA**)	EU (EEA***)	China (MEP****)	Brazil (CONAMA*****)
1 h	200	100	400	200	320
1 year	40	53	40	80	100

Source: adapted from CONAMA (1990); European Environment Agency (2018); P.R.C. Environment (2012); United States Environment Protect Agency (1998); World Health Organization (2010) .
*World Health Organization
**Environmental Protection Agency
***European Environmental Agency
****Ministry of Environmental Protection
*****National Council for the Environment

Figure A.1 – Deaths due to atmospheric pollution worldwide

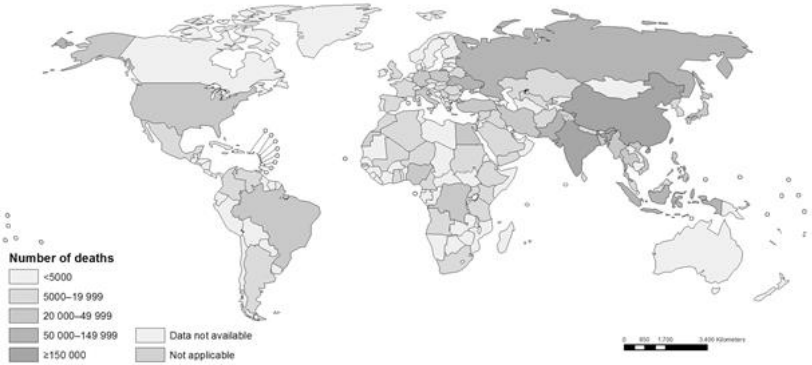

Source: adapted from World Health Organization (2016b).

A.1 Analyzing the rate law

According to Hunger, Hüsken and Brouwers (2010), the concentration of NO at the outlet of a parallel plate reactor can be related to the inlet concentration through the expression presented in Eq. A1, in case of mass transfer limiting step.

$$\frac{C_{NO}^{out}}{C_{NO}^{in}} = \frac{100 - X_{NO}^{MTL}}{100} = exp\left(-\frac{Sh \times D_{NO,air} \times L}{2 \times H^2 \times v}\right) \qquad \text{(A1)}$$

where C_{NO}^{in} and C_{NO}^{out} are the inlet and outlet concentration of NO, X_{NO}^{MTL} is the mass transfer-limited NO conversion, $D_{NO,air}$ is the molecular diffusivity of NO in air, L is the reactor length, H is the reactor height, v is the air velocity and Sh is the Sherwood dimensionless number, which can be calculated through Eq. A2 (HUNGER; HÜSKEN; BROUWERS, 2010).

$$Sh = \frac{k_c \times D_h}{D_{ij}} = 0.66 \times Re^{1/2} \times Sc^{1/3} \quad \text{(A2)}$$

Re and *Sc* represent, respectively, Reynolds and Schmidt dimensionless numbers.

Hunger, Hüsken and Brouwers (2010) have demonstrated that, for the reactor considered herein, X_{NO}^{MTL} should be equal to 99.3% regardless the inlet concentration of NO. According to Mills *et al.* (2016), mass transfer limitation can be neglected when $X_{NO} \ll X_{NO}^{MTL}$ and the authors suggest that $X_{NO} < 0.1 \times X_{NO}^{MTL}$ could be taken as a suitable criterion to consider $C_{NO,NO_2}^{g} \approx C_{NO,NO_2}^{s}$, *i.e.*, NO and NO_2 concentrations virtually equal at the surface of the catalyst material and at the bulk of the gas phase. Clearly, this is not the case when analyzing the kinetics taken from Ballari *et al.* (2010) and, thus, possible mass transfer limitations can be found in the kinetic parameters obtained by the authors. In CFD simulations of heterogeneous catalytic processes the reaction rate is imposed as a boundary condition at the catalytic surface and the intrinsic kinetic parameters are required. Therefore, the rate laws presented by Ballari *et al.* (2010) were analyzed to check if mass transfer limitations were considered in the kinetic parameters and corrections were then proposed to get the intrinsic parameters suitable for CFD modeling.

A 1D plug flow model considering mass transfer limitations in the gas phase can be derived according to Eq. A3.

$$v\frac{dC_{NO}^{g}}{dx} = -k_c a_v \left(C_{NO}^{g} - C_{NO}^{s}\right) \quad \text{(A3)}$$

where v is the air velocity, C_{NO}^{g} is the NO concentration at the bulk of the gas phase, x are Cartesian coordinates, k_c is the mass transfer coefficient, a_v is the surface/volume ratio and C_{NO}^{s} is the NO concentration at the surface of the catalytic material.

The flux of NO consumed at the catalytic surface can be described by Eq. A4, considering the kinetic parameters evaluated with bulk concentrations.

$$k_c\left(C_{NO}^g - C_{NO}^s\right) = \frac{k_{NO}'' C_{NO}^g}{1 + K_{NO}C_{NO}^g + K_{NO_2}C_{NO_2}^g + K_{H_2O}C_{H_2O}^g} \times \left(-1 + \sqrt{1 + \alpha E}\right) \quad \text{(A4)}$$

where k_{NO}'' and K_i ($i = NO, NO_2, H_2O$) represent kinetic and adsorption parameters, respectively, C_i^g is the species concentration at the bulk of the gas phase, α is a kinetic parameter related to the irradiance and E is the irradiance.

This flux reaching the catalyst must be equal to that obtained through the rate law evaluated with surface concentrations when corrected kinetic parameters are considered (Eq. A5).

$$k_c\left(C_{NO}^g - C_{NO}^s\right) = \frac{\tilde{k}_{NO}'' C_{NO}^s}{1 + \tilde{K}_{NO}C_{NO}^s + \tilde{K}_{NO_2}C_{NO_2}^s + K_{H_2O}C_{H_2O}^g} \times \left(-1 + \sqrt{1 + \alpha E}\right) \quad \text{(A5)}$$

where $\tilde{k}_{NO}''$ and $\tilde{K}_i$ (i = NO, NO_2 and H_2O) represent corrected kinetic and adsorption parameters, respectively.

It should be noted that $C_{H_2O}^g = C_{H_2O}^s$ since water is in great excess in the gaseous mixture. Therefore, the concentration of NO at the surface can be related to the concentration at the gas phase through the expression presented in Eq. A6.

$$C_{NO}^s = C_{NO}^g \times \left[1 - \frac{1}{k_c} \times \frac{k_{NO}''}{1 + K_{NO}C_{NO}^g + K_{NO_2}C_{NO_2}^g + K_{H_2O}C_{H_2O}^g} \times \left(-1 + \sqrt{1 + \alpha E}\right)\right] = C_{NO}^g \times f_{NO} \quad \text{(A6)}$$

where f_{NO} represents the correction factor for NO.

Similarly, the material balance for NO_2 can be described by a 1D plug flow model accounting for mass transport limitations according to Eq. A7.

$$v\frac{dC_{NO_2}^{g}}{dx} = k_c a_v\left(C_{NO_2}^{s} - C_{NO_2}^{g}\right) \tag{A7}$$

where v is the air velocity, $C_{NO_2}^{g}$ is the NO_2 concentration at the bulk of the gas phase, x are Cartesian coordinates, k_c is the mass transfer coefficient, a_v is the surface/volume ratio and $C_{NO_2}^{s}$ is the NO_2 concentration at the surface of the catalytic material.

Again, the flux of NO_2 production/consumption at the catalytic surface can be described by Eq. A8, considering the kinetic parameters evaluated with bulk concentrations.

$$\begin{aligned} & k_c\left(C_{NO_2}^{s} - C_{NO_2}^{g}\right) \\ & = \frac{k_{NO}'' C_{NO}^{g} - k_{NO_2}'' C_{NO_2}^{g}}{1 + K_{NO}C_{NO}^{g} + K_{NO_2}C_{NO_2}^{g} + K_{H_2O}C_{H_2O}^{g}} \\ & \times \left(-1 + \sqrt{1 + \alpha E}\right) \end{aligned} \tag{A8}$$

where k_i'' and K_i represent kinetic and adsorption parameters, respectively, C_i^g is the species concentration at the bulk of the gas phase, α is a kinetic parameter related to the irradiance and E is the irradiance.

This flux reaching the catalyst must be equal to that obtained through the rate law evaluated with surface concentrations when corrected kinetic parameters are considered (Eq. A9).

$$\begin{aligned} & k_c\left(C_{NO_2}^{s} - C_{NO_2}^{g}\right) \\ & = \frac{\tilde{k}_{NO}'' C_{NO}^{s} - \tilde{k}_{NO_2}'' C_{NO_2}^{s}}{1 + \widetilde{K}_{NO}C_{NO}^{s} + \widetilde{K}_{NO_2}C_{NO_2}^{s} + K_{H_2O}C_{H_2O}^{g}} \\ & \times \left(-1 + \sqrt{1 + \alpha E}\right) \end{aligned} \tag{A9}$$

where $\tilde{k}_i''$ and $\widetilde{K}_i$ represent corrected kinetic and adsorption parameters, respectively.

Therefore, the concentration of NO_2 at the surface can be related to the concentration at the gas phase through the expression presented in Eq. A10.

$$C_{NO_2}^s = C_{NO_2}^g \times \left[1 + \frac{1}{k_c} \times \frac{k''_{NO} \times \left(C_{NO}^g / C_{NO_2}^g\right)}{1 + K_{NO} C_{NO}^g + K_{NO_2} C_{NO_2}^g + K_{H_2O} C_{H_2O}^g} \times \left(-1 + \sqrt{1 + \alpha E}\right) - \frac{1}{k_c} \times \frac{k''_{NO_2}}{1 + K_{NO} C_{NO}^g + K_{NO_2} C_{NO_2}^g + K_{H_2O} C_{H_2O}^g} \times \left(-1 + \sqrt{1 + \alpha E}\right)\right] = C_{NO_2}^g \times f_{NO_2} \quad \text{(A10)}$$

where f_{NO_2} represents the correction factor for NO_2.

Thus, the rate laws with corrected kinetic parameters for evaluation with surface concentrations can be obtained and are expressed by Eqs. A11 and A12.

$$\begin{aligned} &(-r''_{NO})_s \\ &= \frac{(k''_{NO}/f_{NO}) \times C_{NO}^s}{1 + (K_{NO}/f_{NO}) \times C_{NO}^s + \left(K_{NO_2}/f_{NO_2}\right) \times C_{NO_2}^s + K_{H_2O} C_{H_2O}^g} \\ &\times \left(-1 + \sqrt{1 + \alpha E}\right) \\ &= \frac{\tilde{k}''_{NO} C_{NO}^s}{1 + \tilde{K}_{NO} C_{NO}^s + \tilde{K}_{NO_2} C_{NO_2}^s + K_{H_2O} C_{H_2O}^g} \times \left(-1 + \sqrt{1 + \alpha E}\right) \end{aligned} \quad \text{(A11)}$$

$$\begin{aligned} &\left(-r''_{NO_2}\right)_s \\ &= \frac{\left(k''_{NO_2}/f_{NO_2}\right) \times C_{NO_2}^s - (k''_{NO}/f_{NO}) \times C_{NO}^s}{1 + (K_{NO}/f_{NO}) \times C_{NO}^s + \left(K_{NO_2}/f_{NO_2}\right) \times C_{NO_2}^s + K_{H_2O} C_{H_2O}^g} \\ &\times \left(-1 + \sqrt{1 + \alpha E}\right) \\ &= \frac{\tilde{k}''_{NO_2} C_{NO_2}^s - \tilde{k}''_{NO} C_{NO}^s}{1 + \tilde{K}_{NO} C_{NO}^s + \tilde{K}_{NO_2} C_{NO_2}^s + K_{H_2O} C_{H_2O}^g} \times \left(-1 + \sqrt{1 + \alpha E}\right) \end{aligned} \quad \text{(A12)}$$

Therefore, the corrected parameters of the rate laws are expressed by Eqs. A13-A16 and the values obtained for different operational conditions are summarized in Table A.2.

$$\tilde{k}''_{NO} = (k''_{NO}/f_{NO}) \quad \text{(A13)}$$

$$\tilde{k}''_{NO_2} = \left(k''_{NO_2}/f_{NO_2}\right) \quad \text{(A14)}$$

$$\widetilde{K}_{NO} = \left(K_{NO}/f_{NO}\right) \quad \text{(A15)}$$

$$\widetilde{K}_{NO_2} = \left(K_{NO_2}/f_{NO_2}\right) \quad \text{(A16)}$$

Table A.2 – Correction factors (f_{NO} and f_{NO2}) as a function of the operational conditions.

E ($W \cdot m^{-2}$)	f_{NO}	f_{NO2}	*RH* (%)	f_{NO}	f_{NO2}	C_{NO}^{in} ($kmol \cdot m^{-3}$)	f_{NO}	f_{NO2}
0.3	0.999	1.162	10	0.885	0.878	4.50×10^{-9}	0.882	0.874
1	0.995	1.132	20	0.900	0.894	1.45×10^{-8}	0.901	0.894
2	0.989	1.095	30	0.922	0.919	2.25×10^{-8}	0.914	0.909
3	0.984	1.063	40	0.932	0.931	4.47×10^{-8}	0.939	0.941
4	0.978	1.035	50	0.939	0.941			
5	0.972	1.013	60	0.945	0.949			
6	0.966	0.993	70	0.950	0.957			
7	0.960	0.977	80	0.954	0.964			
8	0.953	0.964						
9	0.946	0.952						
10	0.939	0.941						
11	0.932	0.931						
13	0.916	0.912						

Source: Lira *et al.* (2018)

Higher deviations were observed at higher values of irradiance as well as lower values of relative humidity and feed concentration of NO, corresponding to regions of higher reaction rates at the surface. However, Hunger, Hüsken and Brouwers (2010) have already demonstrated that, for the reactor and operational conditions considered herein, the resistance due to the chemical reaction at the catalytic surface is much higher than that due to the mass transfer limitations at the gas phase.

Figure A.2 – In-house built code (UDF) for the calculation of $-r''_{NO}$ and $-r''_{NO2}$ at the active photocatalytic surface.

```
DEFINE_SR_RATE(my_rate, f, t, r, mw, yi, rr)
{

    Thread *t0 = t->t0;
    cell_t c0  = F_C0(f,t);

    double w_no  = yi[0];
    double w_h2o = yi[1];
    double w_no2 = yi[2];
    double w_air = yi[3];

    double Nsum = w_no/mw_no + w_h2o/mw_h2o + w_no2/mw_no2 + w_air/mw_air;

    double y_no  = (w_no/mw_no)/Nsum;
    double y_h2o = (w_h2o/mw_h2o)/Nsum;
    double y_no2 = (w_no2/mw_no2)/Nsum;
    double y_air = (w_air/mw_air)/Nsum;

    double T_w = F_T(f,t);           //K
    double P_w = F_P(f,t) + 101325;  //Pa

    double p_no  = P_w*y_no;   //Pa
    double p_h2o = P_w*y_h2o;  //Pa
    double p_no2 = P_w*y_no2;  //Pa
    double p_air = P_w*y_air;  //Pa
```

```
#include "udf.h"

#define mw_no     30.0061   //kg/kmol
#define mw_h2o    18.01534  //kg/kmol
#define mw_no2    46.00550  //kg/kmol
#define mw_air    28.9644   //kg/kmol
#define H         0.003     //m
#define Rg        8314.462  //Pa*m³/K/kmol
#define E         10        //W/m²
```

```
    double C_no  = p_no/(Rg*T_w);  //kmol/m³
    double C_h2o = p_h2o/(Rg*T_w); //kmol/m³
    double C_no2 = p_no2/(Rg*T_w); //kmol/m³
    double C_air = p_air/(Rg*T_w); //kmol/m³

    double k_no  = 4.18;           //m/s
    double k_no2 = 6.73e1;         //m/s

    double K_no  = 8.48e8;         //m³/kmol
    double K_no2 = 3.02e8;         //m³/kmol
    double K_h2o = 5.07e4;         //m³/kmol

    double alfa = 2.37e-3;         //m²/W

    double DEN = 1 + (K_no*C_no) + (K_no2*C_no2) + (K_h2o*C_h2o);

    if (STREQ(r->name, "reaction-1"))
        *rr = ((k_no*C_no)*(-1+sqrt(1+(alfa*E)))/DEN);                  //kmol/m²/s
    else if (STREQ(r->name, "reaction-2"))
        *rr = (((k_no2*C_no2)-(k_no*C_no))*(-1+sqrt(1+(alfa*E)))/DEN); //kmol/m²/s
}
```

Source: Lira *et al.* (2018)

Figure A.3 – Molar ratio of NOx and H_2O at the reactor's inlet and outlet as a function of the relative humidity.

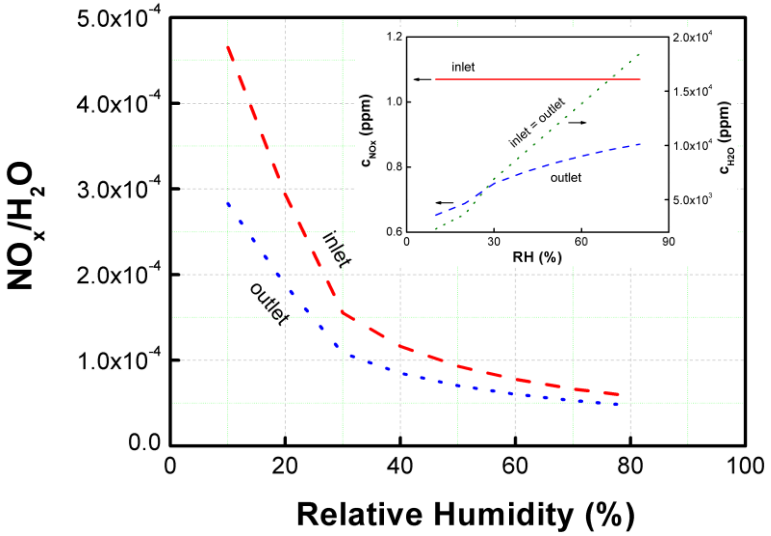

Source: Lira *et al.* (2018)

A.2 Commentary about the effect of light intensity (E) on the reactor performance

Figure A.4 presents the profiles of X_{NO} (%) and S (%) when the kinetic parameter α is multiplied by a factor of 10^3, with the corresponding correction of the kinetic parameters k''_{NO} and k''_{NO_2} by a factor of 2.25×10^{-3}. In this scenario, the nonlinearity of $X = X(E)$ for the higher values of E was properly captured.

Figure A.4 – NO conversion (X_{NO}) and selectivity (S) as a function of the irradiation intensity ($v_{x,in}$ = 0.1667 m·s^{-1}; RH=50%), considering the kinetic parameter α multiplied by a factor of 10^3 and the corresponding correction of the kinetic parameters k''_{NO} and k''_{NO2} by a factor of 2.25×10^{-3}.

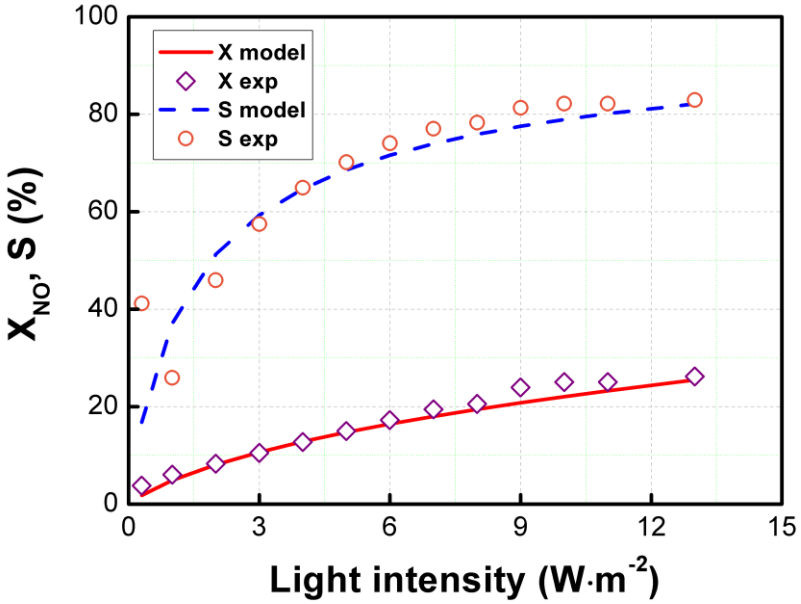

Source: Lira *et al.* (2018)

Figure A.5 – (a) X_{NO} (%) and (b) S (%) as a function of $C^{in}_{NO}/C^{in,max}_{NO}$ obtained with the CFD and 1D plug flow models.

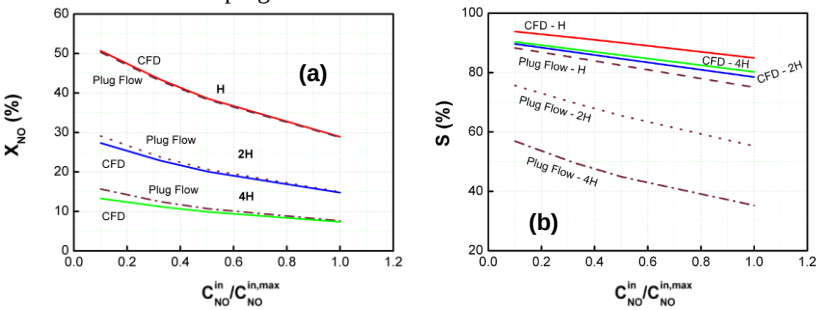

Source: Lira *et al.* (2018)

A.3 Fourth-order explicit Runge-Kutta method (RK4) for the 1D plug flow model (implemented in MATLAB®, version R2010b)

```
clear all;
clc;
close all;

%% Model parameters
global H av v cNOin cWin kNO KNO kNO2 KNO2 Kw
alpha E

kNO   = 4.18;
KNO   = 8.48e8;
kNO2  = 6.73e1;
KNO2  = 3.02e8;
Kw    = 5.07e4;
alpha = 2.37e-3;

H     = 3e-3;
av    = 1/H;
v     = 0.1667;
cNOin = 4.47e-8;
cWin  = 4.803324e-04;
E     = 10;

%% Handles

f1 = @(x,cno,cno2) av*(-kNO*cno*...
```

```
    (-1+sqrt(1+alpha*E))...
    /(1+KNO*cno+KNO2*cno2+Kw*cWin))/v;
f2 = @(x,cno,cno2) av*(-(kNO2*cno2-kNO*cno)...
    *(-1+sqrt(1+alpha*E))...
    /(1+KNO*cno+KNO2*cno2+Kw*cWin))/v;

%% Numerical parameters

dx = 1e-5;
xf = 0.2;
N  = ceil(xf/dx);

%% Initialization

cno(1)  = cNOin;
cno2(1) = 0;
x(1)    = 0;
rNO(1)  = 0;
rNO2(1) = 0;

%% RK4 method

for n = 1:N

    x(n+1) = x(n)+dx;

    k1no  = f1(x(n),cno(n),cno2(n));
    k1no2 = f2(x(n),cno(n),cno2(n));

    k2no= f1(x(n)+dx/2,cno(n)+dx/...
        2*k1no,cno2(n)+dx/2*k1no2);
    k2no2= f2(x(n)+dx/2,cno(n)+dx/...
        2*k1no,cno2(n)+dx/2*k1no2);

    k3no= f1(x(n)+dx/2,cno(n)+dx/...
        2*k2no,cno2(n)+dx/2*k2no2);
    k3no2= f2(x(n)+dx/2,cno(n)+dx/...
        2*k2no,cno2(n)+dx/2*k2no2);

    k4no= f1(x(n)+dx,cno(n)+dx*...
        k3no,cno2(n)+dx*k3no2);
```

```
    k4no2= f2(x(n)+dx,cno(n)+dx*...
        k3no,cno2(n)+dx*k3no2);

    cno(n+1)= cno(n)+dx/6*(k1no+2*...
        k2no+2*k3no+k4no);
    cno2(n+1)= cno2(n)+dx/6*(k1no2+...
        2*k2no2+2*k3no2+k4no2);

   rNO(n+1)=av*(kNO*cno(n)*(-1+...
        sqrt(1+alpha*E))...
        /(1+KNO*cno(n)+KNO2*cno2(n)+Kw*cWin))/v;

    rNO2(n+1) = av*((kNO2*cno2(n)-kNO*cno(n))...
                *(-1+sqrt(1+alpha*E))...
                /(1+KNO*cno(n)+KNO2*...
                cno2(n)+Kw*cWin))/v;
end

X = ((cNOin-cno(end))/cNOin)*100
S = (1-cno2/(cNOin-cno))*100
int_no = trapz(x,rNO)
```

A.4 Effect of inlet NO concentration (C_{NO}^{in}) and light intensity (E) on the reaction rate

As higher the inlet NO concentration, more significant is the effect of the irradiance on the reaction rate (see Figure A.6). Nevertheless, higher relative impact is noticed as lower the irradiance. Also, it is interesting to notice that independently of the irradiance considered, a saturation for the reaction rate is observed when the NO concentration at the reactor inlet is increased.

As the irradiance is increased, higher is the number of electron-hole pairs and thus radicals formed. Therefore, higher conversion is expected as E increases. However, for low pollutant concentrations there is an excess of radicals formed, resulting in effective conversion for a significant range of light intensities values. As the pollutant concentration is increased, though, a higher gradient between the bulk and the catalyst's surface is reached, resulting in more molecules adsorbed. This condition indicates that the rate of radical generation is the limiting step. Interestingly, for a given irradiance, the rate of NO consumption increases, but tends to reach a plateau, as the pollutant concentration is

increased at the reactor inlet (Figure A.6). This trend is in accordance with the results obtained experimentally by Yu and Brouwers (2009) when working under similar conditions.

Figure A.6 – Integral rate of NO consumption ($-r''_{NO}$ integrated at the photocatalytic surface considering unitary depth) as a function of the concentration at the inlet and irradiance.

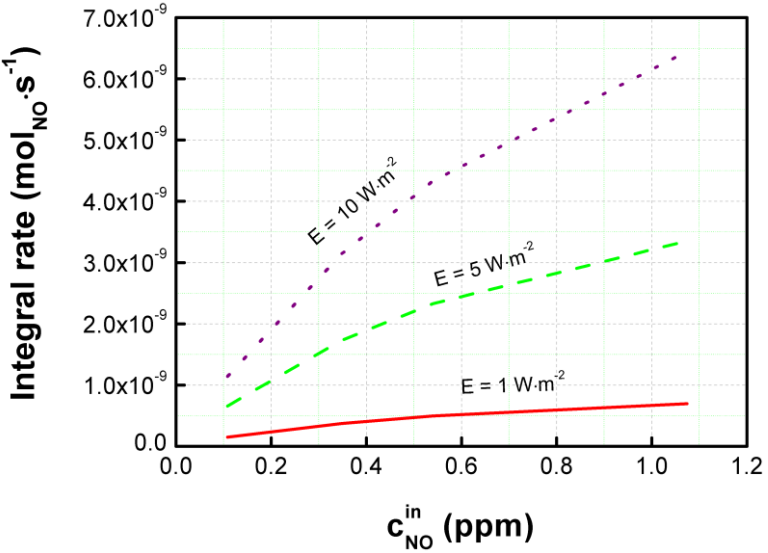

Source: Lira *et al.* (2018)

A.5 Details about the mesh independence study

Although the average NO concentration at the reactor outlet essentially did not change when the mesh refinement level is significantly varied, an analysis of species molar fraction profiles at the reactor inlet shows that significant numerical diffusion may be encountered when a coarser mesh is considered (see Figure A.7(a,b)). This behavior is particularly evident when comparing NO and NO_2 molar fraction profiles obtained with a mesh consisting in ~8.0×10^3 elements (mesh A) and those taken with meshes consisting in ~3.2×10^4 and ~1.2×10^5 elements (meshes B and C, respectively). Since the profiles obtained with mesh B did not differ significantly from that for mesh C, despite ~275% of refinement, and considering that the average concentration values taken at the reactor outlet were essentially the same, mesh B was used in this study.

It is also worth to notice that the NO_2 molar fraction does not departure from zero, at x = 0.00, when evaluated at y = 0.00 in Figure 7(b). It can be explained using Figure A.7(c,d). Clearly, the NO and NO_2 molar fraction profiles entered the reactor (*i.e.*, at x = 0) with the same value imposed according to the boundary conditions expressed by Eq. 4.30 for y = 0.0015 and 0.003. At these positions, the species are only transported (by advection + diffusion) through the reactor (*i.e.*, there is absence of any source/sink term). However, at y = 0.00 m the boundary condition expressed by Eq. 3.34 (*i.e.*, the reaction rate calculated through the UDF) is valid for $0 < x < L$. Thus, at (0.0) the species balance must be satisfied considering the composition imposed at the inlet and the flux specified at the catalytic surface. Therefore, at this point the NO concentration is slight lower than that imposed as inlet boundary condition (due to the consumption calculated by Eq. 4.35), while the NO_2 concentration is finite (due to the production expressed by Eq. 4.36).

Figure A.7 – (a) NO and (b) NO_2 composition profiles taken at the entrance of the reactor considering different mesh refinements (~8.0×10^3, ~3.2×10^4 and ~1.2×10^5 elements for meshes A, B and C, respectively); (c) NO and (d) NO_2 composition profiles taken at the reactor inlet at y = 0.00, 0.0015 and 0.003 m (considering mesh B in all cases).

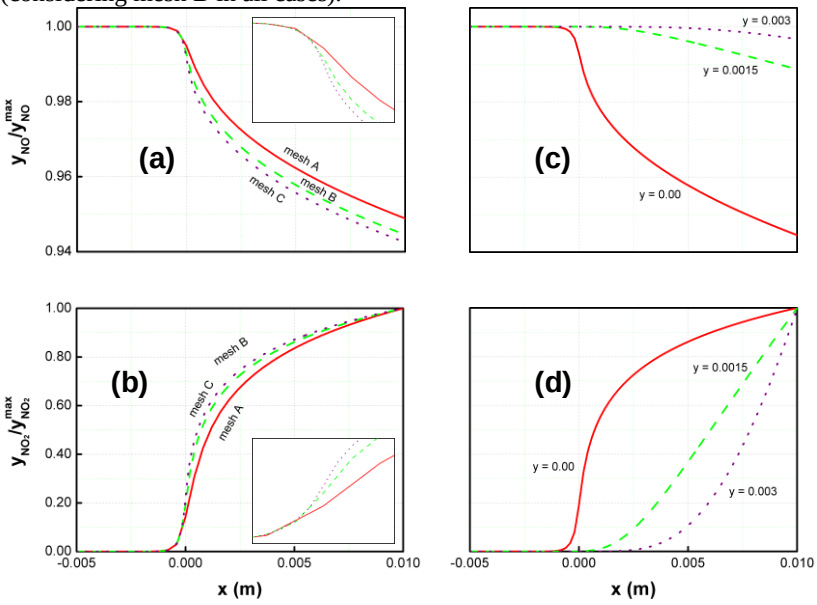

Source: Lira *et al.* (2018)

APPENDIX B – Supplementary Material for Chapter 4

Table B.1 – 2D and 3D models equations: system of nonlinear partial differential equations.

	2D	3D
Equation of continuity	$\frac{\partial}{\partial x}(\rho v_x)+\frac{\partial}{\partial y}(\rho v_y)=0$	$\frac{\partial}{\partial x}(\rho v_x)+\frac{\partial}{\partial y}(\rho v_y)+\frac{\partial}{\partial z}(\rho v_z)=0$
Navier-Stokes equations	$\frac{\partial}{\partial x}(\rho v_x v_x)+\frac{\partial}{\partial y}(\rho v_y v_x) = -\frac{\partial P}{\partial x}-\left(\frac{\partial}{\partial x}\tau_{xx}+\frac{\partial}{\partial y}\tau_{yx}\right)$ $\frac{\partial}{\partial x}(\rho v_x v_y)+\frac{\partial}{\partial y}(\rho v_y v_y)=-\frac{\partial P}{\partial y}-\left(\frac{\partial}{\partial x}\tau_{xy}+\frac{\partial}{\partial y}\tau_{yy}\right)$	$\frac{\partial}{\partial x}(\rho v_x v_x)+\frac{\partial}{\partial y}(\rho v_y v_x)+\frac{\partial}{\partial y}(\rho v_z v_x)=-\frac{\partial P}{\partial x}-\left(\frac{\partial}{\partial x}\tau_{xx}+\frac{\partial}{\partial y}\tau_{yx}+\frac{\partial}{\partial z}\tau_{zx}\right)$ $\frac{\partial}{\partial x}(\rho v_x v_y)+\frac{\partial}{\partial y}(\rho v_y v_y)+\frac{\partial}{\partial y}(\rho v_z v_y)=-\frac{\partial P}{\partial y}-\left(\frac{\partial}{\partial x}\tau_{xy}+\frac{\partial}{\partial y}\tau_{yy}+\frac{\partial}{\partial z}\tau_{zy}\right)$ $\frac{\partial}{\partial x}(\rho v_x v_z)+\frac{\partial}{\partial y}(\rho v_y v_z)+\frac{\partial}{\partial y}(\rho v_z v_z)=-\frac{\partial P}{\partial z}-\left(\frac{\partial}{\partial x}\tau_{xz}+\frac{\partial}{\partial y}\tau_{yz}+\frac{\partial}{\partial z}\tau_{zz}\right)$
Newton's Law of viscosity	$\tau_{xx}=-\mu\left(2\frac{\partial v_x}{\partial x}\right)+\frac{2}{3}\mu\left(\frac{\partial v_x}{\partial x}+\frac{\partial v_y}{\partial y}\right)$ $\tau_{yy}=-\mu\left(2\frac{\partial v_y}{\partial y}\right)+\frac{2}{3}\mu\left(\frac{\partial v_x}{\partial x}+\frac{\partial v_y}{\partial y}\right)$ $\tau_{xy}=\tau_{yx}=-\mu\left(\frac{\partial v_y}{\partial x}+\frac{\partial v_x}{\partial y}\right)$	$\tau_{xx}=-\mu\left(2\frac{\partial v_x}{\partial x}\right)+\frac{2}{3}\mu\left(\frac{\partial v_x}{\partial x}+\frac{\partial v_y}{\partial y}+\frac{\partial v_z}{\partial z}\right)$ $\tau_{yy}=-\mu\left(2\frac{\partial v_y}{\partial y}\right)+\frac{2}{3}\mu\left(\frac{\partial v_x}{\partial x}+\frac{\partial v_y}{\partial y}+\frac{\partial v_z}{\partial z}\right)$ $\tau_{yy}=-\mu\left(2\frac{\partial v_z}{\partial z}\right)+\frac{2}{3}\mu\left(\frac{\partial v_x}{\partial x}+\frac{\partial v_y}{\partial y}+\frac{\partial v_z}{\partial z}\right)$ $\tau_{xy}=\tau_{yx}=-\mu\left(\frac{\partial v_y}{\partial x}+\frac{\partial v_x}{\partial y}\right)$ $\tau_{yz}=\tau_{zy}=-\mu\left(\frac{\partial v_z}{\partial y}+\frac{\partial v_y}{\partial z}\right)$ $\tau_{zx}=\tau_{xz}=-\mu\left(\frac{\partial v_x}{\partial z}+\frac{\partial v_z}{\partial x}\right)$
Equation of continuity for specie i in terms of J_i	$\frac{\partial}{\partial x}(\rho v_x \omega_i)+\frac{\partial}{\partial y}(\rho v_y \omega_i)+\frac{\partial}{\partial x}(J_{i,x})+\frac{\partial}{\partial y}(J_{i,y})=0$	$\frac{\partial}{\partial x}(\rho v_x \omega_i)+\frac{\partial}{\partial y}(\rho v_y \omega_i)+\frac{\partial}{\partial z}(\rho v_z \omega_i)+\frac{\partial}{\partial x}(J_{i,x})+\frac{\partial}{\partial y}(J_{i,y})+\frac{\partial}{\partial z}(J_{i,z})=0$
Fick's Law	$J_{i,x}=-\rho D_{i,m}\frac{\partial \omega_i}{\partial x}$ $J_{i,y}=-\rho D_{i,m}\frac{\partial \omega_i}{\partial y}$	$J_{i,x}=-\rho D_{i,m}\frac{\partial \omega_i}{\partial x}$ $J_{i,y}=-\rho D_{i,m}\frac{\partial \omega_i}{\partial y}$ $J_{i,z}=-\rho D_{i,m}\frac{\partial \omega_i}{\partial z}$

Source: Bird, Stewart and Lightfoot (2002).

Table B.2 – Comparison of NO conversion from 2D and 3D models.

Variable		2D model results		3D model results		Deviation NO (%)	Deviation NO_2 (%)
		$C_{NO,out}$ (kmol·m^{-3})	$C_{NO2,out}$ (kmol·m^{-3})	$C_{NO,out}$ (kmol·m^{-3})	$C_{NO2,out}$ (kmol·m^{-3})		
RH^{*} (%)	10	2.55×10^{-8}	1.66×10^{-9}	2.56×10^{-8}	1.61×10^{-9}	0.400	3.249
	30	2.94×10^{-8}	1.83×10^{-9}	2.94×10^{-8}	1.83×10^{-9}	0.013	0.094
	60	3.27×10^{-8}	1.99×10^{-9}	3.27×10^{-8}	1.99×10^{-9}	0.008	0.099
E^{**} (W·m^{-2})	1	4.33×10^{-8}	1.05×10^{-9}	4.33×10^{-8}	1.05×10^{-9}	0.000	0.047
	6	3.67×10^{-8}	2.12×10^{-9}	3.67×10^{-8}	2.11×10^{-9}	0.003	0.107
	13	2.83×10^{-8}	1.77×10^{-9}	2.83×10^{-8}	1.77×10^{-9}	0.019	0.085
$C_{NO,in}^{***}$ (kmol·m^{-3})	4.50×10^{-9}	2.22×10^{-9}	1.41×10^{-10}	2.22×10^{-9}	1.41×10^{-10}	0.065	0.035
	1.45×10^{-8}	8.20×10^{-9}	5.18×10^{-10}	8.21×10^{-9}	5.18×10^{-10}	0.013	0.087
	2.25×10^{-8}	1.38×10^{-8}	8.67×10^{-10}	1.38×10^{-8}	8.66×10^{-10}	0.026	0.076

$^{*}E$ = 10 W·m^{-2} and $C_{NO,in}$ = 4.47×10^{-8} kmol·m^{-3}

$^{**}C_{NO,in}$ = 4.47×10^{-8} kmol·m^{-3} and RH = 50%

$^{***}E$ = 10 W·m^{-2} and RH = 50%

APPENDIX C – Contributions from members of the examination board

This chapter was developed to emphasize the contributions made by members of the examination board: Prof. Dr. João Lameu da Silva Jr. and Prof. Dr. Alexandre Kupka da Silva. It should be noted that the contributions made particularly in chapter 3 could not be changed in the document because this chapter is based on the article entitled "Photocatalytic NOx abatement: Mathematical modeling, CFD validation and reactor analysis" (https://doi.org/10.1016/j.jhazmat.2018.07.009) which has already been published, and the Journal of Hazardous Materials has the copyright of the same. So, some contributions made by members of the examination board were highlighted below.

1. Coordinate system in Figure 3.1

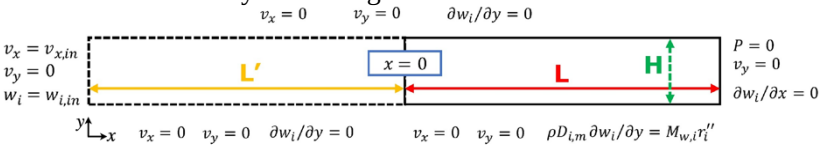

Source: adapted from Lira *et al.* (2018).

2. Why was the luminous intensity set equal to E = 10 W·m^{-2} used as the standard condition?

The ISO 22197-1:2007 method (Fine ceramics (advanced ceramics, advanced technical ceramics) — Test method for air-purification performance of semiconducting photocatalytic materials — Part 1: Removal of nitric oxide) was established to provide a standard test to determine the NO and NO_2 removal activities. This standard uses a flat plate photoreactor with the catalyst being immobilized on a flat surface. According to the ISO 22197-1 specification, the reactor must be irradiated with a UV lamp (E = 10 W·m^{-2} $\pm$ 0.5 W·m^{-2}).

3. What is the relationship between the variation of the height of the reactor and the pressure drop?

Different geometric configurations, varying the height (*H*, 2*H* and 4*H*), were performed throughout the dissertation. It should be noted that the effect of height variation on pressure drop was not recorded.

Figure 3.9 showed that the reactor with the *H* dimension had a higher NO conversion, but it is expected that, as the reactor height

decreases, the pressure drop will increase compared to the other geometries. Then a question remains, is it worth to use the reactor with height *H* even with an associated pressure drop? In order to answer this question, it is evident that it is necessary to optimize the process to find an optimal point between the NO degradation rate and the pressure drop for the flat plate photocatalytic reactor.

4. Instead using velocity, it is better work with Reynolds number.

The Reynolds number is defined as a ratio between the inertial forces ($v\rho$) and the viscous forces (μ/H), which can be expressed by Eq. C1.

$$Re = \frac{\rho v H}{\mu} \tag{C1}$$

where, ρ is the density of the mixture, v is the velocity of the mixture, H is the height of the reactor and μ is the dynamic viscosity of the mixture. Thus, the Reynolds number for this study is equals to 128.18.

5. Diffusion coefficient for binary gas mixtures containing polar compounds.

The binary molecular diffusion coefficients D_{ij} were calculated through a modified Chapman-Enskog correlation given by Eq. 3.22 as reported in Chapter 3 (MCGEE, 1991).

$$D_{ij} = 0.0018583 \times \frac{\left[T^3\left(\frac{1}{M_{w,i}} + \frac{1}{M_{w,j}}\right)\right]^{\frac{1}{2}}}{P_{abs}\sigma_{ij}^2\Omega_D} \tag{3.22}$$

This equation is used for the diffusion coefficient for non-polar gas pairs (WELTY et al., 2008). This relationship must be modified when there are polar molecules; the correlation proposed by Brokaw estimates the diffusion coefficient for binary gas mixtures containing polar compounds. The modified Chapman-Enskog is still used; however, the collision integral (Ω_D) is evaluated by Eqs. C2 – C4.

$$\Omega_D = \Omega_{D0} + \frac{0.196\delta_{ij}^2}{T^*} \tag{C2}$$

$$\delta_{ij} = \left(\delta_i \delta_j\right)^{1/2} \tag{C3}$$

$$\delta_i = \frac{1.94 \times 10^3 \mu_p^2}{V_b T_b} \tag{C4}$$

where, μ_p is the dipole moment (Debye), V_b is the liquid molar volume of the specific compound at its boiling point and T_b is the normal boiling point.

The collision integral (Ω_{D0}) is a function of the dimensionless temperature by Eqs. C5 – C8 (WELTY *et al.*, 2008).

$$T^* = \frac{T}{\varepsilon_{ij}/\kappa} \tag{C5}$$

$$\frac{\varepsilon_{ij}}{\kappa} = \left(\frac{\varepsilon_i}{\kappa}\frac{\varepsilon_j}{\kappa}\right)^{\frac{1}{2}} \tag{C6}$$

$$\frac{\varepsilon_i}{\kappa} = 1.18(1 + 1.3\delta_i^2)T_b \tag{C7}$$

$$\Omega_{D0} = \frac{1.06036}{T^{*0.15610}} + \frac{0.19300}{\exp(0.47635 \times T^*)} + \frac{1.03587}{\exp(1.52996 \times T^*)} + \frac{1.76474}{\exp(3.89411 \times T^*)} \tag{C8}$$

The collision diameter, σ_{ij}, was calculated given in Eq. C9 and Eq. C10 (WELTY *et al.*, 2008).

$$\sigma_{ij} = \frac{\sigma_i + \sigma_j}{2} \tag{C9}$$

$$\sigma_i = \left(\frac{1.585 \times V_b}{1 + 1.3\delta_i^2}\right)^{\frac{1}{3}} \tag{C10}$$

Table C.1 illustrates the results of the diffusion coefficients for the binary mixtures using the Brokaw correlation and modified Chapman-Enskog correlation. It was observed that the diffusivity values presented a small difference between them, but this difference did not affect the NO

conversion and selectivity as shown in Table C.2, where the deviations were less than 1% in all cases.

Table C.1 – Diffusion coefficient for binary gas mixture.

Species	D_{ij} ($m^2 \cdot s^{-1}$) by Brokaw correlation*			D_{ij} ($m^2 \cdot s^{-1}$) by modified Chapman-Enskog correlation**		
	NO	NO_2	H_2O^{vap}	NO	NO_2	H_2O^{vap}
air	2.01×10^{-5}	1.42×10^{-5}	2.96×10^{-5}	1.76×10^{-5}	1.60×10^{-5}	2.25×10^{-5}
NO	-	1.39×10^{-5}	2.18×10^{-5}	-	1.42×10^{-5}	1.94×10^{-5}
NO_2	-	-	1.42×10^{-5}	-	-	1.81×10^{-5}
H_2O^{vap}	-	-	-	-	-	-

Source: *Welty *et al.* (2008); **Mcgee (1991).

Table C.2 – NO conversion (X_{NO}) and selectivity (S) using the Brokaw correlation and modified Chapman-Enskog correlation.

Variable		Brokaw correlation		Modified Chapman-Enskog correlation		Deviation X_{NO} (%)	Deviation S (%)
		X_{NO} (%)	S (%)	X_{NO} (%)	S (%)		
RH^* (%)	10	43.06	91.26	42.99	91.34	0.15	0.08
	30	34.39	88.10	34.31	88.09	0.22	0.02
	50	28.97	85.00	28.91	84.90	0.23	0.12
	70	25.12	82.09	25.07	81.92	0.22	0.21

*Case: $^*E$ = 10 $W \cdot m^{-2}$ and $C_{NO,in} = 4.47\times10^{-8}$ $kmol \cdot m^{-3}$

6. Grid independence check using GCI method.

The GCI method was developed to estimate the uncertainty related to spatial discretization by Celik *et al.* (2008). This method was used to corroborate the results of the mesh independence study performed in Appendix A.5.

The GCI study was developed using the NO and NO_2 concentration at the reactor outlet. Three sets of mesh with $\sim1.5\times10^5$, $\sim3.2\times10^4$ e $\sim8.0\times10^3$ elements were designed for the flat plate photocatalytic reactor. The finest mesh was named Mesh1, the middle mesh was named Mesh2 while the coarsest mesh was named as Mesh3. The three grids in this study were generated using refining greater than 1.3 (CELIK *et al.*, 2008).

To calculate the refinement errors an algorithm was developed in MATLAB®, version R2010b, software based on the routine of Celik *et al.* (2008). Table C.3 shows the estimates of the numerical uncertainty of the refined mesh (GCI21) and the intermediate mesh (GCI32), respectively, for the NO and NO_2 concentration at the outlet of the reactor. The results showed that the GCI values for NO and NO_2 were very close to zero, meaning that the values of the variables were statistically the same

and the meshes were very similar. Therefore, this result corroborates the choice of Mesh2 to be used in this study as also shown in Appendix A.5.

Table C.3 – GCI values.

	NO		NO_2	
	21	32	21	32
Grid convergence index (GCI)	0.0000156%	0.0001791%	0.0012780%	0.0037646%

Code for the GCI method (implemented in MATLAB®, version R2010b)

```
clear all; clc; close all;
%%GCI method
%%2D
%%MESH
%Elements number
N1=124062; %FineMesh
N2=32032;  %MiddleMesh
N3=8016;   %CoarseMesh

%%VARIABLE
VariableName='NO outlet concentration x10^8
(kmol/m^3)';
f1=3.177929;  %FineMeshNO
f2=3.177909;  %MiddleMeshNO
f3=3.176784;  %CoarseMeshNO

%VariableName='NO_{2} outlet concentration x10^9
(kmol/m^3)';
%f1=1.950791; %FineMeshNO2
%f2=1.950826;  %MiddleMeshNO2
%f3=1.950926; %CoarseMeshNO2

%%PARAMETERS - CELIK ROUTINE
h1=(1/N1)^(1/2);
h2=(1/N2)^(1/2);
h3=(1/N3)^(1/2);

r21=h2/h1;
r32=h3/h2;

e32=f3-f2;
e21=f2-f1;
```

```
p = fzero(@(x) funp(x,e32,e21,r32,r21), 15);

f_ex21=((r21^p)*f1-f2)/((r21^p)-1);
f_ex32=((r32^p)*f2-f3)/((r32^p)-1);

E_a21=abs((f1-f2)/f1)*100;
E_a32=abs((f2-f3)/f2)*100;

E_ex21=abs((f_ex21-f1)/f_ex21)*100;
E_ex32=abs((f_ex32-f2)/f_ex32)*100;

GCI21=(1.25*E_a21/((r21^p)-1));
GCI32=GCI21*r21*p;

%%RESULTS

fprintf('p = %4.2f \n', p)
fprintf('f_ex21 = %4.2f\n\n', f_ex21)
fprintf('E_a21 = %4.7f %%\n', E_a21)
fprintf('E_ex21 = %4.7f %%\n', E_ex21)
fprintf('GCI21 = %4.7f %%\n\n', GCI21)

fprintf('f_ex32 = %4.2f\n\n', f_ex32)
fprintf('E_a32 = %4.7f %%\n', E_a32)
fprintf('E_ex32 = %4.7f %%\n', E_ex32)
fprintf('GCI32 = %4.7f %%\n', GCI32)

%%GRAPHIC
xnumber=[0 1/N1 1/N2 1/N3];
ynumber=[f_ex21 f1 f2 f3];
splynumber = interp1
(xnumber,ynumber,[0:1/(50*N1):1/N3], 'PCHIP');
plot(xnumber,ynumber,'xb',
[0:1/(50*N1):1/N3],splynumber,'-r',
'MarkerSize',10)
xlabel('1/N');
A=(1/N3)+0.05*(1/N3);
xlim([-1e-10,A]);
ylabel(VariableName);

plottools('on')
set(gcf,'color',[1,1,1])
box on
```

```
set(gcf,'color','w');

%%FUNCTION
function y=funp(x,e32,e21,r32,r21)
       s=1*sign(e32/e21);
       q=log(((r21^x)-s)/((r32^x)-s));
       y=(abs(log(abs(e32/e21))+q)/(log(r21)))-x;
```